



HAL
open science

Nanostructured W-O thin films by reactive sputtering: application as gas sensors

Xiaolong Xu

► **To cite this version:**

Xiaolong Xu. Nanostructured W-O thin films by reactive sputtering: application as gas sensors. Micro and nanotechnologies/Microelectronics. Université Bourgogne Franche-Comté, 2018. English. NNT : 2018UBFCA003 . tel-01865498

HAL Id: tel-01865498

<https://theses.hal.science/tel-01865498>

Submitted on 31 Aug 2018

HAL is a multi-disciplinary open access archive for the deposit and dissemination of scientific research documents, whether they are published or not. The documents may come from teaching and research institutions in France or abroad, or from public or private research centers.

L'archive ouverte pluridisciplinaire **HAL**, est destinée au dépôt et à la diffusion de documents scientifiques de niveau recherche, publiés ou non, émanant des établissements d'enseignement et de recherche français ou étrangers, des laboratoires publics ou privés.

SPIM

Thèse de Doctorat



école doctorale sciences pour l'ingénieur et microtechniques

UNIVERSITÉ DE TECHNOLOGIE BELFORT-MONTBÉLIARD

Nanostructured W-O thin films by reactive sputtering: application as gas sensors

■ Xiaolong XU

Thesis

“Nanostructured W-O thin films by reactive sputtering: application as gas sensors”

By

XU Xiaolong

Université Bourgogne Franche-Comté

**Ecole Doctorale Sciences Pour l'Ingénieur et
Microtechniques - SPIM**

Defended on Tuesday, March 27, 2018

President

SANCHETTE Frédéric, Professor, Université de Technologie de Troyes, France

Reviewers

PALMERO Alberto, Professor, University of Sevilla, CSIC, Spain

VIRICELLE Jean-Paul, Directeur de Recherches, École Nationale Supérieure des Mines de Saint-Étienne, France

Members

ARAB POUR YAZDI Mohammad, Ingénieur de Recherche (Co-supervisor), Université de Technologie Belfort-Montbéliard, France

BILLARD Alain, Professor, (Co-supervisor), Université de Technologie Belfort-Montbéliard, France

MARTIN Nicolas, Professor, (Co-supervisor), Ecole Nationale Supérieure de Mécanique et des Microtechniques, France

TOMASELLA Eric, Professor, Université Clermont Auvergne, France

SANCHEZ Jean-Baptiste, Maître de Conférences, Université de Franche-Comté, France

Acknowledgements

This work of thesis was fulfilled in team of Micro NAno MAterials & Surfaces (MINAMAS), department of Micro Nano Sciences and Systems (MN2S), Institute of Franche-Comté Electronic Mechanic Thermic and Optic – Sciences and Technologies (FEMTO-ST), at Université Bourgogne Franche-Comté (UBFC).

I am thankful for my supervisor, Nicolas MARTIN, who guided me with deposition of thin films, testing electric and optical properties, and helped me a lot for living in France. Alain BILLARD, who directed the stage of work and gave me advices, also kindly let me use the device for X-ray diffraction and sensor test system. Mohammad ARAB POUR YAZDI, who is a kindly researcher, taught and worked with me for dodecane sensing performances.

I also need to thank the team members, Jean-Baptiste SANCHEZ and Franck BERGER, who worked with me about the sensing performances of ozone, and gave me the help for articles as experts in gas sensing mechanisms.

I need to express my acknowledgements to Jean-Yves RAUCH, Roland SALUT, Jean-Marc COTE and Valérie POTIN, who helped me with all characterization instruments, analysis and publications as co-authors.

This work was performed in cooperation with the LABEX ACTION program (contract ANR-11-LABX-01-01) and the RENATECH network. I got financial support from the China Scholarship Council (CSC China).

Last but not least, I have to say it's fortunately to meet you, Stefania Oliveri, Gautier Lecoutre, Raya El Beainou, Anurupa Shaw, Phong Trần, Etienne Coffy, Venan CV, Xavier Romain, Tatiana Kovalevich, Bicky Marquez, Tintu Kuriakose, Séverine Denis, Petra Villette. We really spent a lot of time in Besançon and left good memories.

List of symbols and abbreviations

sccm: standard cubic centimeter per minute

J_W : target current density ($A\ m^{-2}$)

P: period of rectangular signal (s)

T_{ON} : time of injection of the oxygen gas (s)

T_{OFF} : time without any oxygen injection (s)

dc : duty cycle T_{ON}/P

α : incident angle of substrate ($^\circ$)

α_W : angle between the W target normal and the substrate normal ($^\circ$)

α_{WO_3} : angle between the WO_3 target normal and the substrate normal ($^\circ$)

ϕ : computer-controlled rotating speed of the substrate holder ($rev\ h^{-1}$)

n : refractive index

π : porosity

ε : relative dielectric constant

p_{sp} : total sputtering pressure (mbar)

p_{Ar} : argon partial pressure (mbar)

q_{Ar} : argon mass flow rate (sccm)

p_{O_2} : oxygen partial pressure (mbar)

q_{O_2} : oxygen mass flow rate (sccm)

S: pumping speed ($L\ s^{-1}$)

I_W : W target current (mA)

U_W : W target DC potential (V)

U_{WO_3} : self-bias potential of the WO_3 target (V)

CONTENTS

1. GENERAL INTRODUCTION	1
2. CHAPTER 1: STATE-OF-THE-ART	7
2.1. <u>W-O COMPOUNDS AND THIN FILMS</u>	7
2.2. <u>METHODS FOR PRODUCING WO_x FILMS</u>	8
2.1.1 <i>Sol-gel method</i>	8
2.1.2 <i>Hydrothermal method</i>	9
2.1.3 <i>Electrospinning method</i>	9
2.1.4 <i>Physical vapor deposition method</i>	10
2.3. <u>WO_x FILMS BY RGPP</u>	11
2.4. <u>WO_x FILMS BY GLAD</u>	13
2.5. <u>WO_x FILMS AS AN ACTIVE LAYER FOR GAS SENSORS</u>	15
2.6. <u>CONCLUSION</u>	19
3. CHAPTER 2: MATERIALS AND METHODS	21
3.1. <u>DEPOSITION SETUP AND CONDITIONS</u>	21
3.2. <u>CHARACTERIZATION TECHNIQUES</u>	26
3.3. <u>SENSOR SETUPS AND CONDITIONS</u>	28
4. CHAPTER 3: WO_x FILMS WITH ONE W TARGET	33
4.1. <u>WO_x FILMS BY RGPP</u>	33
4.1.1 <i>Structure, morphology and composition</i>	33
4.1.2 <i>Optical and electrical properties</i>	40
4.2. <u>WO_x FILMS BY GLAD + RGPP</u>	46
4.2.1 <i>Structure and morphology</i>	46
4.2.2 <i>Optical properties</i>	51
4.2.3 <i>Electrical properties</i>	57
4.3. <u>CONCLUSION</u>	63
5. CHAPTER 4: WO_x FILMS BY GLAD CO-SPUTTERING	65
5.1. <u>FROM TWO W TARGETS</u>	65
5.1.1 <i>Structure and morphology by classical O₂ injection</i>	65
5.1.2 <i>O₂ injection close to one W target</i>	68
5.2. <u>FROM W TARGET AND WO₃ TARGET</u>	70
5.2.1 <i>Varying the DC sputtering of W target</i>	71
a) <i>Structure and morphology</i>	71
b) <i>Electrical properties</i>	73
5.2.2 <i>Varying the RF sputtering of WO₃ target</i>	75
a) <i>Structure and morphology</i>	75
b) <i>Electrical properties</i>	78
5.3. <u>CONCLUSION</u>	79
6. CHAPTER 5: GAS SENSING PERFORMANCES	81
6.1. <u>WO_x FILMS WITH ONE W TARGET</u>	82
6.1.1 <i>Role of oxygen</i>	82
6.1.2 <i>Exploiting the GLAD approach</i>	84
6.2. <u>WO_x FILMS WITH W AND WO₃ CO-SPUTTERED TARGETS</u>	92
6.2.1 <i>Annealing treatment before gas sensing</i>	92
6.2.2 <i>Sensing performances</i>	97

6.3.	<u>CONCLUSION</u>	100
7.	<u>CONCLUSIONS AND PERSPECTIVES</u>	101
8.	<u>REFERENCES</u>	105
9.	<u>APPENDICES</u>	113
9.1.	<u>CURRICULUM VITAE</u>	113
9.2.	<u>LIST OF PUBLICATIONS AND COMMUNICATIONS</u>	114

1. General Introduction

Thin films are the workhorses of much today's technology. Entire technologies, from integrated circuits to spacecraft to candy wrappers are strongly dependent on thin films. In many cases, a scientifically observed property of thin films led to a creation of an entirely new field of technology. During the last decades, thin films and particularly nanostructured coatings, have been transformed from a laboratory curiosity to become a multi-billion euros industry worldwide.

Nanostructuring of transition metal oxide thin films has been considered as an attractive field, which differs from bulk materials since they have high surface-to-volume ratio. These nanostructured thin films can be categorized by their dimension: i) one dimensional nanostructures, such as nanowires, nanotubes, and nanobelts, ii) two dimensional nanostructures, which are usually used in lithographic techniques with a mask and then etched (hole type) [1] or growth (nanowire matrix) [2] to fabricate thin films, or deposit alternative multilayers nanostructures [3], or zigzag structures and iii) three dimensional nanostructures, which can be prepared by using templates (3 dimensionally ordered macro-porous systems) [4] or direct write lithography and refine deposited (square spiral arrays) [5]. Combined with the character of transition metal oxides, these thin films have exciting potential applications such as chemical gas sensors [6], photodegradation [7], catalysts [8], photonic crystals [9], resistant coatings [10].

For the last years, numerous binary metal oxide thin films have been produced by reactive sputtering since this process is an attractive way to efficiently prepare semi-conducting and dielectric materials [11–15]. There has been a continuous improvement towards fabricating tunable oxide coatings playing with the deposition parameters. Among the large panel of binary oxides, the growth and characterization of tungsten-based compounds have extensively been studied due to their remarkable optical, electrical and chemical properties [16–18]. Thus these W-O films have been used in a range of applications such as antireflective and electrochromic coatings [19], gas sensors, catalysts [20] and so on. However, the majority of the reported investigations has been focused on stoichiometric WO_3 or oxygen-deficient

WO_{3-x} thin films [21,22]. A few studies have been devoted to the behaviors of WO_x thin films with a wide range of oxygen concentrations, i.e. $0 < x < 3.0$ [23]. This lack of knowledge is even more significant for W-O thin films prepared by reactive sputtering. Basically, when a metallic target like tungsten is sputtered in a reactive atmosphere (e.g. argon + oxygen gases), the process abruptly drops in a reactive mode as the oxygen mass flow is increasingly supplied [24]. This typical nonlinear effect of the reactive sputtering process restrains the range of reachable compositions. Thus, it may become a challenge to accurately control the oxygen and tungsten elemental concentrations in the films without using feedback control systems or high pumping speeds [25–27]. Recently, the Reactive Gas Pulsing Process (RGPP) [28] was developed to deposit metallic oxide thin films with tunable compositions. It was successfully used to reach titanium, niobium, tantalum, iron, zirconium and W-O and oxynitride thin films with a wide range of metalloid contents [10,29–34]. That is the reason why this method has been chosen in this thesis as a chemical approach to deposit W-O thin films by reactive sputtering. The RGPP was implemented to produce adjustable oxygen and tungsten atomic concentrations in the films. The strategy consisted in pulsing the oxygen gas during the sputter deposition, in order to alternate the process between metallic and oxidized sputtering modes and thus to get various WO_x compounds from metallic W to over-stoichiometric WO₃ compounds. The injection time of the oxygen gas was systematically changed, so as to reach a regular and well-controlled evolution of the growth rate, composition, optical behaviors and electronic transport properties. A gradual transition from metallic to insulating behaviors was finally demonstrated and connected to a single pulsing parameter, namely the duty cycle, and thus to the oxygen concentration in the films.

The design and fabrication of thin films have been the cornerstone to technological advances in many fields. The capability to further engineer film properties through physical structuring on the micro- and nano-scale and by an accurate control of architectures enable new opportunities for performance improvements. Among the structuring toolbox, vacuum processes involving the Glancing Angle Deposition (GLAD) technique recently appeared as an attractive approach because it easily creates a wide range of architectures (tilted columns, zigzags, spirals and so on) at the nanometric scale [35]. The

basis can be explained by initial numbers of nucleation on the substrate making self-shadowing incident angle particle flux. The nucleation sites keep growing and form voids between two columns. Therefore, during the GLAD process, there are two key parameters, which need to be mentioned: one is the incident angle α which is defined by the angle between the target normal and the substrate normal; the other one is the rotating speed ϕ , which is defined by a computer-controlled rotating speed of the substrate holder. The incident angle α can be changed from 0 to 90 °, with a relevant column angle obtained from Tait's investigation [36] explaining the empirical correlation between incident angle α and column angle β . The rotating speed ϕ can produce different architectures. Zigzag structures can be prepared when the substrate holder rotates 180° after a certain period. Spiral structures can be prepared when the substrate holder rotates at a given speed, and the pitch height and coil diameter can be designed by the ratio between deposition rate and rotating speed.

Nanostructured thin films have found applications in many fields, exploiting the adjustable properties from the chemical approach (e.g. RGPP) or the physical structuring (e.g. GLAD). In this thesis, the focus will be on the use of W-O thin films as an active layer for gas sensors. Two gases have been chosen as pollutants: ozone and dodecane. Ozone is an oxidizing gas, which can cause the decreasing of oxygen vacancies concentration in the film, leading to an n-type sensor with a high resistivity. Ozone is the typical air pollutant, which is widely investigated in gas sensor field [37–44]. Jet fuels has large amount of compounds, but basic from the conception, researchers prepare to use small hydrocarbons (dodecane could represent petroleum-based jet fuel) instead of large hydrocarbon molecules to investigate such as reaction kinetic [45] or gas leak monitor [46]. Dodecane is also typical of reduction air pollution, which could increase the depletion layer of oxygen vacancies concentration, giving rise to a resistivity decrease for an n-type gas sensor.

In this thesis, we report on the deposited W-O thin films prepared by RGPP, GLAD and co-sputtering. The strategy consists in clarifying the role of oxygen gas during the sputter deposition in order to find out which composition of thin film exhibits the best gas sensing performances. Then, GLAD is implemented to get various architectures such as columnar, zigzag and spiral microstructures. We show

that nanostructuring of W-O thin films allows sensing either oxidizing, or reducing chemical compound and how the films' architecture leads to a detection enhancement. To this aim, ozone and dodecane have been chosen since they exhibit oxidizing and reducing behaviors, respectively. In order to produce nanostructured films, two combined strategies have been involved to play with microstructure and composition of sputter-deposited W-O thin films. Finally, GLAD co-sputtering was used, to fabricate thin films with a low resistivity and an adequate electronic transport.

In chapter 1, W-O compounds are described as the starting materials with attractive tunable properties so as to apply as an active layer for gas sensors. Advantage of thin films compared to the conventional bulk materials is explained. Different methods to prepare W-O thin films are presented and, for each one, a few examples are given with more detailed information. Other works devoted to WO_x films applied for gas sensors prepared by RGPP and GLAD techniques are mentioned and tested under different gases.

In chapter 2, all facilities and instruments used for the thesis are described, such as sputtering systems for the deposition of W-O thin films, morphologies and structured characterization by electronic microscopy, X-ray diffraction, resistivity and optical measurements. Experimental details are developed for the gas sensing tests.

In chapter 3, W-O thin films are prepared from one W target by RGPP using different duty cycles. Electrical resistivity and optical transmittance are used to evaluate oxygen contents in WO_x films as a function of duty cycle, the latter being announced as a key parameter influencing the characteristic of W-O thin films. Then, the GLAD technique is developed focusing on two more additional parameters: the incident angle α and the rotating speed ϕ . By controlling these two parameters, various architectures are fabricated. Optical and electrical properties are investigated as the function of the duty cycle dc and incident angle α .

In chapter 4, a two targets co-sputtering system is implemented. Firstly, two tungsten targets are co-sputtered with a systematic change of the current applied on each target. The idea is to produce two components W/ WO_3 columnar microstructures. A ring close to one W target is used for the oxygen

injection and its influence is discussed. Then, tungsten trioxide RF sputtered target is installed instead of one tungsten DC sputtered target. The current of the tungsten target I_w and the WO_3 self-bias potential U_{WO_3} are separately modified to produce co-sputtered WO_x thin films.

In chapter 5, some selected thin films prepared by RGPP, RGPP+GLAD or RGPP+GLAD co-sputtering are exploited as active layers for gas sensors. Ozone (oxidizing chemical compound) and dodecane (reducing chemical compound) are tested as pollutants. Influence of oxygen contents in thin film and microstructure are discussed.

2. Chapter 1: State-of-the-art

In this first chapter, the author intends to propose a short overview of W-O compounds and thin films. Methods commonly developed for depositing WO_x thin films are described and sputtering processes involving RGPP and GLAD approaches are discussed. Some recent investigations focused on WO_x as an active layer for gas sensors are finally reported with an emphasis on W-Os produced by GLAD.

2.1. W-O compounds and thin films

Several W-O compounds can be reached as a function of the oxygen and tungsten concentrations (Figure 2.1) [47].

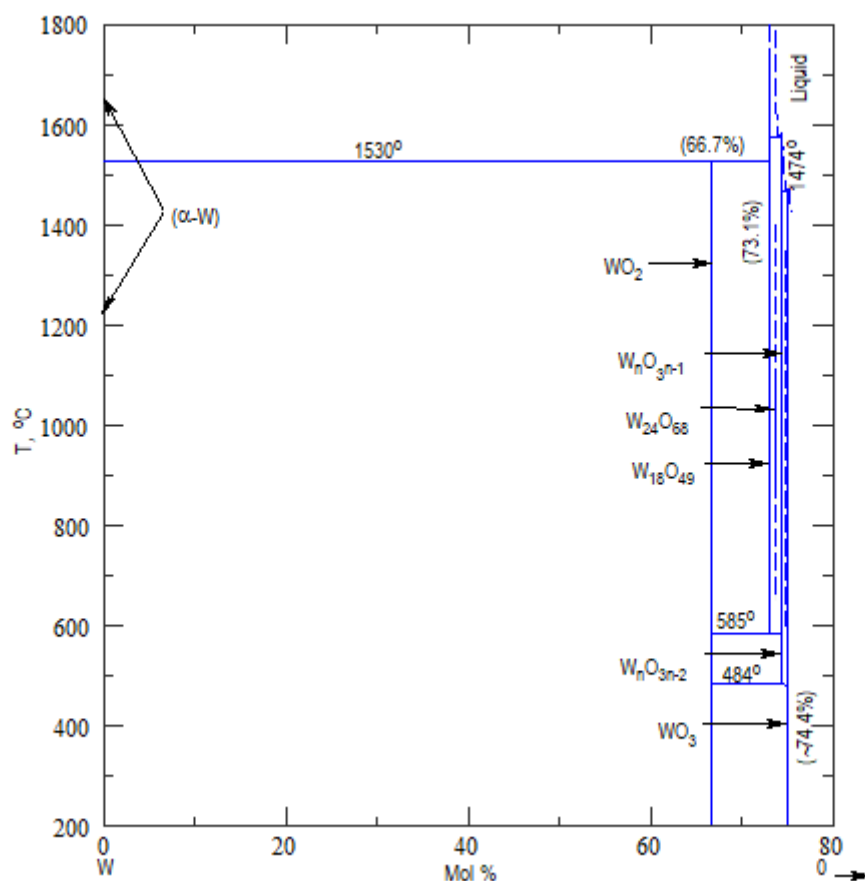


Figure 2.1 Phase diagram of the W-O system [47].

Changing the oxygen content leads to typical stable phases such as W, WO_2 , WO_3 , or Magnéli phases such as W_3O_8 , W_5O_{14} , $W_{18}O_{49}$, $W_{17}O_{47}$, $W_{20}O_{58}$, and $W_{25}O_{73}$, or other compounds with chemical formula

W_nO_{3n-1} or W_nO_{3n-2} . WO_3 usually exhibits four phases vs. temperature: tetragonal structure, which is thermodynamically stable at temperatures above 740 °C, orthorhombic structure stable for temperatures in-between 330 - 740 °C, monoclinic structure stable for temperatures in-between 17 - 330 °C and triclinic structure stable for temperatures below 17 °C.

Among the various metal oxides, tungsten trioxide is a n-type semiconductor, which has a wide band-gap (2.4–2.8 eV) [48], and attracted the scientific community due to sensing properties. For n-type semiconductors, resistivity is increased when exposed to oxidizing gases (O_3 , NO_2), or decreased with reducing gases (H_2 , CO , NH_3). A sensing effect is based on electronic exchanges between gas and metal oxide surface. Tungsten oxide exhibits good sensing properties such as a low detection gas concentration, a low operation temperature, fast response and recovery times, and a high sensitivity. Tungsten oxide sensors also show excellent performances towards pollutants such as O_3 [43], NO_2 [49], SO_2 , H_2S [50], H_2 [51], CO [52], NH_3 [53], hydrazine [54], acetone [55]. Its electronic properties are thus used during gas detection by recording the change of electrical resistance. It is well known that the mechanism of sensing performances is related to the surface-to-volume ratio (or surface area). Therefore surfaces exhibiting high roughness [38,40,53,56] and interfaces such as nano-necks [57,58] or junctions [53,59–61] play a key role in gas sensing performances.

2.2. Methods for producing WO_x films

Various methods have ever been applied for preparing WO_x films, such as sol-gel, hydrothermal, electrospinning, and PVD and CVD techniques. Several selected examples for each method are described below.

2.1.1 Sol-gel method

Sol-gel method can produce metal inorganic compounds, metal organic compounds or a mixture of these two compounds, through the hydrolysis polycondensation, gelation and annealing processes (preparation of oxides or other compounds). Maity *et al.* [62] used tungsten precursor sol from tungsten (V) ethoxide in propan-2-ol and added HCl drop by drop during stirring. Then the sol was aged overnight before

depositing with a high-speed spin coating. The coating was moved into a furnace at 350 °C for 5 min to remove organic species. The procedure was repeated until the required films thickness. Mane *et al.* [49] used a sol-gel method to prepare WO₃ nanoparticles. They mixed and stirred tungsten hexachloride and methanol at 60 °C for 3 h to obtain the gel. Then the gel was heated to obtain a powder. It was washed, dried, and annealed at 700° C for 1 h. Finally, the powder was dissolved in m-cresol (solvent) and deposited on substrate by using drop-casting method.

2.1.2 Hydrothermal method

Hydrothermal method refers to a special sealed reactor, by using aqueous solution as a reaction medium. The reaction system was heated to a critical temperature (or close to the critical temperature), to produce high-pressure environment for inorganic synthesis. It was also developed to prepare nanowires (or nanorods) arrays of WO₃ thin films [63–65]. Zhang *et al.* [66] used Na₂WO₄·2H₂O solution as precursor, and HNO₃ was added drop by drop during stirring. Then the substrate was mixed with the solution in the Teflon-lined stainless-steel autoclave at constant temperature for 12 h with hydrothermal method. Finally, the substrate was washed by distilled water and ethanol for several times, and dried at 50 °C. Liu *et al.* [67] started with H₂WO₄ solution by adding H₂O₂ drop by drop with strong stirring, then mixed with NH₄Cl solution. Different morphologies of WO₃ nanostructures were controlled by different ratios of H₂WO₄ precursor, ethanol and deionized water. The solution was filled into Teflon-lined stainless-steel autoclave with vertically oriented substrate, then sealed and kept at 180 °C for 5 h. Finally, the substrate was cleaned by deionized water and ethanol and dried at 60 °C for 12 h. Zhang *et al.* [68,69] employed nonstoichiometric WO₃ nanoparticles mixed with an organic solvent to prepare paste, which was applied with a screen printing technique, then drying at 80 °C for 15 min, sintered at 350 °C to remove organic species and calcinated at 600 °C for 2 h to improve the mechanical strength.

2.1.3 Electrospinning method

Electrospinning method forces the surface of precursor to overcome the surface tension under electric field. It provides a simple and an efficient way for the fabrication of nanometer scale fibers. Chi *et al.* [55] developed single capillary electrospinning method. First, tungsten chloride as a precursor was

mixed with N, N-dimethylformamide stirred for 30 min. Then, polyvinylpyrrolidone was added in the above solution and was stirred for 30 min. Afterwards, ethanol was added and stirred for 10 h. The precursor solution was filled into a syringe and a high-voltage power supply was connected to the pinhead. The fibers collected on the substrate were calcinated at 550 °C for 3 h. Bai *et al.* [70] implemented an electrospinning method to prepare Cu-doped WO₃ hollow fibers. H₂WO₄ was added into a mixed solvent (ethanol and H₂O₂) with ultrasonication for 40 min. Then citric acid and NH₃·H₂O aqueous solution were added drop by drop during stirring. Cu(NO₃)₂·3H₂O as copper source was added into the sol. The latter was filled into a syringe pump and the pinhead high voltage was applied. Then the hollow fibers were collected and sintered in air at 500 °C for 1 h.

2.1.4 Physical vapor deposition method

It is difficult to obtain large area homogeneous thin films by wet-chemical reaction. Then the physical vapor deposition methods were applied for preparation of W-O films. Zhao *et al.* [51] used Supersonic Cluster Beam Deposition (SCBD) technology to prepare tungsten films. An argon pulsing flow passes through a rotating tungsten rod. Then the time lag of electric pulses ignites the plasma of tungsten, which makes W atoms further to aggregate and produces W nanoclusters. The Ar flow carries the nanoclusters and passes through an expansion chamber, due to a pressure gradient. It leads to a supersonic expansion. Then the nanoclusters flow passes an aerodynamic filter, to align the tungsten nanoclusters deposited on the substrate. Vuong *et al.* [60] prepared WO₃ nanowire thin films on single-walled carbon nanotubes template. First, they deposited platinum and titanium layers on the substrate as the electrodes. Then graphite rod as carbon source fabricated single-walled carbon nanotubes by an arc current in hydrogen gas. Last, DC magnetron sputter W was deposited on template and the thin films were put into an oven so as to oxidize the W to WO₃ and burn the template. Stoycheva *et al.* [40] developed aerosol assisted chemical vapor deposition (AACVD) to synthesize WO₃ thin films. Dissolving hexaphenoxide in a mixture of acetone and toluene, a shadow mask was used to protect blank membrane. W-O films were grown on the membrane at 350, 450, and 500 °C. After deposition, the films were annealed in air at 500 °C for 2 h. Qin *et al.* [61] used RF magnetron to sputter a metallic W target. Under 150 Pa at 650 °C with

Ar+ O₂ gas mixture, aligned W₁₈O₄₉ nanowire arrays were prepared on the W film in a tube furnace. Kumar *et al.* [71] prepared WO₃ thin films by thermal evaporation. At first, the commercial grade WO₃ powder was sintered into pellets, then using a high-energy electron beam (6 keV) to evaporate on the substrate. Afterwards, all the thin films were annealed at a certain temperature for 1 h. Parreira *et al.* [72] deposited W-O by DC reactive magnetron sputtering. Various partial pressures of oxygen were used. Oxygen content was systematically changed from 0 to 75 %. Deposition rate and X-ray diffraction were recorded vs. an increasing oxygen content. An optimized rate appears for the stoichiometric WO₃ phase. The deposition rate increased before this optimum and decreased after, which was explained by the poisoning effect of the tungsten target. Crystalline phases were produced α -W, β -W, amorphous phase, and quasi-amorphous structure. The adhesion of coating was also investigated. Parreira *et al.* [73] continued the research on DC reactive magnetron sputtering of the W-O system. Thermal stability of the W-O thin films was investigated by various annealing treatments and with or without neutral atmospheres. The results showed that sub-stoichiometric compounds start to oxidize at 600 °C, and under neutral atmosphere, crystallization appears at 700 °C and follows the phase diagram. Li *et al.* [17] prepared W-O films under various oxygen flow rates by DC reactive magnetron sputtering. As-deposited films were metal-rich WO_x to amorphous WO₃ compounds. The color changed from dark blue to transparent while oxygen supply increased during deposition. XPS indicated W⁴⁺, W⁵⁺, W⁶⁺ ions in the films. The occurrence of W⁵⁺ was attributed to the amorphous structure of the films. Optical bandgap widened for films deposited under high oxygen flow rate.

2.3. WO_x films by RGPP

Parreira *et al.* [33] developed the Reactive Gas Pulsing Process for the W-O system. They fixed the pulsing period of oxygen $P = 10$ s or 50 s and various T_{ON} times from 3 to 9 s or 25 to 45 s, respectively. They also kept duty cycle $dc = 0.9$ with various periods P (from 10 to 100 s). All films exhibited a multilayered structure, which consisted of W-rich and O-rich periodic nanolayers. The main idea of RGPP is to alternate the reactive sputtering between metallic and compound sputtering modes. The

deposition rate was decreased when the W target was fully poisoned. The authors suggested a hysteresis loop of W target potential and total pressure (Figure 2.2), which is rather a drift of the process.

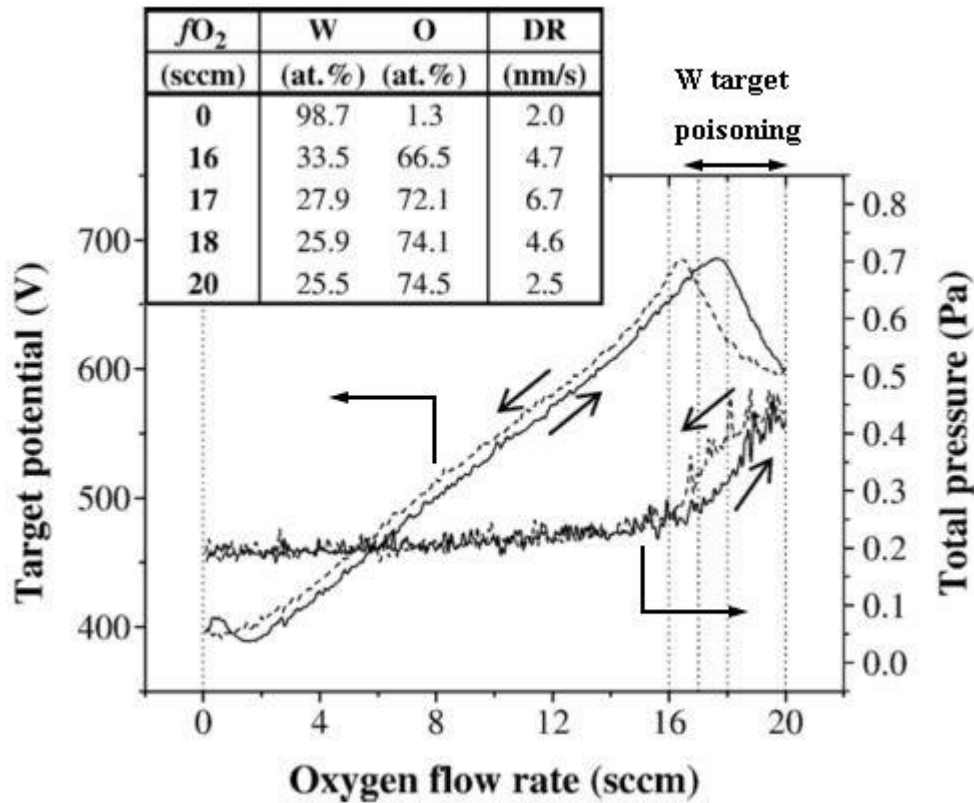


Figure 2.2 Evolution of the target potential and total pressure vs. oxygen flow rate during reactive sputtering [33].

By using RGPP, a significant increase of the deposition rate was measured and the deposition of compounds with controllable compositions. The structure was systematically changed from α -W or β -W to nanocrystalline WO_3 phase only modifying the T_{ON} time.

Polcar *et al.* [74] used RGPP to obtain graded refractive index coatings, leading to films with different colors. Seven layers of a multilayered structure was built with the same pulsing period P but various duty cycles dc by adjusting the deposition time. Two samples with two series graded coatings were prepared. Reflectance vs. wavelength measurements were compared with simulations as shown in Figure 2.3.

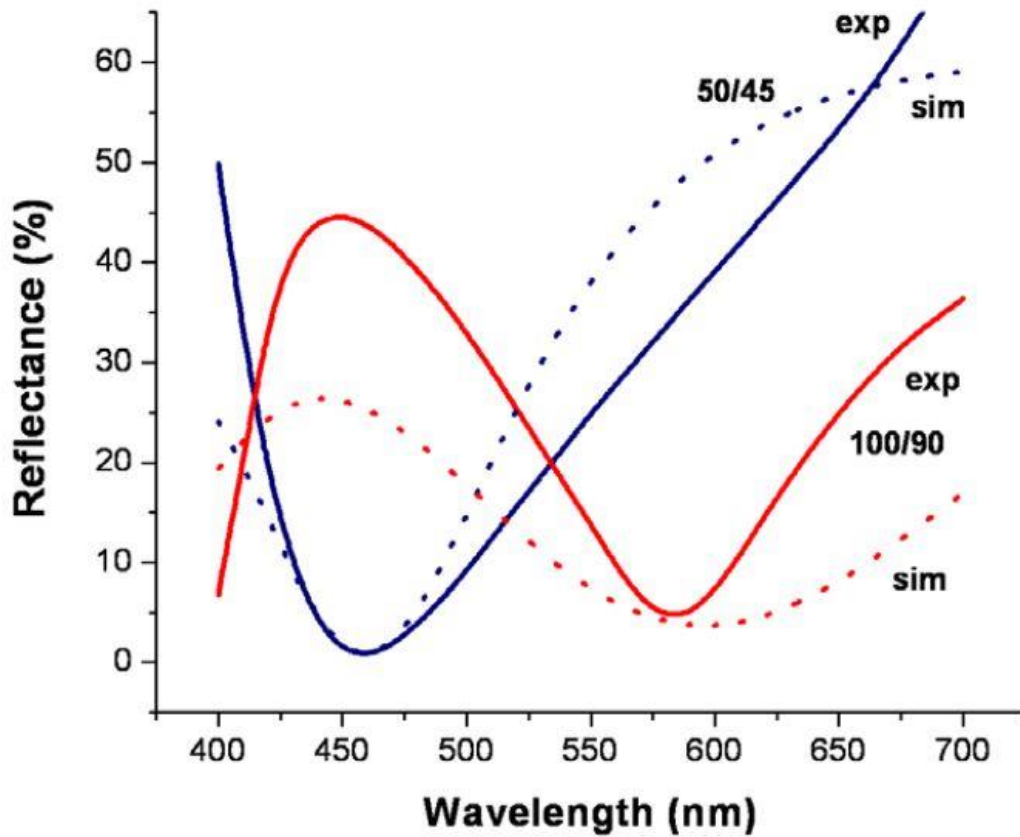


Figure 2.3 Reflectance spectra in the visible range of W-O thin films sputter deposited by RGPP. Comparison between simulation and experiment for coatings deposited with different periods $P = 50$ and 100 s, and T_{ON} time = 45 and 90 s. [74]

Position and magnitude of the reflectance peak can be simulated. Controlling the sputtering conditions, such as gas flow rate or sputtering power, a desired thin film color can be achieved.

2.4. WO_x films by GLAD

Charles *et al.* [75] deposited WO₃ thin film by using DC reactive magnetron sputtering from a W target in Ar+ O₂ gas mixture. They first investigated the influence of incident angle α of the particle flux on optical properties, such as refractive index, extinction coefficient, optical band gap, Urbach energy and birefringence. They showed that the column angle β was changed from 0 to 54° as the incident angle α was systematically increased from 0 to 80°. When the incident angle α was higher than 50°, a clearly columnar microstructure was observed. Refractive index at 550 nm dropped from 2.11 to 1.90 as a function of the incident angle. This optical property change was assigned to the increasing porous architecture coming from the shadowing effect during deposition.

More recently, Charles *et al.* also [76] studied the influence of different kinds of nanostructures on optical properties. By using the same deposition conditions, WO₃ thin films were prepared with different incident angles and different zigzag periods. Refractive index and birefringence were investigated by experiments and simulations (MIT's MEEP code [77]). The maximum refractive index was obtained when the number of zigzag periods $N = 4$ (Figure 2.4), which could be considered as the less voided films produced when the period increases. A higher number of zigzag periods makes the columns trend to perpendicular columns to the substrate and thus a similar porous structure as tilted column.

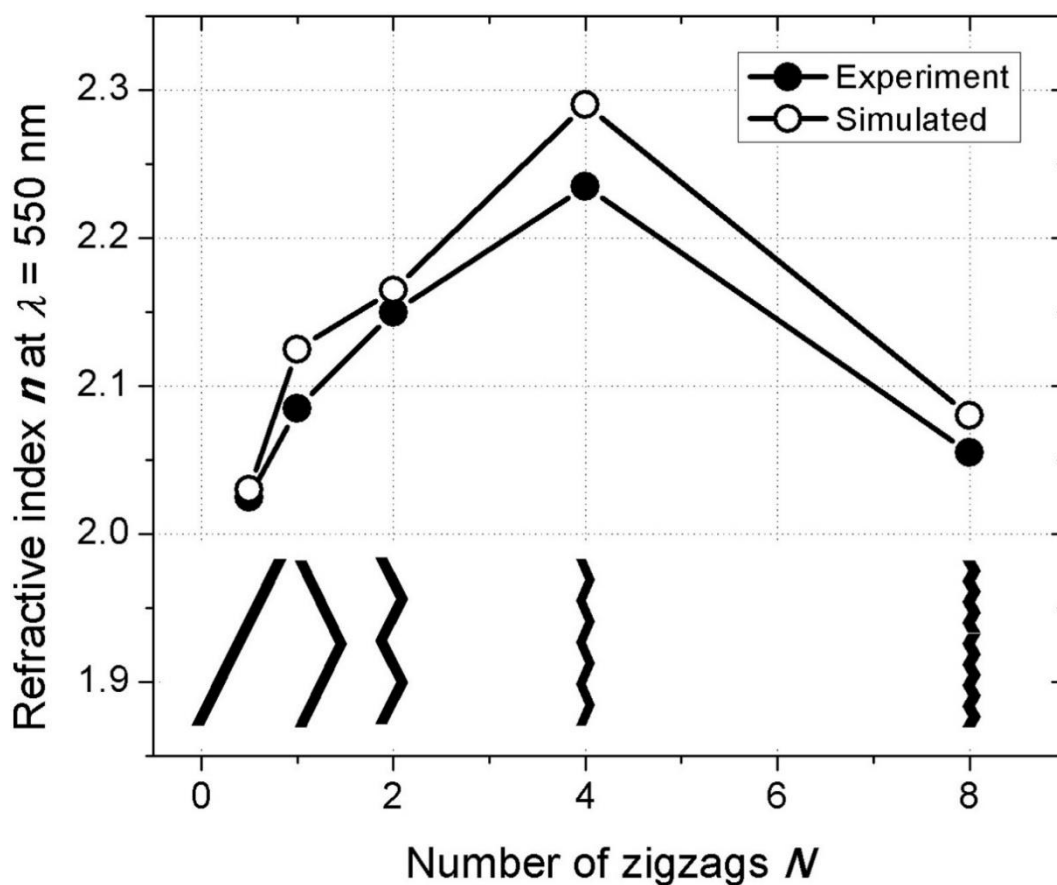


Figure 2.4 Comparison between experimental and simulated refractive indices n at $\lambda = 550$ nm for zigzag structures with $N = 0.5, 1, 2, 4$ and 8 zigzags [76].

Deniz *et al.* [78] fabricated tungsten and tungsten trioxide films by GLAD with an incident angle $\alpha = 80^\circ$. W and WO₃ films were grown in Ar or Ar + O₂ gas mixtures, respectively. The films were annealed at 500 °C in air for 5 hours. The annealing treatment did not change the morphology of the W nanorods, but it significantly transformed the WO₃ nanorods into a nanoporous network. Simple cubic β -W phase and amorphous phase were obtained before annealing treatment, whereas films crystallized following

the triclinic/monoclinic WO_3 phase after the annealing treatment. Similarly, the XPS analysis of WO_3 films showed that $\text{W}4f$ peaks shift from sub-stoichiometric to stoichiometric WO_3 compound after annealing (Figure 2.5).

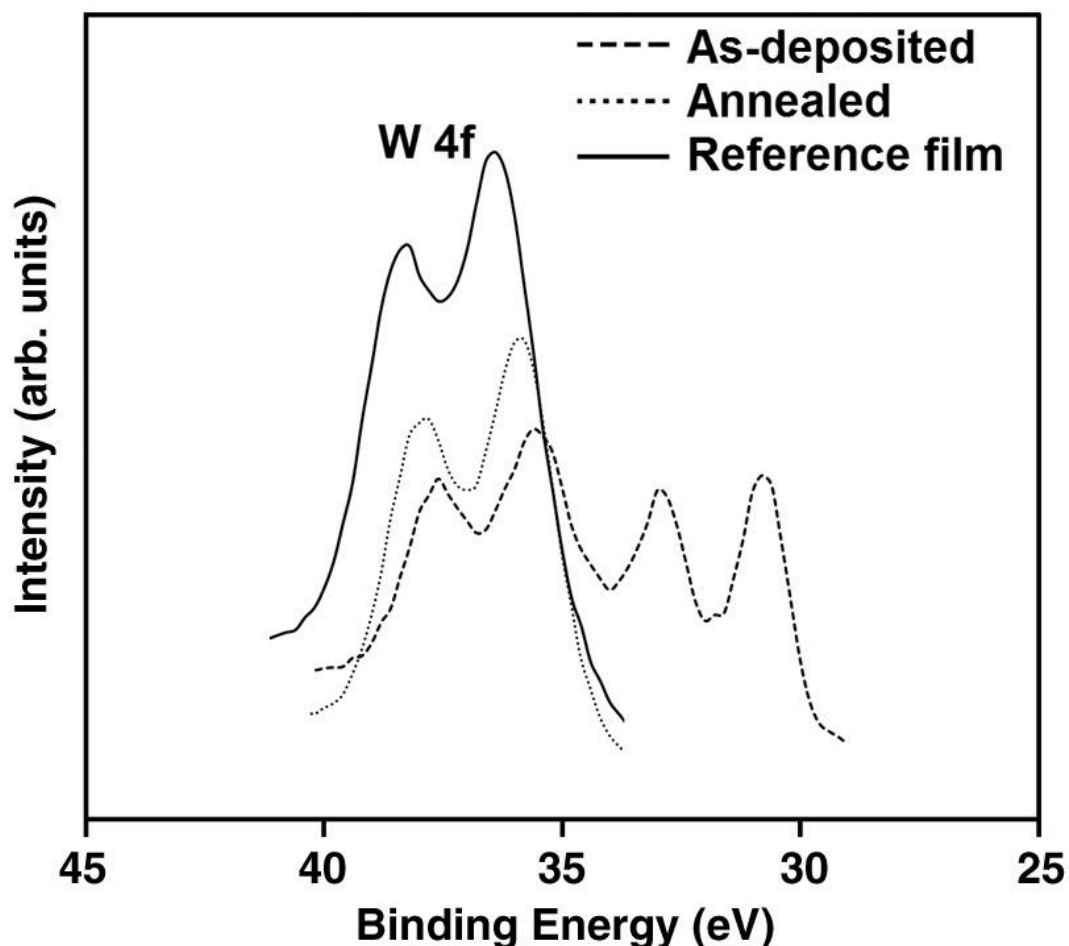


Figure 2.5 High resolution XPS W 4f peaks from as-deposited and post-deposition air annealed WO_3 films [78].

2.5. WO_x films as an active layer for gas sensors

Horprathum *et al.* [79] made WO_3 gas sensors by DC magnetron sputtering in Ar + O_2 gas mixture. By using GLAD or without GLAD, incident angle was set at 85° and 0° , respectively. All the thin films were annealed in air for 3 hours at 400 and 500 $^\circ\text{C}$. Inclined WO_3 nanorod thin films exhibited a better NO_2 response compared to dense films, and such WO_3 nanorods annealed at 500 $^\circ\text{C}$ showed the most sensitive response using 0.1 ppm NO_2 at an operating temperature of 250 $^\circ\text{C}$. In Figure 2.6, the response of the dense film is lower than that of the nanorods. Films annealed at 400 $^\circ\text{C}$ exhibit a lower response than those annealed at 500 $^\circ\text{C}$. Such sensing performances were explained assuming that the nanorod

architecture has a large surface area, and the highest annealing temperature (500 °C) made these films as a highly porous cross-linked WO₃ nanonetwork.

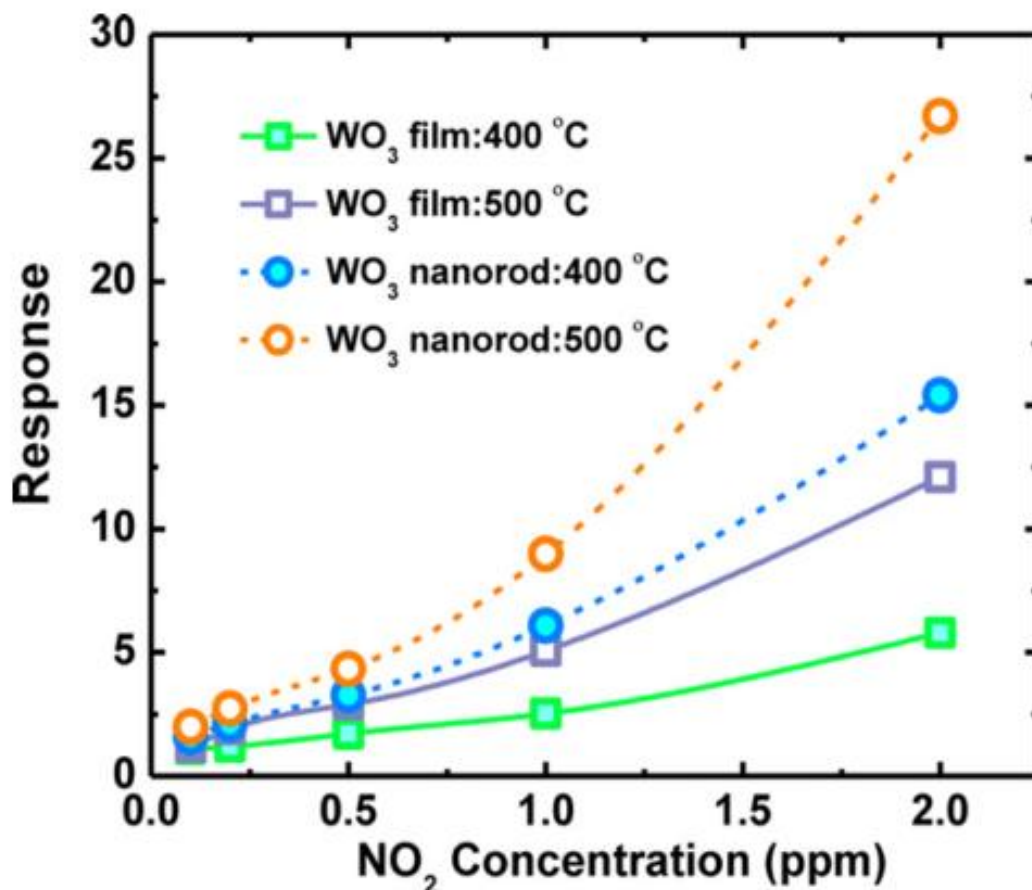


Figure 2.6 Response vs. NO₂ concentration with dense and nanorod thin films, annealed at 400 and 500 °C [79].

Moon *et al.* [80] prepared their sensors by using RF sputtering with an incident angle of 85°. Sensors were annealed in air at 500 °C for 60 min. They compared with planar thin films fabricated with a normal incident angle ($\alpha = 0^\circ$) with the same films thickness. NO₂ gas was mainly tested, but other target gases like C₂H₅OH (ethanol), CH₃COCH₃ (acetone), NH₃, H₂, SO₂ and CO were also investigated (Figure 2.7). The lowest detected concentration was 1 ppm. They used self-heated sensors, which means that the resistance was measured under different bias voltages instead of operating temperatures. In Figure 2.7, the response vs. concentration is shown at the same bias voltage $V_b = 5$ V, which is a different standard compared to the operating temperature as commonly used by most researchers.

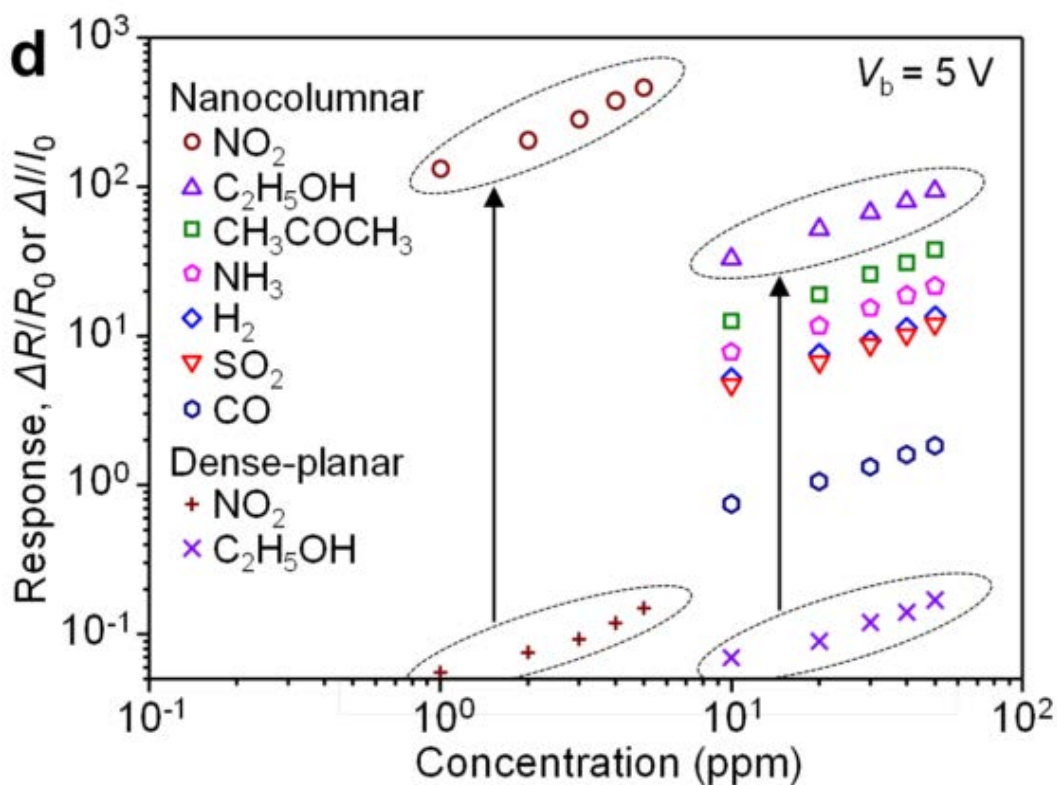


Figure 2.7 Response of the dense-planar and nanocolumnar WO_3 thin film sensors as a function of gas concentration for various target gases at bias voltage $V_b = 5\text{ V}$ [80].

More recently, the same group of Moon *et al.* [57] used RF sputtering with an incident angle of 86° to prepare gas sensor. The surface area was calculated to be $350\text{ m}^2\text{ g}^{-1}$, which is 12 times higher than WO_3 dense thin films. The sensor was sintered at 550°C for 60 min. 5 ppm NO_2 and 50 ppm C_2H_5OH , and 50 ppm CH_3COCH_3 were injected as target gases as a function of different operating temperatures. They showed that at 200°C , the ratio of response between NO_2/C_2H_5OH or CH_3COCH_3 was largest, which means that, at this optimal temperature, WO_3 sensor has the best selectivity. The sensitivity and selectivity improvements were connected to the porous structure with nano-necks, which has double barrier-Schottky junctions and fully depletion areas.

Wisitsoorat *et al.* [81] prepared WO_3 sensors via RF sputtering with an incident angle of 85° . They used different deposition times to fabricate variable thin film thicknesses. All films were annealed in air at 450°C for 2 h. C_2H_5OH and NO_2 were selected as target gases. The larger nanorods have smaller depletion layer thickness (Figure 2.8). The thinnest films have a larger response to reducing gases. Oxidizing gases made deeper additional depletion region of films involved in the sensing process, which

means that a thicker thin film expresses a better response [82]. The same group deposited Pd layer 2.5 nm thick as a catalyst on WO₃ surface. The deposited films were annealed in air at 400 °C for 3 h. Optical gas sensing absorbance was investigated under H₂ or synthetic air. With an inclined structure, Pd catalyst layer exhibited a larger contact area to WO₃ nanorods, which had also a much larger absorbance change than dense films (Figure 2.8).

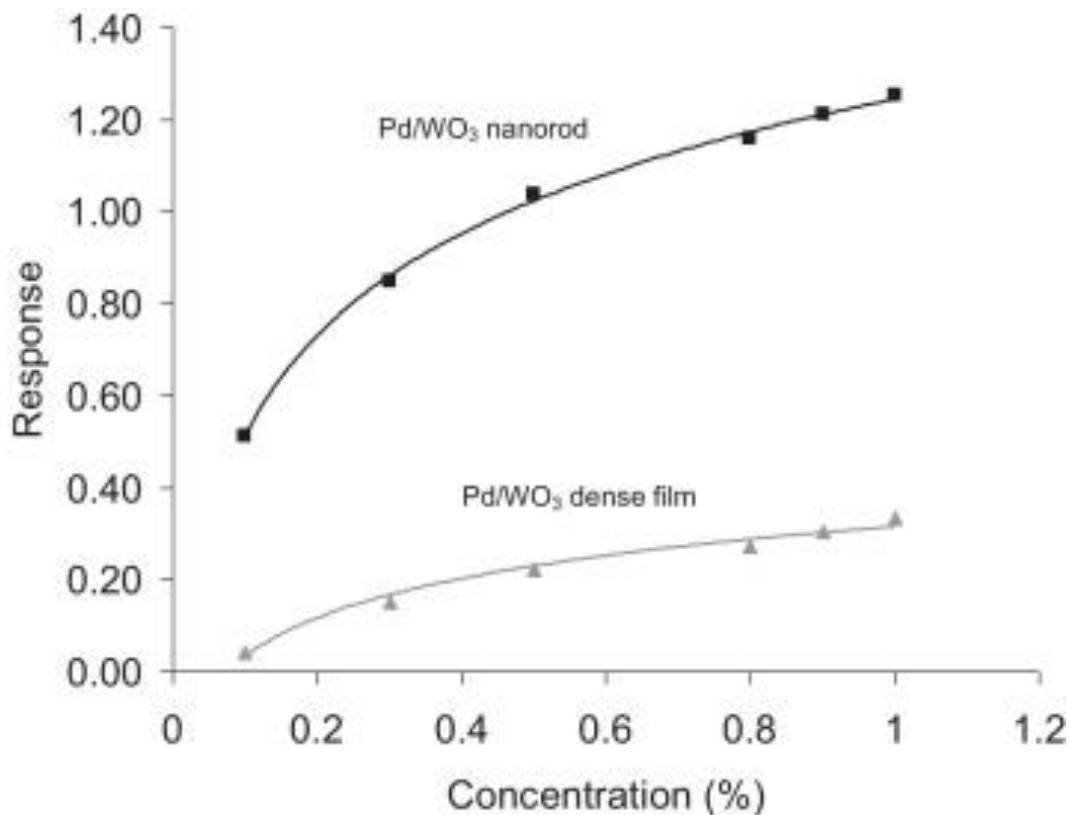


Figure 2.8 Sensor response of Pd/WO₃ dense films and Pd/WO₃ nanorods vs. various H₂ concentrations at 100 °C [81].

Wongchoosuk *et al.* [83] used RF sputtering at an incident angle of 85 °. They injected acetylene (C₂H₂) as a carbon source into a gas mixture during WO₃ deposition to prepare carbon-doped WO₃ nanorods. All the films were annealed at 400 °C for 3 h. NO₂ was selected as the target gas (Figure 2.9).

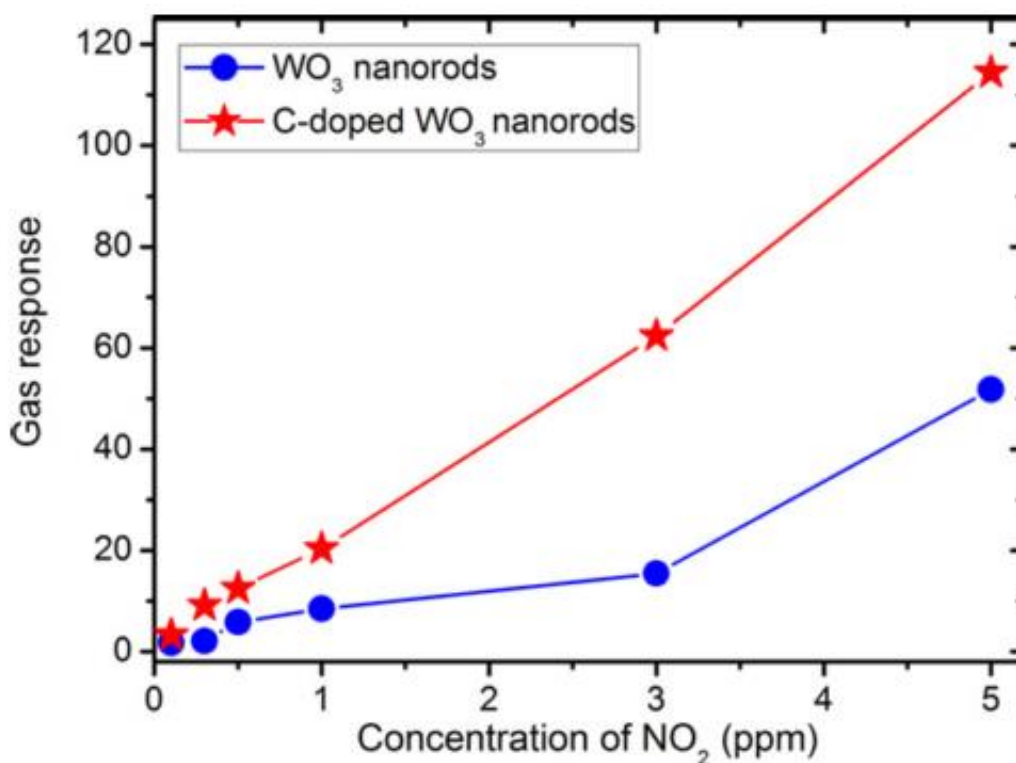


Figure 2.9 Gas responses of carbon-doped and undoped WO₃ nanorods gas sensors to different concentrations of NO₂ at the operating temperature of 150 °C [83].

They showed that carbon-doped WO₃ films decreased the activation energy and increased the depletion layer thickness. Such a doping led to a better response, recovery time, operating temperature and selectivity.

2.6. Conclusion

The production of W-O compounds and thin films have been abundantly reported in the literature. It is nearly a challenging task to get an exhaustive review about physical and chemical deposition methods in liquid and/or vacuum environments leading to the growth of WO_x thin films. Among the deposition methods, the reactive sputtering process is an attractive way to get tunable W-O thin films. The Reactive Gas Pulsing Process (RGPP) and the GLancing Angle Deposition (GLAD) have been unfrequently reported in the literature in spite of their potentiality to play with the nature and microstructure of the deposited metal oxides. Application of W-O as an active layer for gas sensing still remains an exciting

scientific topic, especially when the films architecture as well as its composition can be adjusted by the deposition process.

3. Chapter 2: Materials and methods

In this chapter, the author reports on a brief description of the sputter deposition methods. The GLAD techniques with one and two targets are described, as well as pulsing parameters involved by RGPP. Basic parameters of the characterization techniques are also given (rather than a detail description of principles, which can easily be found in the cited literature). Emphasis is put on the electrical resistivity and optical measurement setups. Sensor benches and operating conditions are finally explained for the detection of dodecane and ozone as pollutants.

3.1. Deposition setup and conditions

For W-O thin films, a homemade DC reactive magnetron sputtering system with a 40 L vacuum chamber was used. A 2-inch disk tungsten target (purity 99.9 at. %) was fixed 65 mm away from the center of the substrate holder as shown in Figure 3.1.

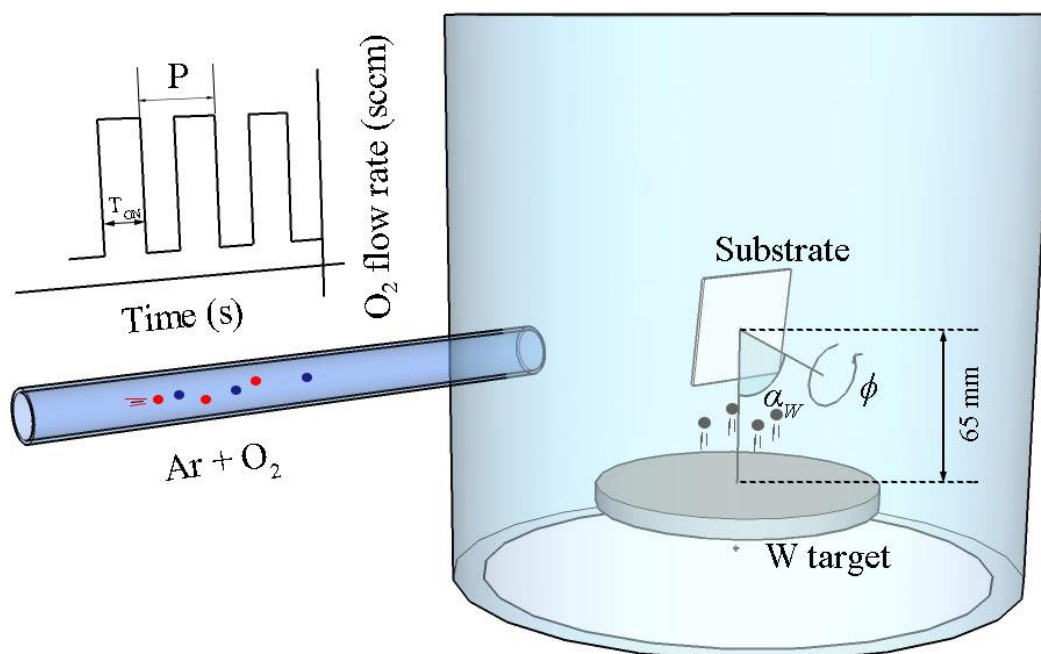


Figure 3.1: Illustration of the deposition system. All the following parameters can be adjusted: α = the angle of inclination of the W target compared to the normal of the substrate, ϕ = the rotating speed of the substrate holder, P = the pulsing period of oxygen gas (rectangular signal), T_{ON} = the time of injection of the oxygen gas.

Before depositing, an ultimate pressure about 10^{-8} mbar was reached with a turbomolecular pump backed by a mechanical pump. Target current was fixed at $I_W = 100$ mA (the corresponding current density was $J_W = 50$ A m $^{-2}$). A pre-sputtering time was applied for 5 min in order to remove the contamination layer on the target surface and stabilize the process. The argon flow rate was kept constant at $q_{Ar} = 1.2$ sccm. A constant pumping speed $S = 10$ L s $^{-1}$ was used leading to an argon partial pressure $p_{Ar} = 2.8 \times 10^{-3}$ mbar. Oxygen mass flow rate q_{O_2} was pulsed during W-O deposition by means of the Reactive Gas Pulsing Process (RGPP). A constant pulsing period $P = 16$ s was used. The maximum oxygen flow rate was $q_{O_2Max} = 2.4$ sccm and the minimum was $q_{O_2min} = 0$ sccm (to see later about the choice of P , q_{O_2Max} and q_{O_2min}). For all depositions, the substrate holder was grounded, and no external heating was added. The angle of inclination of the substrate holder, namely α , could be changed from 0 to 90° compared to the substrate normal. The rotating speed ϕ was computer-controlled and could be adjusted from 0 to several rev h $^{-1}$ (revolution per hour). A GLAD co-sputtering system was also used to deposit W-O thin films (Figure 3.2).

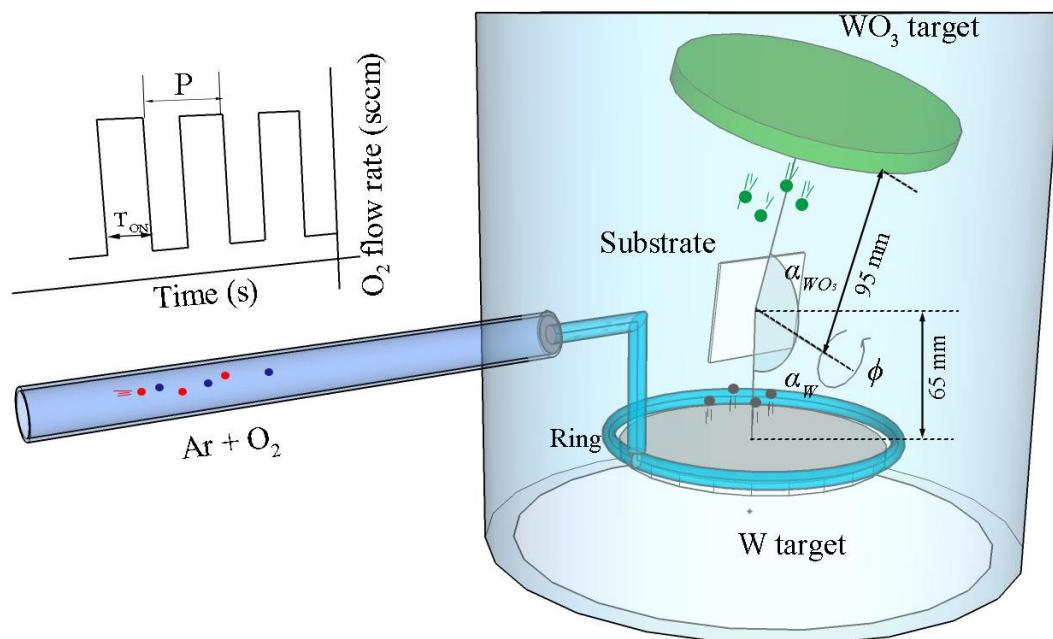


Figure 3.2: Illustration of the GLAD co-sputtering system. W target was DC sputtered, whereas WO_3 target was RF sputtered. Oxygen gas was pulsed, and argon was constantly supplied. α_W = the angle of inclination of W target compared to the normal of the substrate = 80° and α_{WO_3} = the angle of inclination of WO_3 target compared to the normal of the substrate = 80°.

A 2-inch disk tungsten trioxide (WO_3) target (purity 99.9 at. %) was fixed 95 mm away from the substrate holder. A RF generator was used to sputter it. W and WO_3 targets were focused on the center of the substrate holder and simultaneously sputtered using opposite and oblique angles $\alpha_W = \alpha_{\text{WO}_3} = 80^\circ$ from the substrate normal. The substrate holder was fixed for all GLAD co-sputtering ($\phi = 0 \text{ rev h}^{-1}$). The other deposition parameters were the same as those employed with a single W target DC sputtered. It is important to note that the argon flow rate had to be increased since 1.2 sccm did not allow maintaining a stable ignition of the RF plasma on WO_3 target (argon pressure was too low). As a result, the argon flow rate was set at $q_{\text{Ar}} = 3.2 \text{ sccm}$ leading to an argon partial pressure $p_{\text{Ar}} = 3.0 \times 10^{-3} \text{ mbar}$ and thus, stable co-sputtering conditions. The pulsing parameters of the oxygen gas were kept the same as those set for the single W target DC sputtered. Tungsten target current was systematically changed from $I_W = 40$ to 100 mA whereas the WO_3 self-bias potential was modified from $U_{\text{WO}_3} = 100$ to 300 V in order to play with the films microstructure, as well as W and O concentrations.

When only one W target was DC sputtered, and in order to determine the oxygen pulsing parameter, argon was first injected at $q_{\text{Ar}} = 1.2 \text{ sccm}$ (the corresponding argon pressure was $p_{\text{Ar}} = 2.8 \times 10^{-3} \text{ mbar}$). W target was DC sputtered with $I_W = 100 \text{ mA}$ and the oxygen gas was injected in the chamber. At first, oxygen flow rate was gradually injected from 0 to 2.4 sccm, and then reduced back to 0 sccm. The total sputtering pressure p_{sp} in the chamber and the W target voltage U_W were recorded (Figure 3.3).

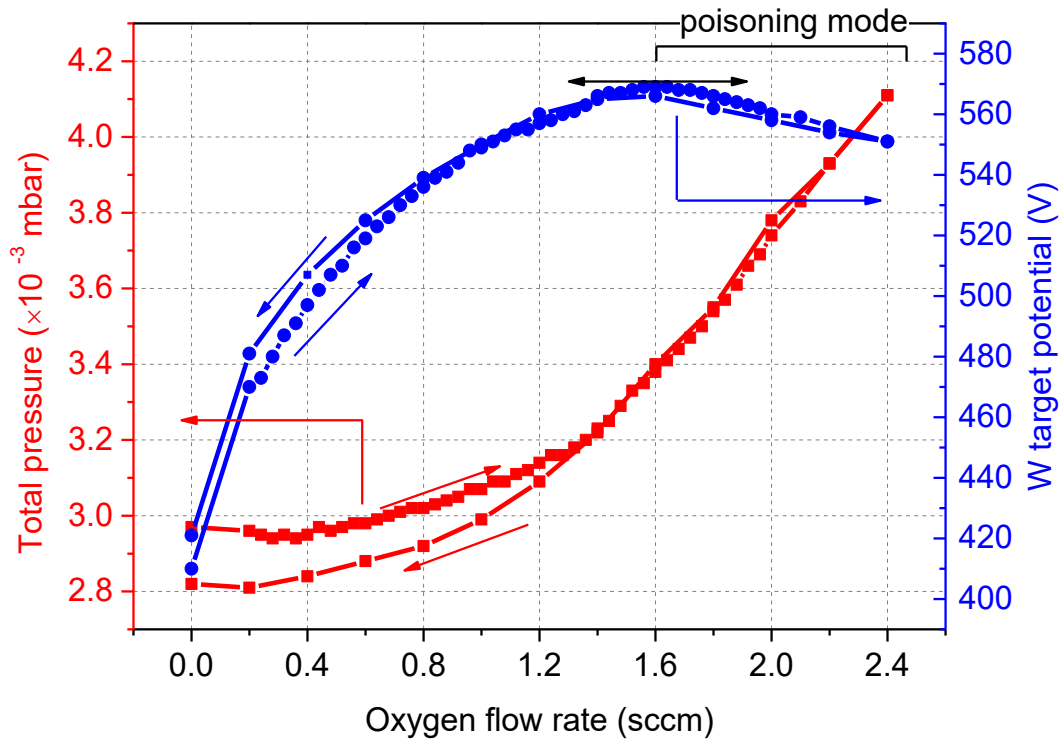


Figure 3.3: Evolution of the total sputtering pressure (■) and W target potential (●) vs. oxygen flow rate. The pumping speed $S = 10 \text{ L s}^{-1}$, argon pressure $p_{Ar} = 2.8 \times 10^{-3} \text{ mbar}$ and W target current $I_W = 100 \text{ mA}$.

Without oxygen injection, the W target voltage is more than 400 V and corresponds to a pure metallic sputtering mode. For the shortest oxygen flow rate (0.2 sccm), U_W abruptly rises up to 470 V and then gradually reaches a maximum of 570 V for $q_{O_2} = 1.6 \text{ sccm}$. A further increase of the oxygen flow rate gives rise to a slight drop of the W target voltage. In-between 1.6-2.4 sccm, we can assume that the reactive sputtering process is mainly in reactive sputtering mode (i.e. W target surface is poisoned by the oxygen gas). Similarly, the total sputtering pressure slightly increases from 3.0×10^{-3} up to 3.4×10^{-3} mbar as q_{O_2} changes from 0 to 1.6 sccm. Afterward, p_{sp} linearly increases vs. q_{O_2} , which correlates with a poisoning mode of the reactive sputtering process. Despite the low pumping speed implemented during the deposition stage ($S = 10 \text{ L s}^{-1}$), reducing the oxygen flow rate does not exhibit a hysteresis loop of the total sputtering pressure and target voltage as it can be commonly reported for other systems like Ti-O₂ [28] or Zr-O₂-N₂ [32]. Therefore, by setting an oxygen flow rate higher than 1.6 sccm, the sputtering process becomes mainly oxidized. To be sure to avalanche the process in reactive mode, $q_{O_2Max} = 2.4 \text{ sccm}$ has been chosen.

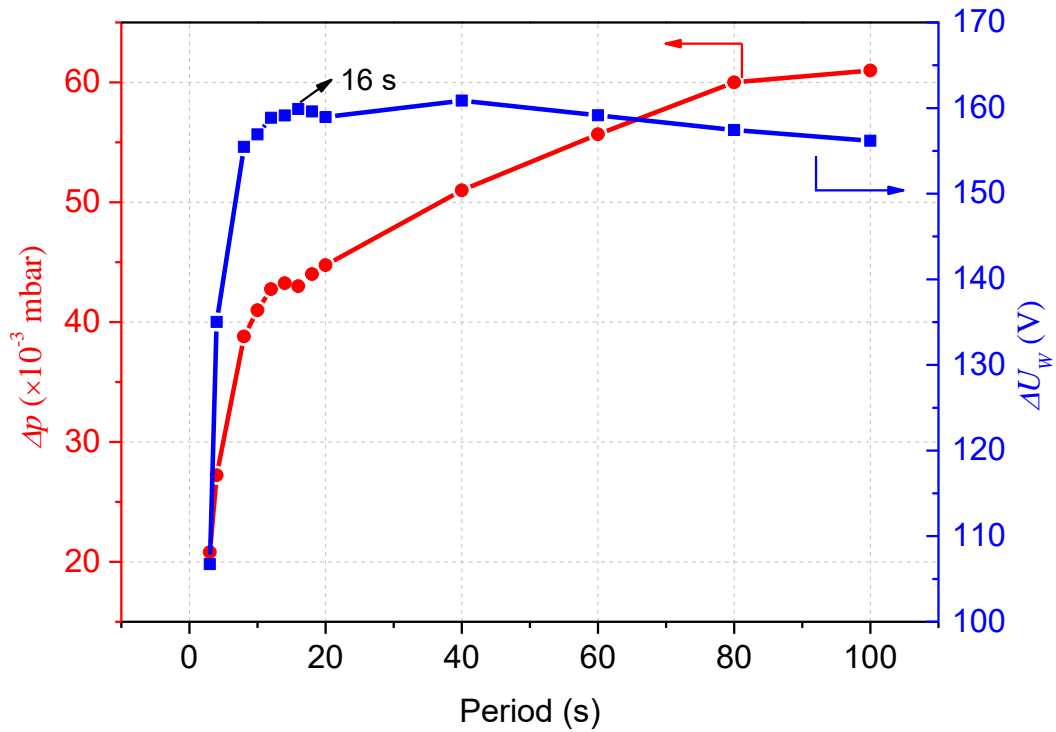


Figure 3.4: Variation of the total sputtering pressure (■) and W target potential (●) as a function of the pulsing period of the oxygen gas. Duty cycle $dc = 50\%$ of P , $q_{O2Max} = 2.4$ sccm, $q_{O2min} = 0$ sccm, Pumping speed $S = 10$ L s⁻¹, argon partial pressure $P_{Ar} = 2.8 \times 10^{-3}$ mbar and W target current $I_w = 100$ mA.

In order to choose the pulsing period P of the oxygen mass flow rate, the duty cycle defined as $dc = T_{ON}/P$ was set as 50 % of P keeping $q_{O2Max} = 2.4$ sccm during the T_{ON} time and stopping the oxygen flow rate for the rest of the period (i.e. $q_{O2min} = 0$ sccm during the T_{OFF} time). The variation of W target voltage and total sputtering pressure between T_{ON} and T_{OFF} , ΔU and Δp , respectively, were both recorded as a function of an increasing pulsing period P from 4 to 100 s (Figure 3.4).

Changing the pulsing period from 4 to 10 s produces an abrupt increase of the total sputtering pressure variations, which is even more significant for the W target voltage. For pulsing periods higher than 10 s, the target voltage variation becomes stable and the sputtering pressure still rises but to some extent. For these pulsing conditions ($P > 10$ s), the process completely alternates between the reactive and metallic sputtering modes. As a result, the pulsing period has to be long enough to be able to change the duty cycle keeping such an alternation between both modes. A pulsing period $P = 16$ s has been selected since it allows getting sputtering conditions to get fully metallic or oxidized sputtering mode during T_{OFF} and T_{ON} times, respectively, and so tuning the oxygen concentration in the films.

3.2. Characterization techniques

The substrate material was glass and (100) silicon wafer. All substrates were cut to the following dimensions 25 mm × 12.5 mm. They were ultrasonically cleaned in acetone, ethanol and deionized water for 10 min and dried in an oven (60 °C). For testing the sensing performances, W-O thin films were sputter deposited on commercial MSP 769 Heraeus sensor platforms. The sensing procedure will be more described in the next paragraph.

Morphology of W-O films was observed with a Dual Beam SEM/FIB FEI Helios 600i microscope on the fractured cross-section and on the top view. Due to the limited number of samples that fit on the substrate holder since a strict placement of the substrates directly in front of the sputtered particle flux is crucial, a first series of samples was sputtered on silicon substrates. They were used for the deposition rate calculation (obtained from the film thickness measured by profilometry, and deposition time), and SEM cross-section and top imaging. Then, taking into account the different deposition rates, the sputtering time was adjusted in order to keep an overall thickness close to 400 nm for all films used in the subsequent characterization and sensing tests. X-ray diffraction (XRD) patterns of the films were collected by D8 focus diffractometer using a cobalt source ($\text{Co } \lambda_{K\alpha} = 1.78897 \text{ \AA}$) according to a Bragg–Brentano θ - 2θ configuration. Scans were performed with a 2θ angle with a step of 0.02° per 0.2 s and a 2θ angle ranging from 20 to 80° .

Optical transmission spectra of the films deposited on glass substrate were recorded with a Lambda 900 UV-visible optical spectrometer. A mask (black piece) with a hole of 1 mm diameter was placed in the light path, to limit the observed area on the thin films. This mask allows probing a nearly constant thickness and avoid thickness gradient, which is especially substantial in GLAD films exhibiting an inclined columnar structure (intrinsic to the GLAD process). Optical transmittance spectra of thin films deposited on glass substrate were recorded in the visible range. The scanning wavelength ranged from 300 nm to 1100 nm, with 1 nm s^{-1} scanning speed.

The DC electrical resistivity of the films deposited on glass substrate was measured at room temperature or vs. temperature (from RT to 300 °C) by the four-probe method. Measurements were carried out in air using a custom-made chamber, which was covered in order to achieve a dark environment. The measurement procedure is based on the van der Pauw's method [84] (Figure 3.5). It requires four Ohmic contacts (golden tips) to be placed on the boundaries of the sample (or as close to it as possible) and as small as possible compared to the distance between them. To make a measurement, a current is applied between 2 contacts (for instance, I_{12}) and the voltage across the opposite edge (in this case, V_{34}) is measured. From these two values, a resistance can be deduced using Ohm's law.

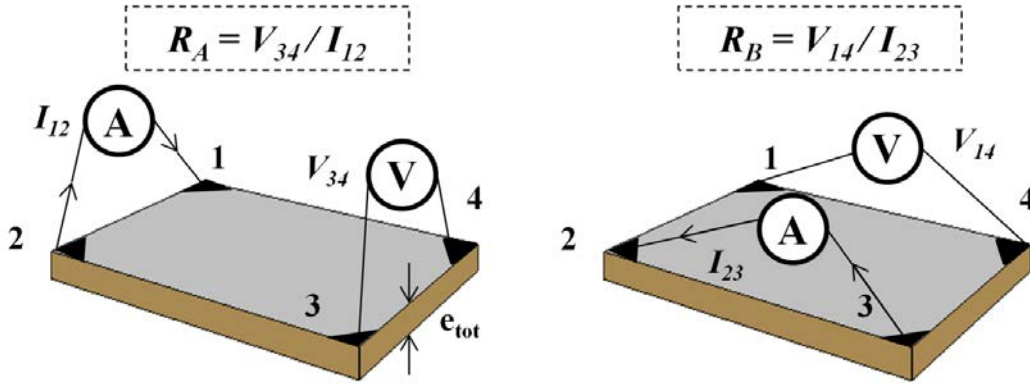


Figure 3.5: Illustration of the van der Pauw's procedure [84].

Similar measurements are applied following the NIST procedure [85] in order to get 8 resistances and finally, an average of two resistances, namely R_A and R_B , defined as:

$$\begin{cases} R_A = \frac{R_{21,34} + R_{12,43} + R_{43,12} + R_{34,21}}{4} \quad (\Omega) \\ R_B = \frac{R_{32,41} + R_{23,14} + R_{14,23} + R_{41,32}}{4} \quad (\Omega) \end{cases} \quad (3.1)$$

Knowing the film's thickness " d ", the electrical resistivity " ρ " is obtained following:

$$\rho = \frac{\pi d}{\ln 2} \left(\frac{R_A + R_B}{2} \right) F \quad (\Omega \text{ m}) \quad (3.2)$$

where F is the van der Pauw's coefficient, which depends on the $R = R_A/R_B$ ratio (or R_B/R_A since R must be > 1). The F coefficient is calculated using:

$$\frac{1}{2} e^{\frac{\ln 2}{F}} = \cosh\left(\frac{R-1}{R+1} \cdot \frac{\ln 2}{F}\right) \quad (3.3)$$

Similarly, charge carrier mobility and concentration can be determined by Hall effect by means of the same procedure as electrical resistivity measurements, but applying a magnetic field B of 0.8 Tesla perpendicular to the sample surface. At first, the magnetic field $+B$ is set, and a current is applied between 1 and 3 (I_{13}). The resulting voltage between 2 and 4 (V_{24P}) is measured. Similar measurements are performed with a current between contacts 3 and 1 (I_{31}) and a voltage between 4 and 2 (V_{42P}), and so on. V_{24P} , V_{42P} , V_{13P} , V_{31P} associated to I_{13} , I_{31} , I_{24} , I_{42} are obtained, respectively. Thus, the magnetic field is reversed, i.e. $-B$, and the same routine is used leading to V_{24N} , V_{42N} , V_{13N} , V_{31N} associated to I_{13} , I_{31} , I_{24} , I_{42} , respectively.

One can calculate V_C , V_D , V_E and V_F following:

$$V_C = V_{24P} - V_{24N}; V_D = V_{42P} - V_{42N}; V_E = V_{13P} - V_{13N}; V_F = V_{31P} - V_{31N}$$

The sample type is then determined from the polarity of the voltage sum $\Sigma V = V_C + V_D + V_E + V_F$. If ΣV is positive (negative), the film is p-type (n-type), I = average current (A), q = elementary charge (1.6×10^{-19} A s). The carrier concentration is then given by:

$$\begin{aligned} [p] &= \frac{8 \times 10^{-6} IB}{qd\Sigma V} \quad (cm^{-3}) \text{ for p - type} \\ [n] &= \left| \frac{8 \times 10^{-6} IB}{qd\Sigma V} \right| \quad (cm^{-3}) \text{ for n - type} \end{aligned} \quad (3.4)$$

The carrier mobility is obtained from:

$$\begin{aligned} \mu_p &= \frac{d}{q[p]\rho} \quad (m^2 V^{-1} s^{-1}) \text{ for the hole mobility for p - type} \\ \mu_n &= \frac{d}{q[n]\rho} \quad (m^2 V^{-1} s^{-1}) \text{ for the electron mobility for n - type} \end{aligned} \quad (3.5)$$

3.3. Sensor setups and conditions

W-O thin films were sputter deposited on commercial MSP 769 Heraeus sensor platforms (Figure 3.6). Such a device is made of interdigitated combs and allows a simultaneous heating, temperature and thin

film electrical resistance measurements *vs.* time during the gas testing. The MSP 769 module combines a heater layer of Pt 25 ($25.0 \pm 2.5 \Omega$ at 0°C with a characteristic curve according to DIN EN 60 751), and a temperature sensor thin film of Pt 1000 (1000Ω at 0°C , measuring values and characteristic curve according to DIN EN 60 751) on a ceramic substrate covered with an insulating glass layer. Interdigitated gold electrodes are deposited on the insulating glass layer, onto which a sensing layer can be deposited by thin film technology. Before testing, the sensor was aged under synthetic dry air flow (200 mL min^{-1} , 5% RH) at 300°C for 12 hours to test the stabilization of sensors resistance.

Dodecane was thermalized (vaporized) by means of a water bath at 35°C and synthetic dry air carrying dodecane through the tubes, where they were warmed by electric resistance heating tape, which kept the tubes at 40°C , in order to avoid the dodecane condensation in the tubes. After passing through the reactor, the exhaust went through the humidity sensor.

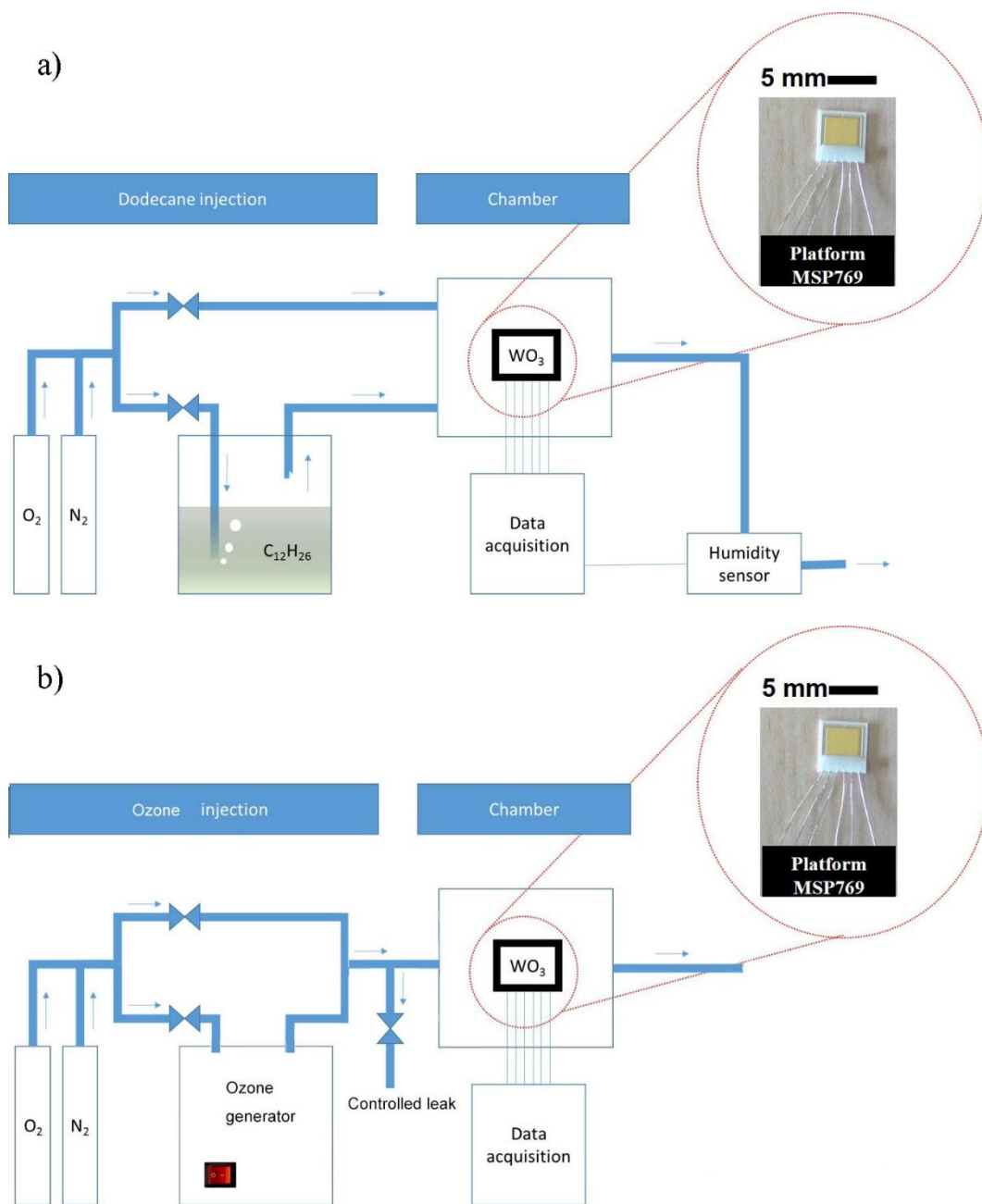


Figure 3.6 Schematic view of systems used to test W-O films exposed to a) dodecane vapor and b) ozone gas.

The ozone was generated by a commercial gas generator (O_3 1000[®]), by means of a UV radiation of air flow, to transform the oxygen into ozone, precisely and constantly. The dilution was controlled by a leak. A constant air flow rate (200 mL min^{-1}) passed through the gas generator. Then a second route could be varied from 0 to 800 mL min^{-1} . The two routes were mixed before the controlled leak. Then the leak was modified to make sure that only 200 mL min^{-1} diluted ozone could enter the reactor. Two dilution benches were used in order to expose the sensor layer under various concentrations of ozone (initial concentration equal to 220 ppb) or dodecane (initial concentration equal to 300 ppm)

balanced in synthetic dry air flow (Figure 3.6) [86]. For each experiment, the sensor was exposed to a constant gas flow rate of about 200 mL min^{-1} . The electrical resistance change of the sensing film was measured as a function of time. In this study, the sensing properties of the films were studied at different working temperatures from room temperature up to $500 \text{ }^\circ\text{C}$ and under different concentrations of ozone or dodecane in synthetic dry air. These experiments allowed evaluating both the optimum operating temperature and then the limit of detection of various efficient W-O structures. Figure 3.7 shows an example of the resistance of WO_x film sensor vs. time under test with ozone and dodecane.

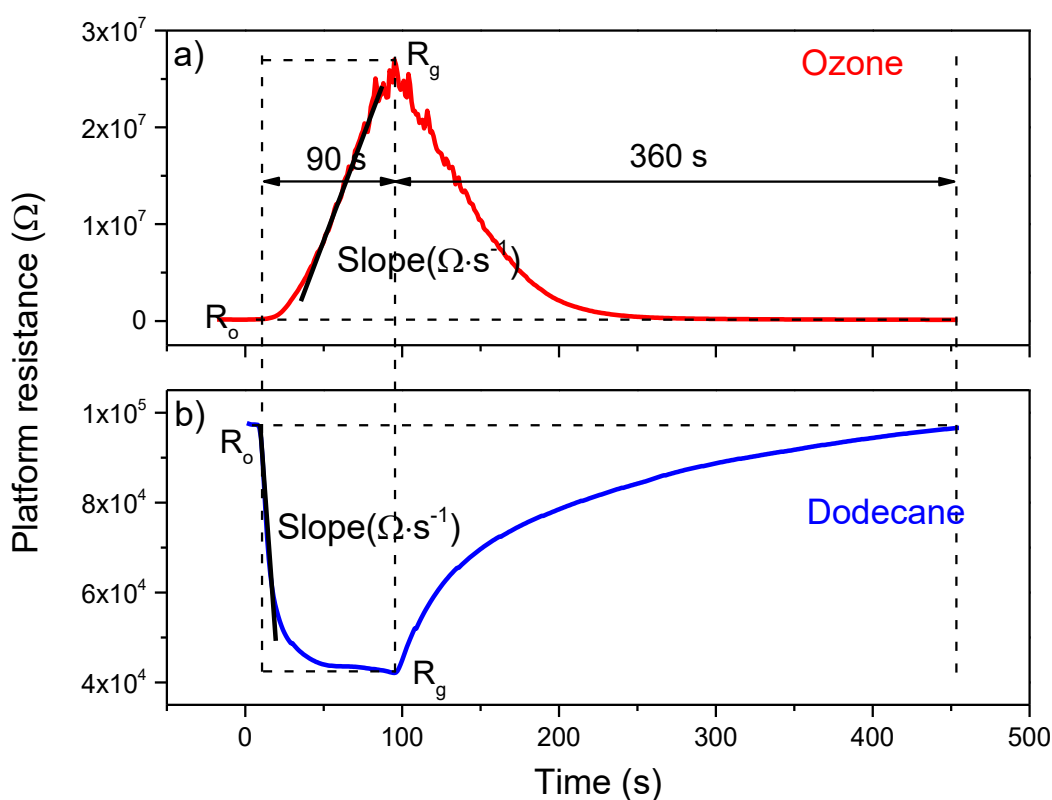


Figure 3.7 Typical WO_x gas sensor response of a) ozone and b) dodecane, under concentration of $[\text{O}_3]$ at 500 ppb and $[\text{C}_{12}\text{H}_{26}]$ at 300 ppm for 90 s (air exposure time is 360 s).

The gas response of the sensor is defined as $S = |R_g - R_0| / R_0 \times 100 \%$, where R_g is the resistance (Ω) in the air mixed with ozone or dodecane and R_0 is the resistance (Ω) under synthetic dry air. Since WO_x film is an n-type sensor, the gas response exhibits a peak when the sensor is under ozone and a valley when it is exposed under dodecane. The response slope was calculated from the linear part of the response curve. The exposing time and air exposure time were fixed at 90 and 360 s, respectively.

4. Chapter 3: WO_x films with one W target

This chapter aims at preparing W-O thin films with a suitable resistivity range and porosity microstructure. RGPP is an attractive method, which can gradually and precisely produce tunable compounds by adjusting deposition parameters, particularly duty cycle dc , so as to reach a regular and well-controlled evolution of the growth rate, composition, optical behaviors and electronic transport properties. To modify the films' microstructure, GLAD is applied for fabricating various architectures, such as columnar, zigzag and spiral W-O thin films. Electrical, optical properties, microstructure and morphology are finally investigated.

4.1. WO_x films by RGPP

WO_x films were prepared by RGPP, from pure metallic W to over-stoichiometric WO₃ thin films. By modifying the duty cycle, thin films exhibit various electrical and optical properties. We focus on some optimized compositions to apply W-O thin film as gas sensors.

4.1.1 Structure, morphology and composition

SEM observations of the cross-section of the films show various morphologies as a function of the duty cycle (Figure 4.1). Without oxygen injection, a typical columnar microstructure is clearly viewed (Figure 4.1a). Taking into account qualitative structure zone models based-on Thornton's diagram [87] or more recently improvements suggested by Anders [88], densely packed fibrous grains are expected for DC sputtering of pure tungsten films. It may be suggested that W films tend to feature as a zone T microstructure rather than zone 1 since tungsten is a heavy atom, for which the reflection probability of Ar neutral is strongly favored [89]. Thus, the contribution of reflected neutrals to the total deposited energy certainly increases the displacement and heating effects on the growing film.

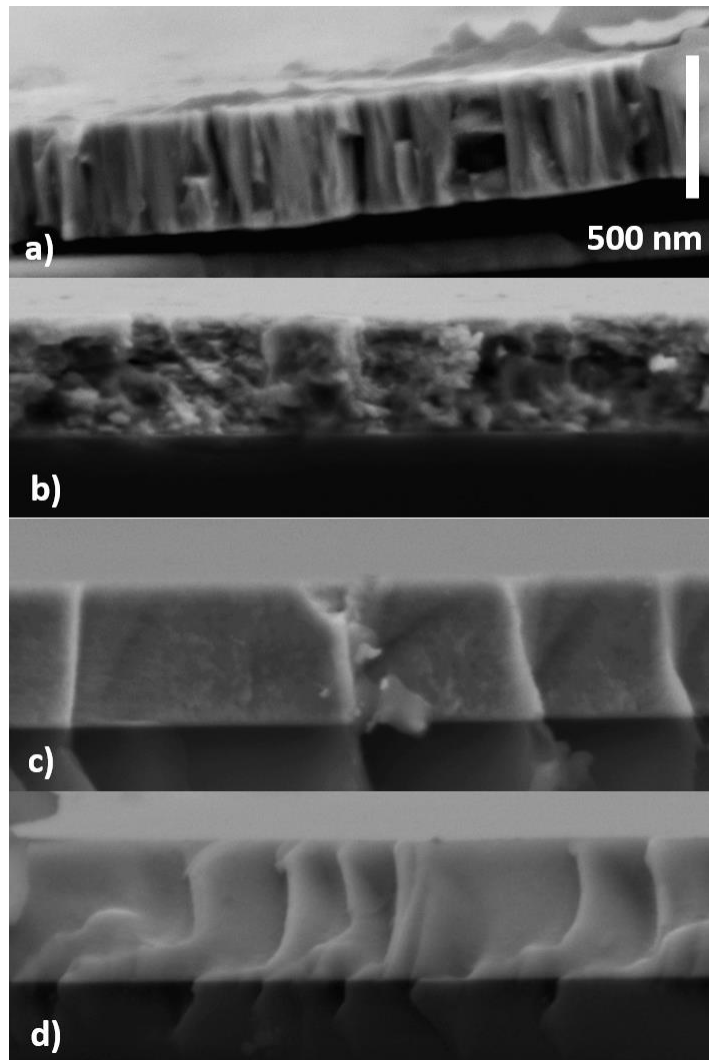


Figure 4.1 SEM cross-sections of tungsten and W-O thin films deposited on silicon substrate with various duty cycles: (a) $dc = 0\%$, (b) $dc = 20\%$, (c) $dc = 40\%$, (d) $dc = 100\%$ of P .

When oxygen is pulsed and for the lowest duty cycles (up to $dc = 20\%$ of P), the columnar structure vanishes as shown in Figure 4.1b. A granular-like aspect of the cross-section is observed, which gives rise to a random fracture of the films. The oxygen addition during the sputtering process (reactive mode) combined to the periodic injections certainly disturb the W-O growth mechanism as well as the long-range order (to see XRD results later).

From $dc = 40\%$ of P and for a further increase of the duty cycle, cross-section observations by SEM show a featureless morphology (Figure 4.1c and d). W-O films prepared with duty cycles higher than 40% of P contain more than 60 at. % of oxygen from compositional analyses (Figure 4.2). One can expect a ceramic-like behavior of these films as illustrated from the fracture of silicon wafer, which is

extended through the coatings thickness. In addition, the cross-section of W-O films prepared with the highest duty cycles exhibits representative fracture surfaces of brittle materials, which corroborate their ceramic-like characteristics.

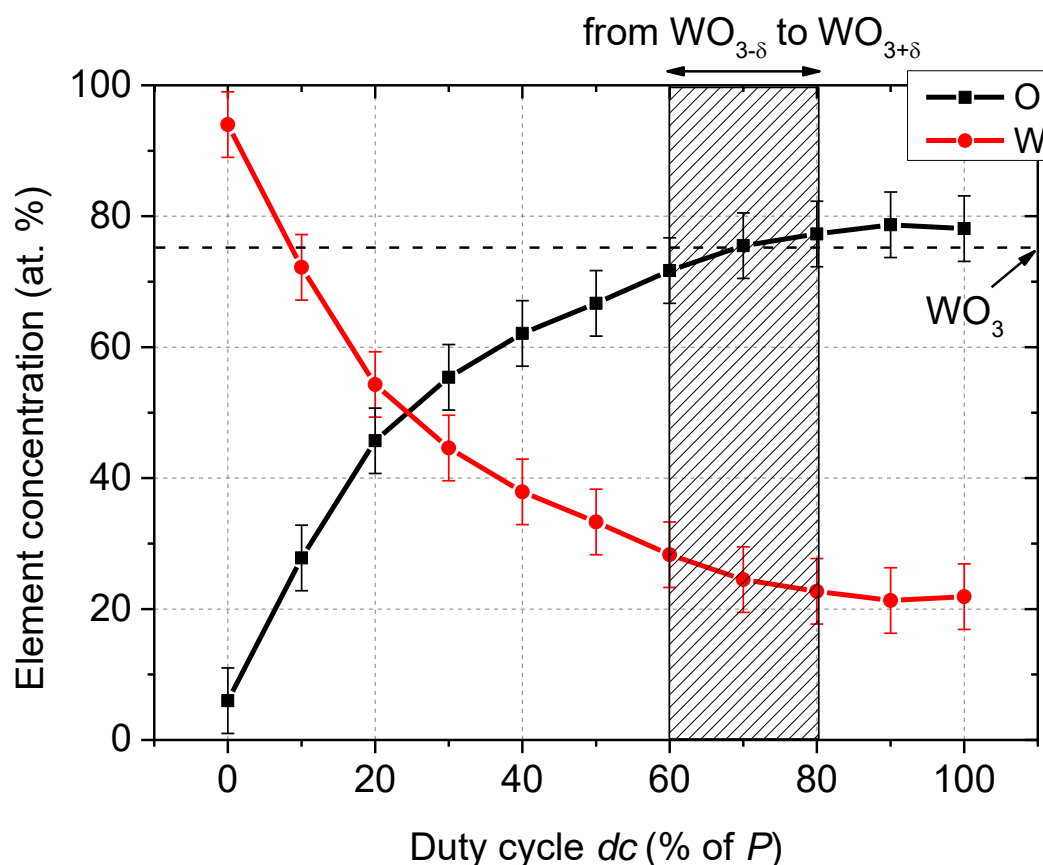


Figure 4.2 Oxygen and tungsten atomic concentrations by EDS in W-O thin films as a function of the duty cycle dc . A gradual evolution is obtained by means of a systematic increase of dc . For duty cycles in-between 60 - 80 % of P , sub-stoichiometric $WO_{3-\delta}$ to oxygen-rich $WO_{3+\delta}$ compounds are produced.

Most of the metallic targets sputtered in argon + oxygen atmosphere typically exhibits a sudden drop of the deposition rate as a function of the reactive gas flow rate [90]. Due to a poisoning effect of the target surface and since the sputtering yield of an oxide compound is much less than that of the metal, oxide thin films are normally deposited with a maximum rate of a few percent of the pure metal rate [91]. With the Reactive Gas Pulsing Process, a gradual transition of the rate is rather measured when the duty cycle is incrementally increased [92]. Again, the deposition rate of W-O films smoothly varies with the duty cycle, as shown in Figure 4.3.

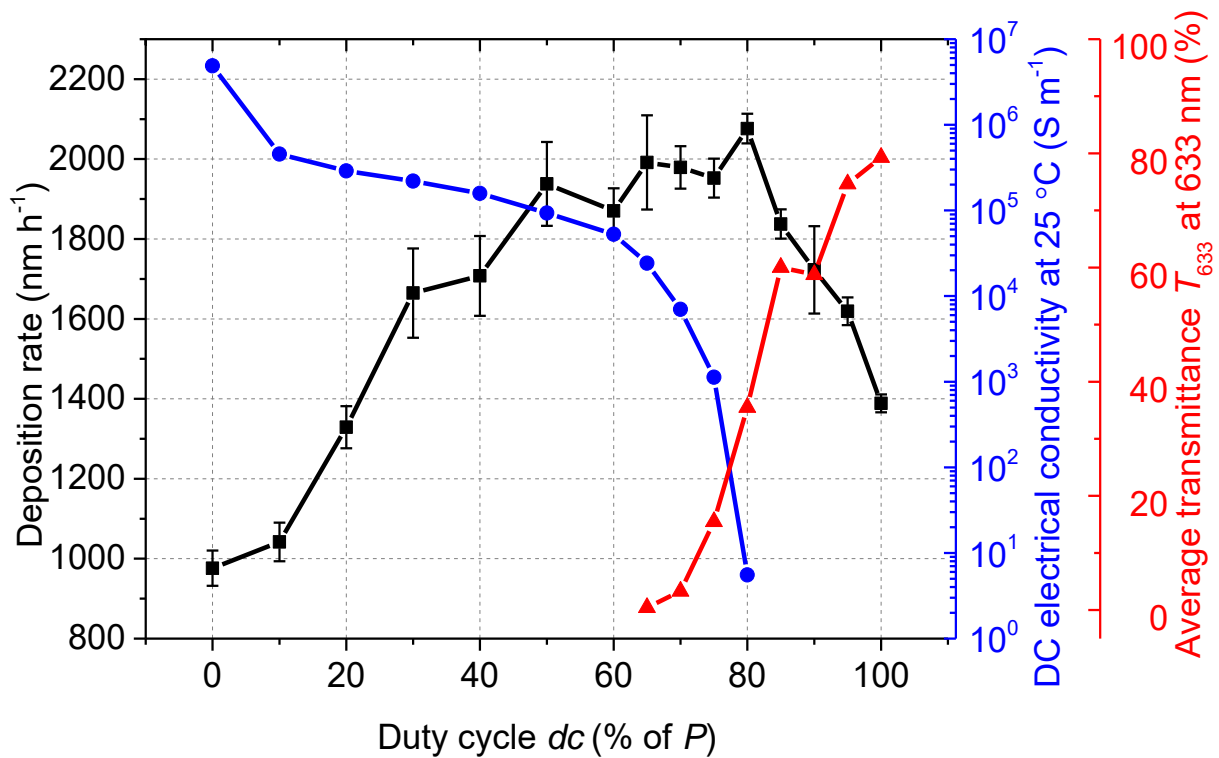


Figure 4.3 Deposition rate (■), DC electrical conductivity at room temperature $\sigma_{25^\circ\text{C}}$ (●) and optical transmittance T_{633} at 633 nm (▲) of W-O thin films as a function of the duty cycle dc .

Firstly, deposition rate increases as duty cycle changes from 0 to 70 % of P , then reaches a maximum value higher than 2000 nm h^{-1} , which is twice the pure tungsten rate, for dc around 70 % of P . When the oxygen flow rate tends to be constantly injected ($dc = 100$ % of P), deposition rate drops down to 1400 nm h^{-1} , which is again significantly higher than the pure tungsten rate. This bell-shaped and enhancement of the deposition rate are mainly connected to the poisoning effect of the target surface, an increase of the oxygen concentration in the deposited films, and the density of deposited oxide compounds. A balance occurs between the sputtering yield of W-O compounds formed on the metallic target surface and its oxidation by the reactive gas. When oxygen is injected at the beginning of the T_{ON} time (Figure 4.4), the W target surface starts oxidizing and leads to an increase of the W target voltage, as shown in Figure 4.4b, curve 1-2. Afterwards, the process avalanches in the oxidized sputtering mode (Figure 4.4 b, curve 2-3), but with a lower sputtering yield [93]. During the remaining T_{ON} time, W target voltage tends to be stable and reaches a plateau.

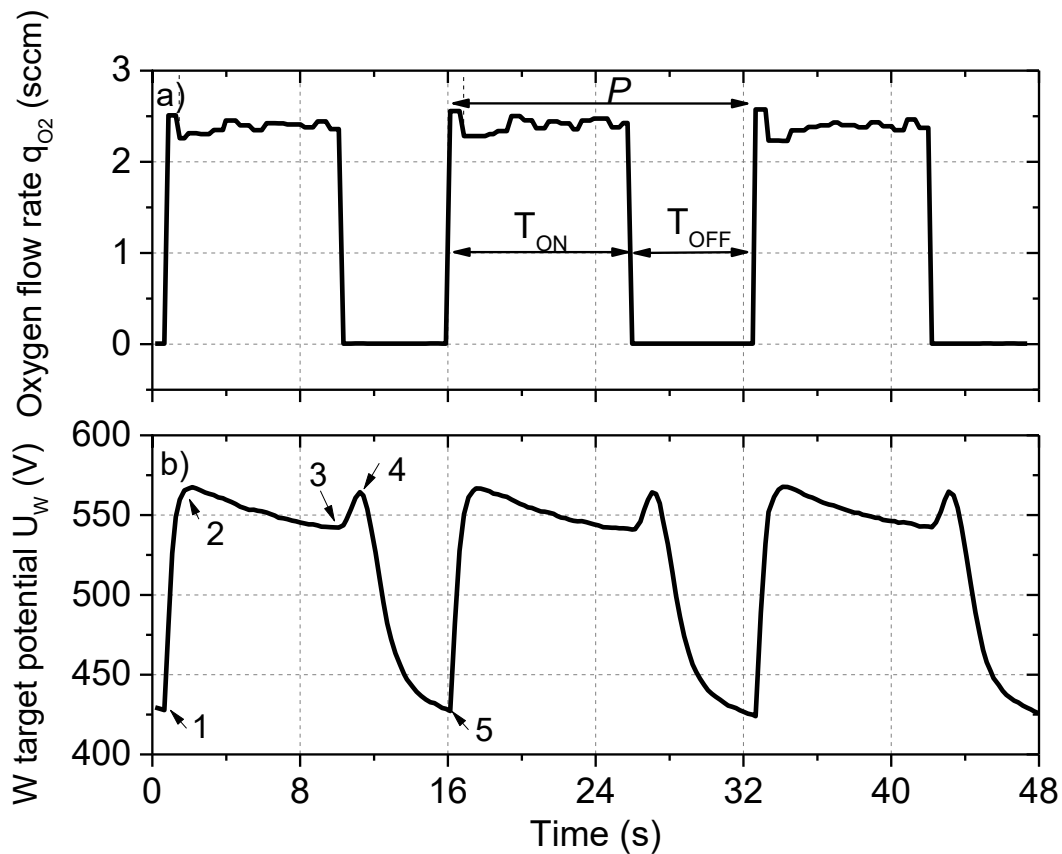


Figure 4.4 An example of a) the pulsed oxygen flow rate vs. time, and b) the W target potential U_W vs. time recorded for $dc = 60\%$ of P .

When oxygen supply is switched off (T_{OFF} time starts), the process comes back to the metallic sputtering mode and less oxygen is incorporated in the film (Figure 4.4 b, curve 3-4), and then target surface is renewed and leaves the oxidized sputtering mode. The W target potential comes back to the beginning, as shown in Figure 4.4b, curve 4-5. During one pulsing period P , these alternations between oxidized and metallic sputtering modes increase the average of the target voltage, the amount of oxygen in the films, and since the density of W-O is substantially lower than that of pure tungsten, the resulting deposition rate is enhanced.

With a further increase of the duty cycle (i.e. $dc > 60\%$ of P), the T_{OFF} time is too short to restore the process in the metallic mode (Figure 4.5). Deposition rate drops, oxygen concentration becomes stable (Figure 4.2) and the process tends to behave as the conventional reactive sputtering (constant supply of oxygen).

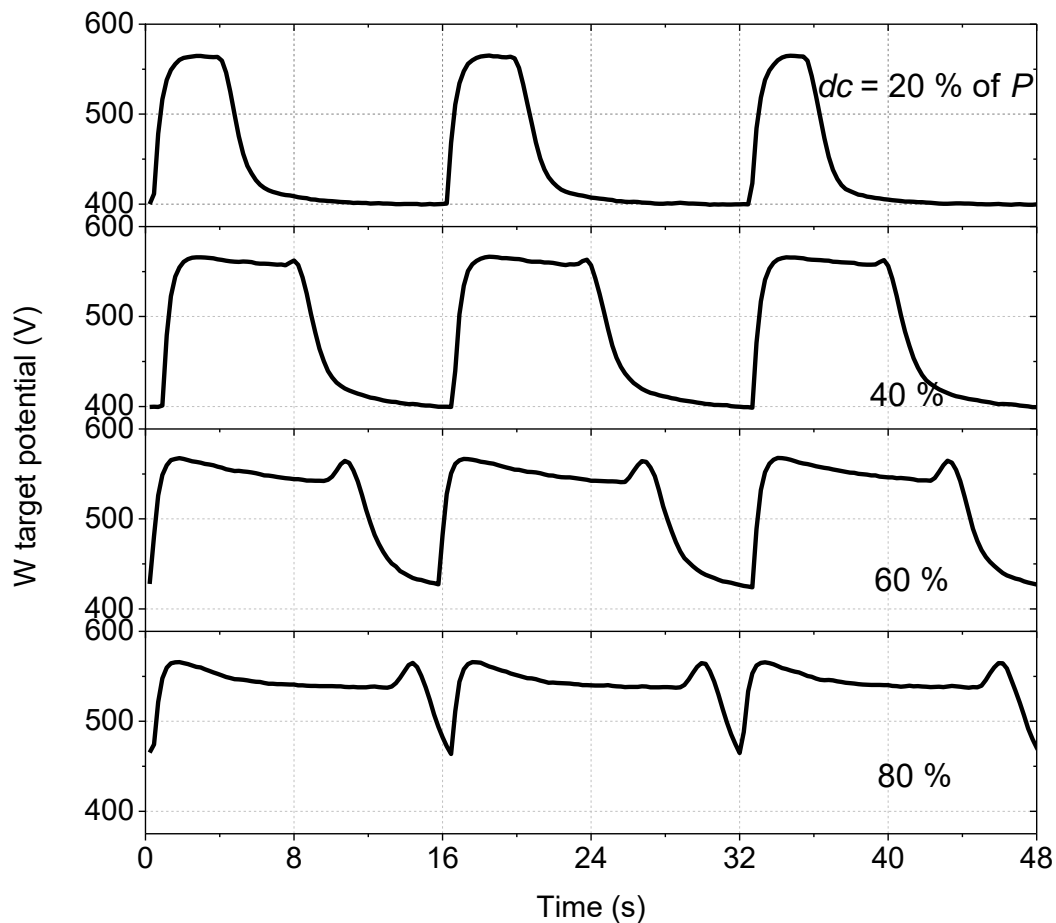


Figure 4.5 W target voltage vs. time for various duty cycles.

About the evolution of tungsten and oxygen contents in WO_x films as a function of the duty cycle (Figure 4.2), no abrupt transition of the elemental concentrations is observed as commonly reported for a critical oxygen flow rate when most of the binary oxides are prepared by reactive sputtering [94]. A reverse and continuous change of O and W concentrations is rather obtained as dc increases. It is mainly assigned to the alternation of the reactive process between the metallic and oxidized sputtering modes. During the T_{ON} time, the oxygen flow rate rapidly reaches 2.4 sccm, which avalanches the process in the compound sputtering mode. During the T_{OFF} time, the oxygen mass flow rate is completely stopped, and the process can be restored to the metallic mode. The full alternation between each mode obviously depends on the T_{ON} and T_{OFF} times (both must be long enough). As a result, the duty cycle of RGPP is a key parameter to progressively tune the chemical composition of W-O thin films. By conventional reactive sputtering (i.e. a constant oxygen flow rate during deposition), the oxygen concentration in the films rises more

abruptly as a function of the O₂ content in the sputter gas mixture [95], which may restrain the operating conditions required to adjust the metalloid concentration. It is also worth noting that duty cycles lower than 60 % of the pulsing period P produce the most significant variation of the films composition. For $dc > 60$ % of P , oxygen and tungsten concentrations tend to value corresponding to the stoichiometric WO₃ material. The most interesting range of duty cycles is in-between 60 - 80 % of P since films increasingly evolve from O-deficient to O-rich WO₃ compound, for which the results were measured with the EDS.

X-ray diffraction patterns of WO_x thin films show that the crystalline structure is mainly influenced by the shortest duty cycles (Figure 4.6). Without oxygen introduction ($dc = 0$ % of P), a (210) strong preferential orientation of the *bcc* W phase (pdf # 04-0806) is clearly recorded at $2\theta = 47.20^\circ$. In addition, a weak but significant diffracted signal can also be noticed at $2\theta = 42.22^\circ$, which is assigned to (504) planes of the sub-stoichiometric WO_{2.83} phase (pdf #36-0103) and at $2\theta = 38.69^\circ$, which correspond to (111) planes of the WO₃ phase. This is due to 3 min of deposition with $dc = 100$ % of P in order to produce an interface between the film and the substrate. This allows adhesion of tungsten thin film on glass and no delamination. When oxygen gas is pulsed with $dc = 20$ % of P , poorly crystallized W-O films are produced with low and broad peaks assigned to *bcc* W, WO_{2.83} and W₁₈O₄₉ (pdf # 05-0392) phases. By increasing the duty cycle, a strong peak at $2\theta = 38.69^\circ$, which corresponds to (111) planes of the WO₃ phase film occurs and peaks associated to the silicon substrate are only recorded for a constant supply of the oxygen gas ($dc = 100$ % of P).

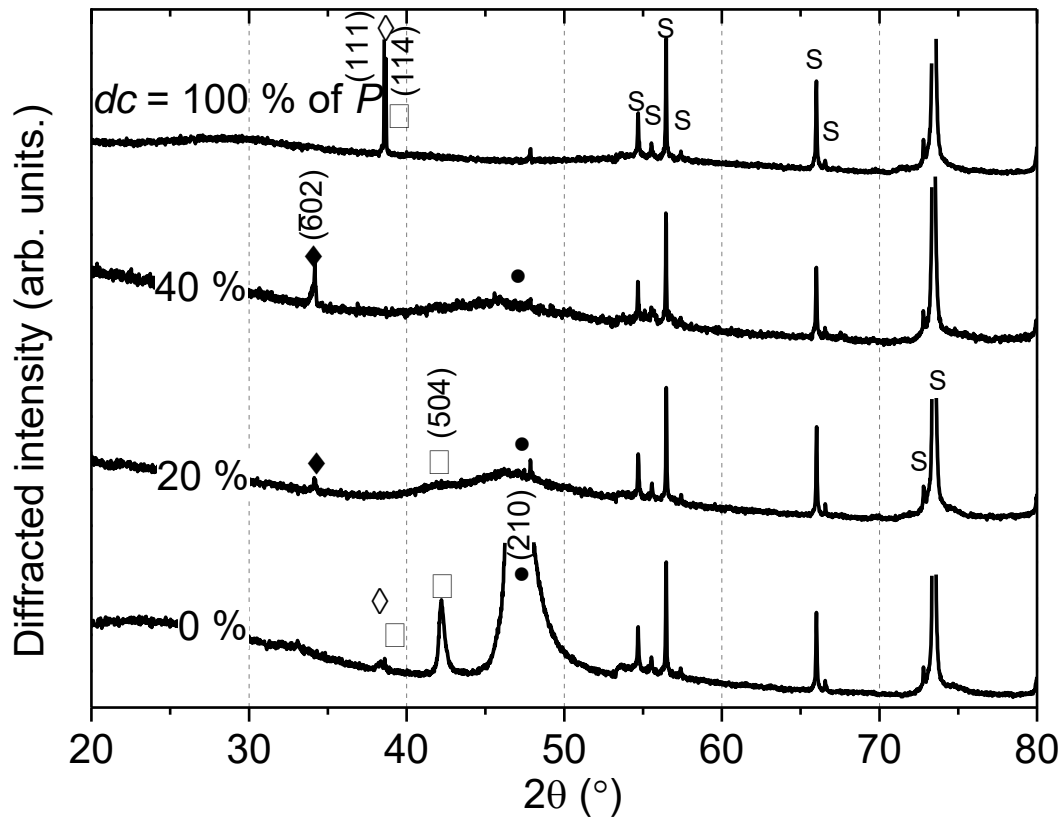


Figure 4.6 X-ray diffraction patterns of tungsten and W-O thin films deposited on silicon substrate with various duty cycles: $dc = 0, 20, 40$ and 100 % of P . S = silicon substrate; ● = W (pdf # 04-0806); ◆ = $W_{18}O_{49}$ (pdf # 05-0392); □ = $WO_{2.83}$ (pdf #36-0103); ◇ = WO_3 (pdf #05-0388).

Our results agree with that of Parreira *et al.* [33], who previously reported the growth of an amorphous phase in W-O films sputter deposited by the Reactive Gas Pulsing Process. Due to the periodic injection of the reactive gas, oxygen does not solely produce a compound formation on the target surface, but it also disturbs the growth of crystalline phases in the film. It is also worth noting that these amorphous films well correlate with the brittle microstructure previously evidenced from the cross-section viewed by SEM (Figure 4.1b and c).

4.1.2 Optical and electrical properties

The average optical transmittance at 633 nm (representative of the transparency of the material) of W-O films deposited on glass is also influenced by the duty cycle, particularly for $dc > 70$ % of P . Films are completely absorbent for the lowest duty cycles and a transition zone is achieved in the range $70 < dc < 85$ % of P , as previously shown in Figure 4.3. Films become transparent and typical interference fringes are produced in the visible region spectrum for duty cycles higher than 85 % of P , as shown in Figure

4.7. These results correlate with the evolution of W and O concentrations vs. duty cycle (Figure 4.2). Semi-transparent W-O films are obtained in this transition zone and correspond to the change from sub- to over-stoichiometric WO_3 compounds.

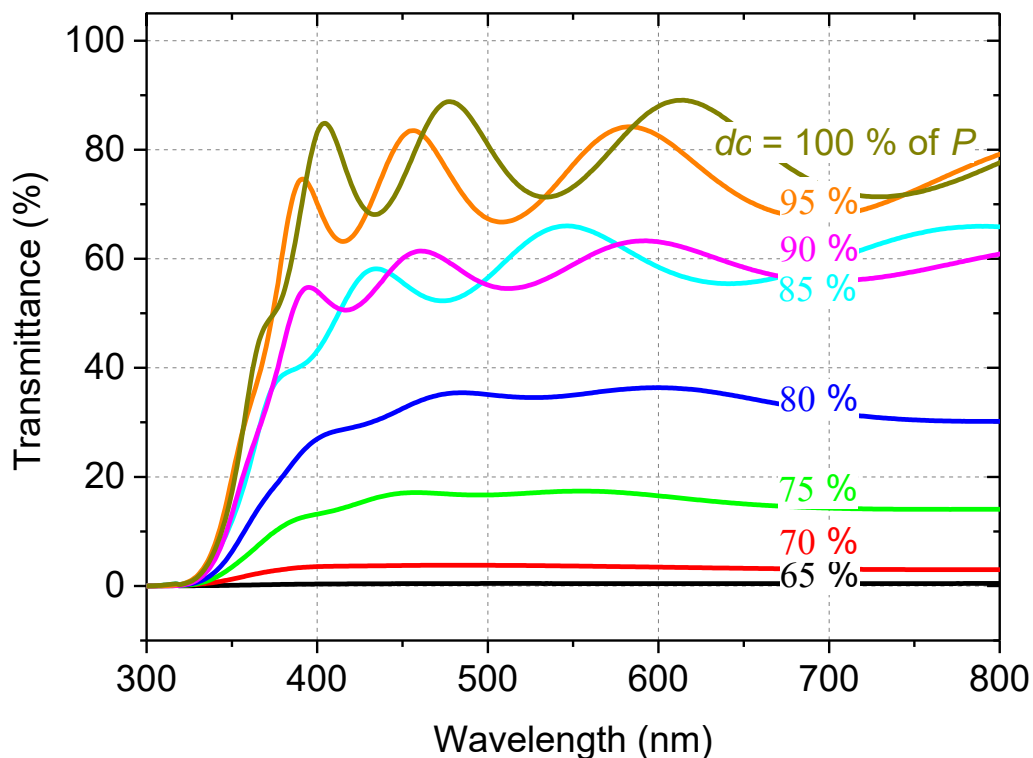


Figure 4.7 Optical transmittance spectra in the visible region of W-O thin films deposited on glass substrate for duty cycles higher than 65 % of P.

Electrical conductivity measured at room temperature also depends on duty cycle (Figure 4.3). Without oxygen introduction, the conductivity of tungsten film is $\sigma_{25^\circ C} = 4.88 \times 10^6 \text{ S m}^{-1}$, which is lower than the bulk value ($\sigma_{25^\circ C}$ of W bulk is higher than 10^7 S m^{-1}) as expected in polycrystalline thin films. For the shortest duty cycle (10 % of P), conductivity reduces by more than an order of magnitude due to a significant oxygen incorporation in the film (28 at. % from Figure 4.2). As duty cycle rises from 10 to 60 % of P , the films become continuously and slightly more resistive, which is mainly assigned to their oxygen-enrichment. The transition zone corresponding to the absorbent-to-transparent evolution previously reported from optical transmittance well correlates with the abrupt drop of electrical conductivity. Semi-transparent W-O films produced with $dc = 80\%$ of P reach the lowest conductivity with $\sigma_{25^\circ C} = 5.53 \text{ S m}^{-1}$. Films prepared with higher duty cycles are too much resistive to be measured

with our four-probe system. Such a resistivity jump is again directly related to the oxygen concentration in the films since compositional analyses clearly demonstrated a regular evolution from O-deficient to O-rich WO_3 compound in this range of duty cycles (Figure 4.2).

Electrical resistivity of the films vs. temperature was also measured from room temperature to 300 °C. Figure 4.8 shows that the electrical resistivity vs. temperature is largely affected by the duty cycle. Films exhibit a metal-like behavior at low duty cycles. It turns to semiconductor and finally insulator at higher duty cycles. When the duty cycle is higher than 80 % of P , the samples are again too much resistive to be measured.

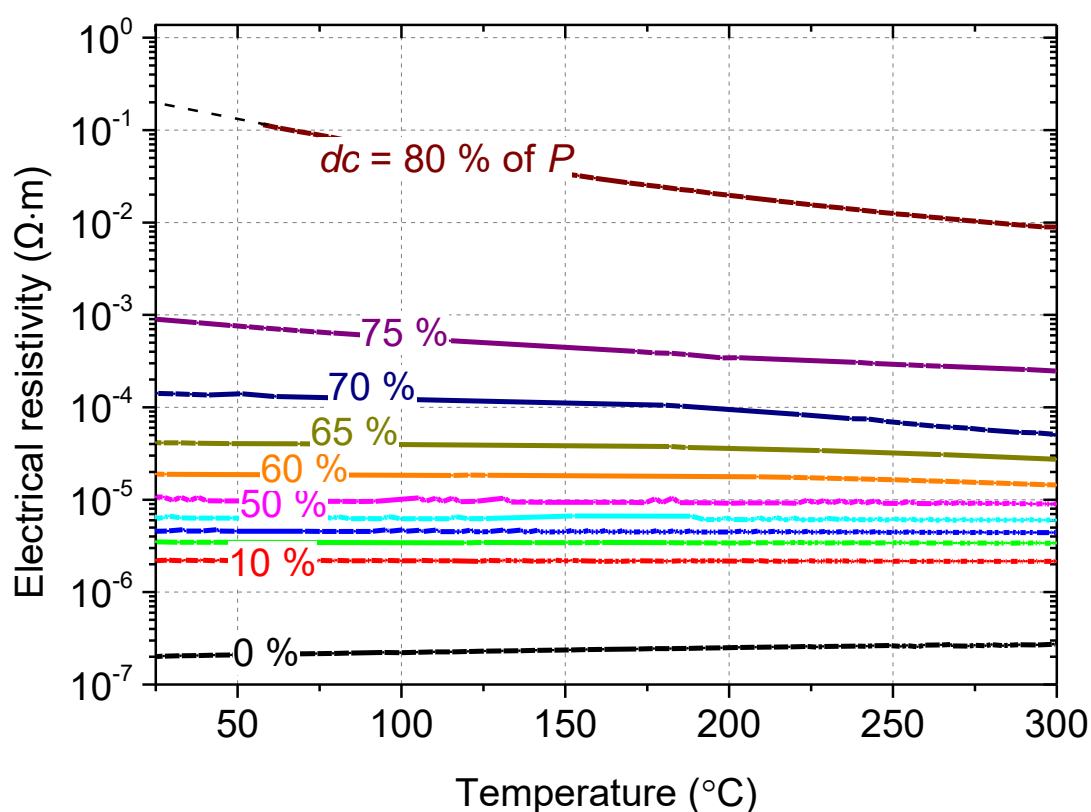


Figure 4.8 Electrical resistivity vs. temperature of W-O films prepared with different duty cycles.

Without pulsing the oxygen gas, a typical metallic-like behavior is observed, i.e. a slight increase of the electrical conductivity as the temperature rises. The temperature coefficient of resistance calculated at room temperature (RT) is $\text{TCR}_{\text{RT}} = 3.7 \times 10^{-3} \text{ K}^{-1}$ (Table 4.1). It is lower than that of the W bulk value (TCR_{RT} of bulk W is $4.4 \times 10^{-3} \text{ K}^{-1}$ [96]), which is commonly reported for thin films and mainly assigned to the scattering of electrons at grain boundaries [97]. When oxygen is pulsed and up to $dc = 30\%$ of P ,

conductivity remains in the order of 10^5 S m^{-1} and TCR_{RT} reduces to $1.6 \times 10^{-3} \text{ K}^{-1}$. The metallic-like character of the films is kept in spite of an increasing oxygen concentration in the films (55 at. % from Figure 4.2), but the conductivity tends to exhibit an invariant temperature dependence. Increasing further the duty cycle leads to negative TCRs with $-1.1 \times 10^{-2} \text{ K}^{-1}$ for $dc = 60 \%$ of P (Table 4.1).

Table 4.1 Oxygen-to-tungsten atomic concentrations ratio $[O]/[W]$, electrical conductivity at room temperature $\sigma_{25^\circ\text{C}}$, temperature coefficient of resistance at room temperature TCR_{RT} and activation energy E_a of W-O thin films prepared with various duty cycles.

Duty cycle dc (% of P)	0	10	20	30	40	50	60	65	70	75	80
$[O]/[W]$ ratio	0.06	0.38	0.84	1.24	1.63	2.00	2.53	-	3.08	-	3.40
$\sigma_{25^\circ\text{C}}$ ($\text{S}\cdot\text{m}^{-1}$)	4.9×10^6	4.5×10^5	2.9×10^5	2.2×10^5	1.6×10^5	9.3×10^4	5.3×10^4	2.4×10^4	7.0×10^3	1.1×10^3	5.5
TCR_{RT} (K^{-1})	3.7×10^{-3}	1.9×10^{-3}	1.5×10^{-3}	1.6×10^{-3}	-4×10^{-3}	-7×10^{-3}	-1.1×10^{-2}	-	-	-	-
Activation energy E_a (meV)	-	-	-	-	-	-	-	5	14	54	145

This shift from positive to negative TCR values has ever been reported for titanium oxide thin films similarly prepared by the Reactive Gas Pulsing Process [98]. Taking into account that W-O films become amorphous for duty cycles higher than 40% of P , the change of sign of TCR cannot be assigned to the number of grain boundaries per electron mean free path as suggested for crystallized metallic materials [97]. In our W-O films, this change from positive to negative values is directly connected to the growing amount of oxygen in the films. From Goldfard *et al.* investigations [99], conductivity and TCR of W-O films are related to the O $2p$ -band relative intensity in the valence band spectral region. The O $2p$ -band grows with oxygen concentration, at the expense of the W d -band. As a result, the decrease of conductivity and TCR vs. duty cycle is due to the reverse evolution of the O $2p$ and d -bands contribution to the intensity of the valence band region. A more oxygen concentration causes depletion of the d -band charge carriers in favor of the O $2p$ valence band (carrier concentration decreases).

When duty cycle varies from 60 to 65 % of P , there is a change from a low resistivity behavior (metallic-like) of W-O exhibiting a negative TCR to a semi-conducting-like behavior observed for oxygen deficient $\text{WO}_{3-\varepsilon}$ compound. A negative slope of $\text{Ln}(\sigma) = f(1000/T)$ is obtained for duty cycles higher

than 65 % of P , which is connected to a thermally induced conductivity mechanism. The linear behavior in the Arrhenius plot leads to an activation energy E_a ranging from a few meV up to 145 meV (Table 4.1) for the highest resistive films measurable with our four-probe set-up ($dc = 80\%$ of P).

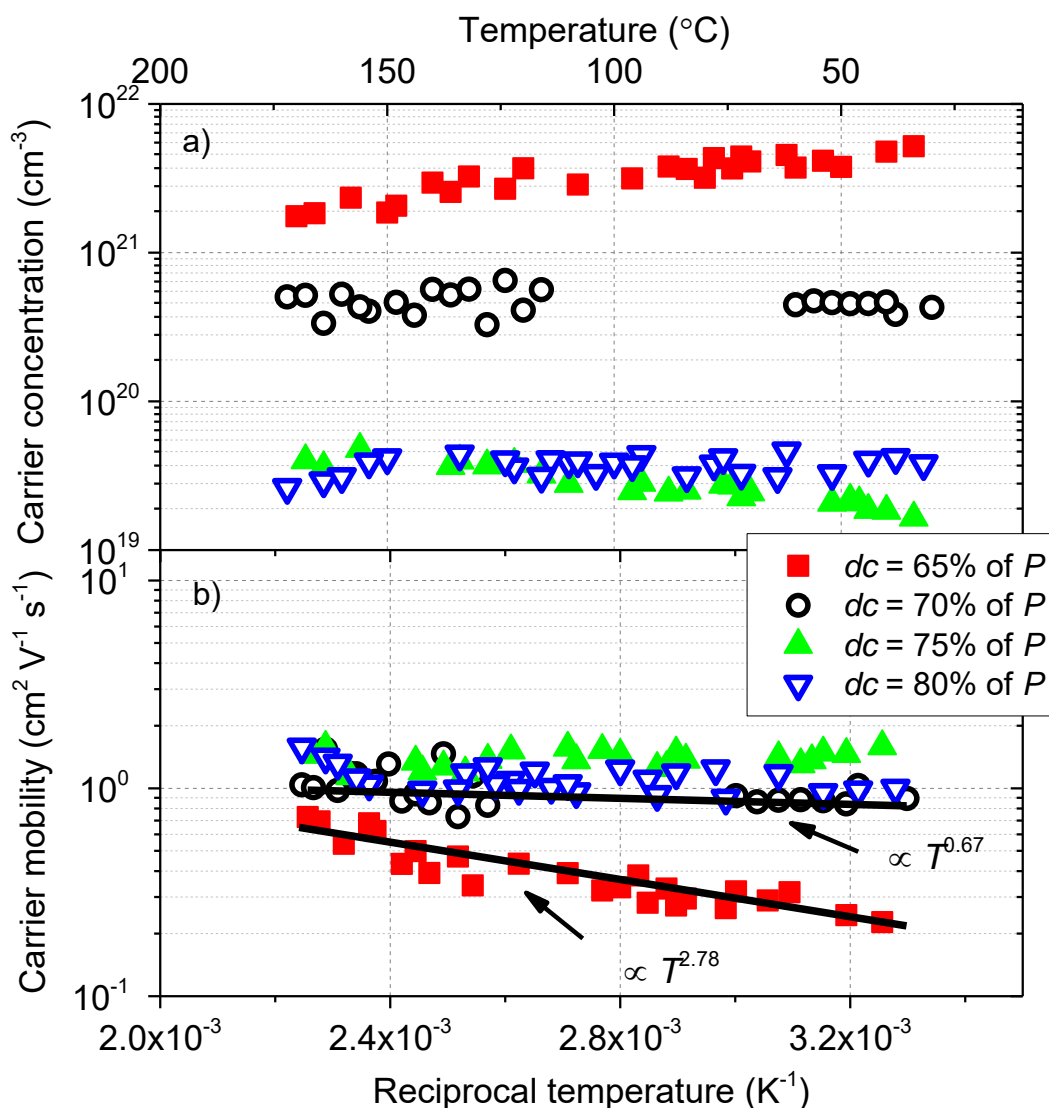


Figure 4.9 (a) Carrier concentration and (b) Hall mobility vs. reciprocal temperature and temperature of W-O thin films for duty cycles dc in-between 65-80 % of P . Black line is a fit obtained following a power-law temperature dependence of the mobility.

The gradual change of the electrical behavior of W-O films from metallic to semi-conducting and finally insulating-like materials as a function of duty cycle is evidenced. The loss of electrical conductivity, once again, agrees with Goldfard *et al.* results [99]. It corroborates Hall effect measurements with a significant decrease of the carrier concentration as duty cycles rises from 65 to 80 % of P , as shown in Figure 4.9a.

Hall voltage measured with our system was only substantial for this range of duty cycles and the sign of this voltage indicated that electrons are the majority carriers. It is worth to note that such a range correspond to the abrupt transition previously observed for optical transmittance and electrical conductivity (Figure 4.3). It also supports the most interesting window of oxygen-to-tungsten concentrations ratio vs. duty cycle showing that films gradually evolve from O-deficient to O-rich WO_3 compound (Figure 4.2). Films prepared with $dc = 75$ and 80% of P exhibit nearly the same carrier concentration (n close to $3 \cdot 10^{19} \text{ cm}^{-3}$) with a slight temperature dependence, which is typical of stoichiometric or weakly oxygen-deficient WO_3 [100]. For $dc = 70\%$ of P , n is higher than $4 \cdot 10^{20} \text{ cm}^{-3}$ with an invariant temperature dependence. The carrier concentration is more than 10^{21} cm^{-3} for films produced with $dc = 65\%$ of P . This large increase of the carrier concentration is directly connected to the oxygen vacancies in WO_{3-x} films produced for these deposition conditions. As the deviation from stoichiometric to strongly oxygen-deficient WO_3 compound is favored by reducing the duty cycle in the 60 - 80% of P range, the semiconductor-to-metal transition occurs. Deviation from stoichiometry creates donor levels due to oxygen vacancies [101]. The increasing concentration of donor centers (as duty cycle reduces) leads to the formation of donor conduction band, which overlaps the conduction band and tends to exhibit metallic-like properties (i.e. $n > 10^{21} \text{ cm}^{-3}$). It is interesting to note that for films prepared with $dc = 65\%$ of P , the carrier concentration becomes temperature dependent. This reduction of the carrier concentration as the temperature rises may be related to the increasing structural defects in the films produced by oxygen vacancies. These defects act as trapping centers for the charge carriers (i.e. free electrons) in the films [102]. In addition, decreasing the oxygen concentration in sub-stoichiometric metallic oxide films enhances their reactivity and the films become more sensitive to oxidation with an increase of temperature.

Carrier mobility vs. temperature is less influenced by the duty cycle (Figure 4.9 b) and remains is in the order of $1 \text{ cm}^2 \text{ V}^{-1} \text{ s}^{-1}$ for films prepared with $dc = 75$ and 80% of P , with no significant variations as a function of the temperature. The lowest room temperature mobility is about $0.2 \text{ cm}^2 \text{ V}^{-1} \text{ s}^{-1}$ for $dc = 65\%$ of P and tends to $1 \text{ cm}^2 \text{ V}^{-1} \text{ s}^{-1}$ as the temperature reaches 120°C . The temperature variation of the carrier

mobility suggests that there are various carriers scattering mechanisms, which are temperature dependent. At first, the carriers scattering can be related to the carriers mobility and intergranular potential according to a classical thermally activated process [103]. Nevertheless, the $\log \mu$ vs. $1/T$ plot of our films does not exhibit a clear linear evolution (Figure 4.9b). Therefore, the temperature dependence of carriers mobility has to be investigated taking into account lattice and impurity scattering mechanisms. It can be described by the empirical relationship $\mu \propto T^w$ where w is a positive or negative constant for scattering due to impurities or lattice, respectively [104]. Fitting from data reported in Figure 4.9b gives rise to a positive value with $w = 0.67$ for W-O films sputter deposited with $dc = 70\%$ of P and reaches 2.78 for $dc = 65\%$ of P . This temperature dependence is then associated to the scattering of carriers by defects (due to oxygen vacancies). Such defects act as neutral impurities since the w coefficient becomes higher than $3/2$, this latter value being commonly assigned to ionized impurities scattering phenomenon [104].

4.2. WO_x films by GLAD + RGPP

As in the previous work (§ 4.1), WO_x films were prepared combining GLAD and RGPP. GLAD technique was also introduced to produce various morphologies and structures. To this aim, a porous microstructure and appropriate W-O thin films were investigated so as to develop active layers for gas sensing applications.

4.2.1 Structure and morphology

Cross-section views of inclined thin films prepared with a duty cycle $dc = 100\%$ of P are observed by SEM for an incident angle $\alpha = 70, 75, 80$ and 85° (Figure 4.10). An inclined columnar structure is clearly obtained, whatever the incident angle.

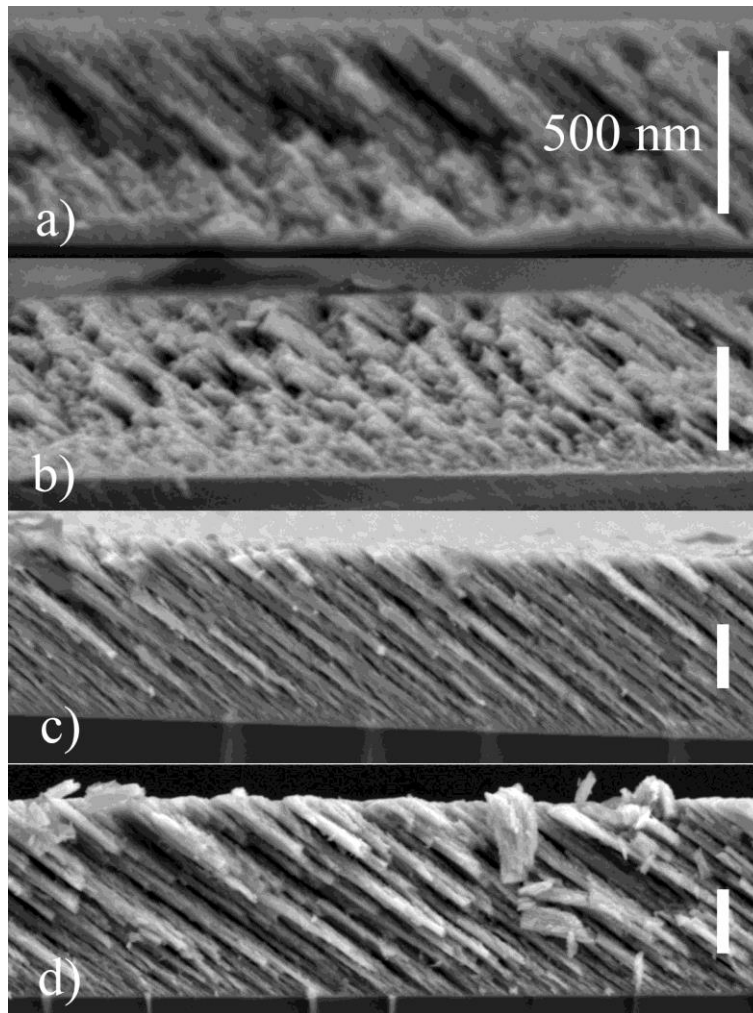


Figure 4.10 Inclined columnar structures of W-O thin films prepared with a duty cycle $dc = 100\%$ of P , and various incident angles a) $\alpha = 70^\circ$, b) $\alpha = 75^\circ$, c) $\alpha = 80^\circ$, and d) $\alpha = 85^\circ$.

Column angle β gradually increases from 45° to 55° as the incident angle changes from $\alpha = 70$ to 85° , respectively. Relationships between α and β angles can be compared with Tait *et al.* investigations [36], as shown in Figure 4.11. For incident angles $\alpha < 60^\circ$, the columnar structure is not so clear as metallic films like Cr, Ti, W and so on [36,105,106]. This kind of inclined columns exhibit a porous structure compare to conventional W-O films that we produced before without using GLAD (Figure 4.1d) [107].

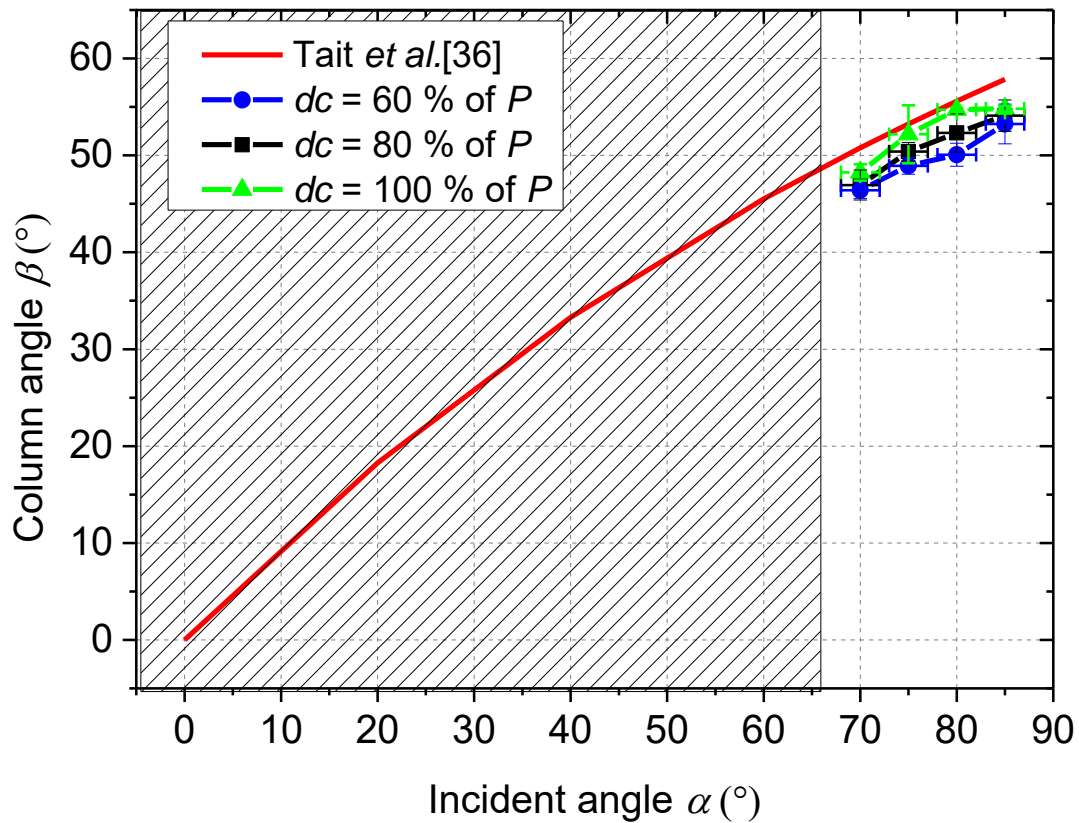


Figure 4.11 Column angle β vs. incident angle α of W-O films prepared with different duty cycles. β vs. α is also calculated from Tait et al. relationship [36]. Dashed region indicates that no columnar microstructure is observed in films prepared for $\alpha < 60^\circ$.

Based on the gas sensing performances of W-O thin films produced by RGPP (to see Figure 6.1 in chapter 5), and assuming that resistivity of porous architectures (inclined columns) is higher than that of conventional films (Figure 4.26), duty cycle of W-O films with a zigzag microstructure should be chosen at low duty cycle, in order to reach the suitable resistivity for zigzag gas sensors. Figure 4.12 exhibits zigzag structures prepared with an incident angle $\alpha = 80^\circ$, a duty cycle $dc = 30\%$ of P . Zigzag numbers are 1/2, 1, 2, 4, 8 and 16. Whatever the zigzag number, the average column angle is about 48° (taken from both directions). This value can be compared to those obtained in Figure 4.11, and correlates with Tait et al. investigations [36]. With a zigzag structure, one can also expect a porous thin film, as shown from the cross-section observations and compounds produced in conventional films (Figure 4.1d).

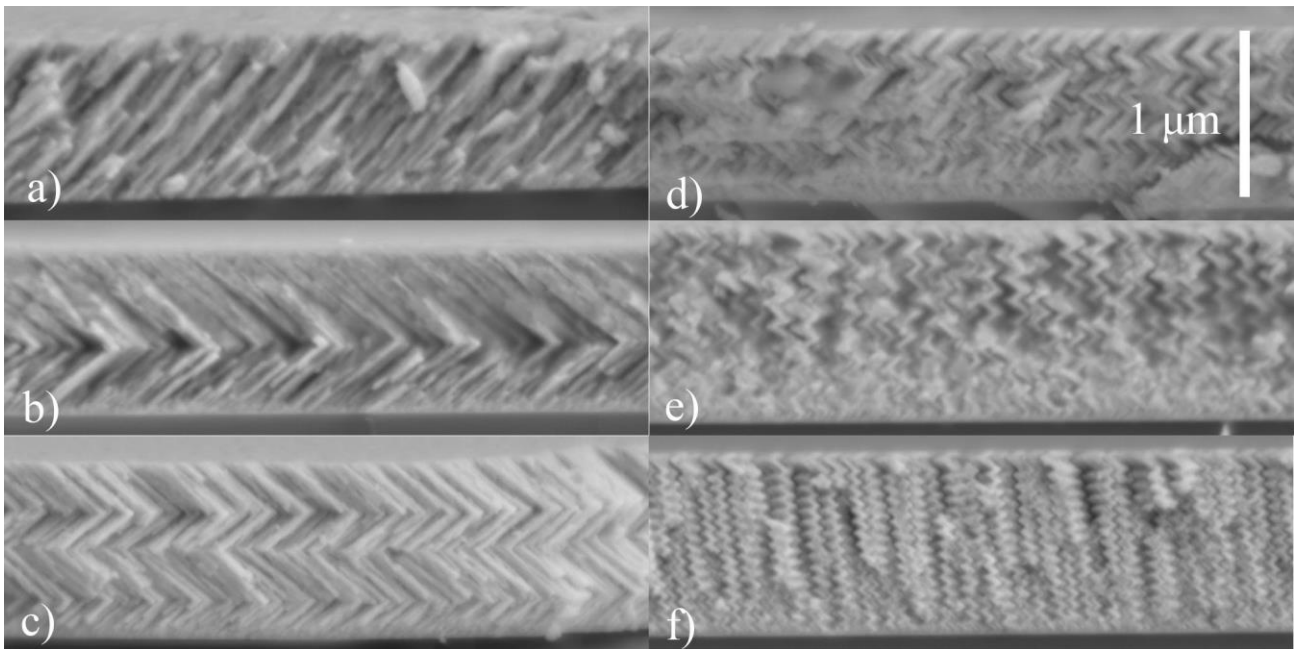


Figure 4.12 Zigzag structures of W-O thin films prepared with $dc = 30\%$ of P , an incident angle $\alpha = 80^\circ$ and various zigzag numbers a) 1/2, b) 1, c) 2, d) 4, e) 8, and f) 16.

Tungsten oxide films with a spiral microstructure are shown in Figure 4.13. They were prepared with a duty cycle $dc = 50$ and 60% of P , an incident angle $\alpha = 80^\circ$, and 4 pitches. Rotating speed of the substrate holder was adjusted taking into account the deposition rate. The speed was set so as to get 4 helices during the whole deposition time, which gives rise to a thin film thickness around 500 nm.

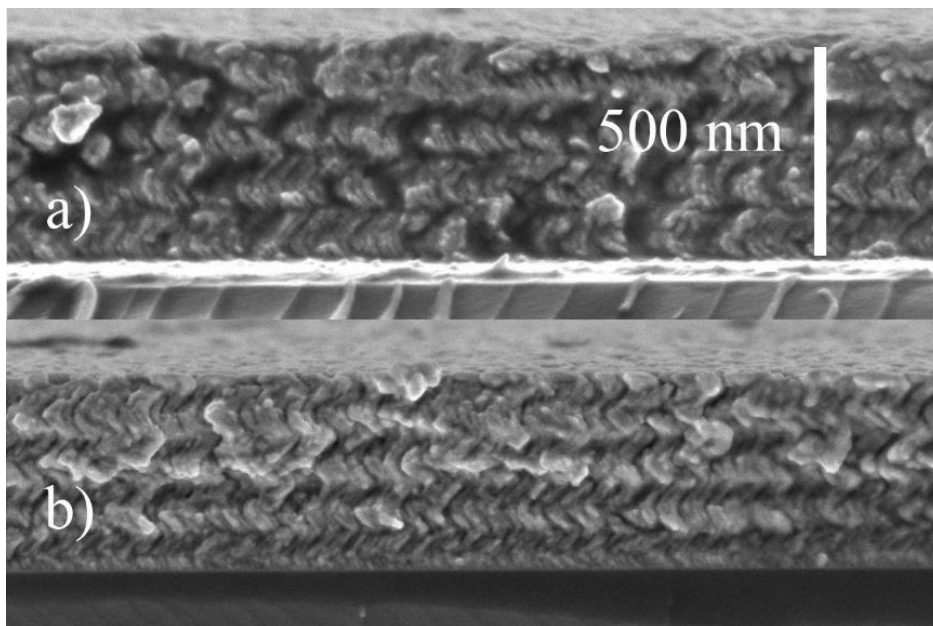


Figure 4.13 Spiral microstructures of W-O thin films with different duty cycles a) $dc = 50\%$ and b) $dc = 60\%$ of P , an incident angle $\alpha = 80^\circ$ and a number of pitches = 4.

Four turns are clearly viewed with voids and spaces between spirals. A porous microstructure is similar to those obtained in Figure 4.10 and Figure 4.12 but roughness and porosity seem to be less than that of inclined columns as shown in Figure 4.10.

In order to prepare W-O films as an active layer for gas sensors, inclined, zigzag and spiral microstructures were fabricated and post-annealed following their crystallinity by XRD. Inclined columns were prepared by the GLAD method with duty cycles $dc = 20$ to 50% of P . Zigzag microstructures were also prepared using the same procedure. Duty cycle dc was changed from 30 to 50% of P , zigzag number from 1 to 16 , and spiral microstructures were grown with the same duty cycle range and spiral number fixed at 4 . For all films, the annealing treatment was in air from 250 to $400\text{ }^\circ\text{C}$ for 12 hours. XRD patterns of films exhibiting all architectures, without annealing or with annealing lower than $300\text{ }^\circ\text{C}$, are shown in Figure 4.14 a.

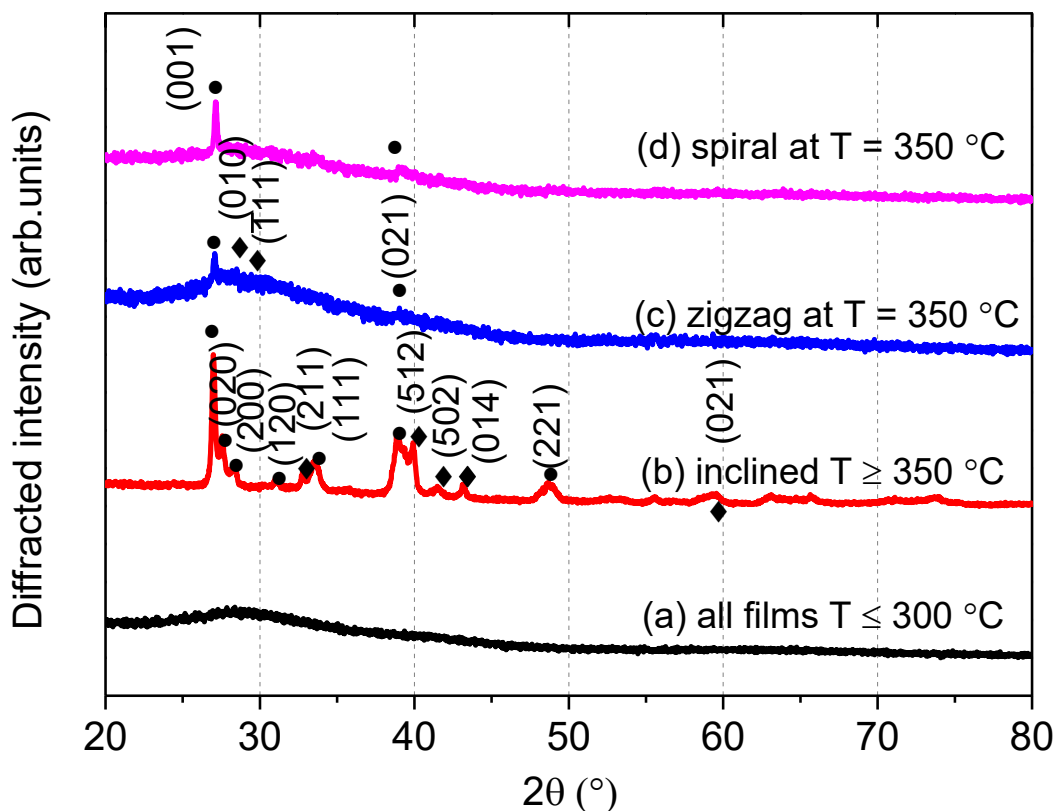


Figure 4.14 X-ray diffraction patterns of inclined, zigzag and spiral architectures of W-O thin films annealed in air for 12 h. a) An amorphous structure remains for all films annealed at temperature lower than $300\text{ }^\circ\text{C}$. b) Diffracted signals clearly appear for films with inclined columns annealed at temperature higher than $300\text{ }^\circ\text{C}$. c) Small peaks are recorded for zigzag structures annealed at $350\text{ }^\circ\text{C}$, and d) spiral structures annealed at $350\text{ }^\circ\text{C}$.

● = WO_3 (pdf # 20-1324); ◆ = $\text{W}_{18}\text{O}_{49}$ (pdf # 05-0392).

For annealing temperatures lower than 300 °C, no diffracted signals are recorded for any architecture. The inclined thin films with an annealing higher than 300 °C for 12 hours are shown in Figure 4.14b. Spiral and zigzag architectures annealed at 350 °C exhibit a nearly amorphous structure since only one weak peak is recorded at $2\theta = 28^\circ$. This peak corresponds to the (001) planes of WO_3 phase (pdf # 20-1324). Inclined columns annealed at temperature $\geq 350^\circ\text{C}$ exhibit clear diffracted signals. Peaks are mainly assigned to WO_3 (pdf # 20-1324) and $\text{W}_{18}\text{O}_{49}$ (pdf # 05-0392) phase mixture. For the pattern shown in Figure 4.14b, a strong peak related to (001) planes of WO_3 phase (pdf # 20-1324) is recorded at $2\theta = 26.97^\circ$. Other peaks can be noticed at $2\theta = 27.53^\circ$, 28.33° , which correspond to (020), (200) of WO_3 phase (pdf # 20-1324), and (010), ($\bar{1}11$) of $\text{W}_{18}\text{O}_{49}$ phase (pdf # 05-0392), respectively. Another intense peak (021) of the WO_3 phase (pdf # 20-1324) is measured at $2\theta = 38.88^\circ$ and another one (512) due to the $\text{W}_{18}\text{O}_{49}$ phase (pdf # 05-0392) appears at $2\theta = 39.93^\circ$. The rest are small peaks corresponding to these two phases.

4.2.2 Optical properties

At first, optical transmittance spectra in the visible region of W-O films exhibiting an inclined columnar microstructure were recorded (Figure 4.15). Films were prepared with a systematic change of duty cycle dc and incident angle α . For duty cycles lower than 65 % of P , films are completely absorbent. Semi-transparent or transparent W-O films are produced for $dc > 65\%$ of P and for any incident angle. For duty cycles higher than 90 % of P , typical interference fringes are clearly noticed, especially for the lowest incident angles. The highest amplitudes are recorded, which means that W-O films have a high refractive index. For incident angles $\alpha = 75$ to 85° , amplitudes of fringes are significantly reduced. This is mainly connected to the reduction of refractive index. A porous microstructure is produced, as expected for the highest incident angles. It is also worth to note that the absorption edge shifts to higher wavelength, particularly for $\alpha = 80$ and 85° . Such a shift has ever been reported by Charles *et al.* [75] and associated to the poorly crystallized or even amorphous structure of the films as previously shown from XRD results (Figure 4.14) i.e. a decrease of the optical bandgap due to more defects in the films as α rises (more impurity states in the band gap). For duty cycles $dc = 70$ and 80% of P , fringes are not as

homogeneous as those measured for films with $dc = 90$ and 100% of P . Films are semi-transparent and an absorption band close to $600-700\text{ nm}$ becomes significant. This range of duty cycles correspond to WO_{3-x} compounds, with a large amount of oxygen deficiencies. Transmittance is strongly affected by the incident angle due to the voids in the microstructure, which scatter the light. For higher incident angles, films become more and more porous and the average transmittance is enhanced.

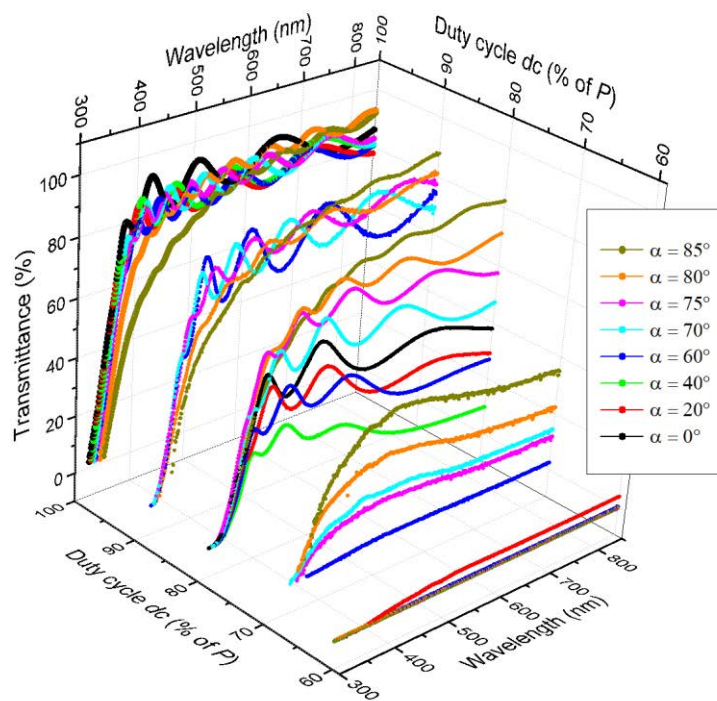


Figure 4.15 Optical transmittance spectra in the visible region of W-O thin films deposited on glass substrate for duty cycles higher than 60% of P and with different incident angles α .

An average transmittance at 633 nm defined as $T_{633\text{nm}} = 2T_M T_m / (T_M + T_m)$ (T_M and T_m are the optical transmittance from the envelope curves obtained from the peaks and valleys at 633 nm , respectively) of the films was calculated vs. incident angle α as shown in Figure 4.16. This figure clearly illustrates 3 types of optical behaviors connected to the duty cycle and incident angle. Absorbent films are produced for duty cycles lower than 60% of P and the incident angle has no effect on optical transmittance in the visible range. The chemical composition mainly influences the transmittance, i.e. by gradually adding oxygen, films become more and more transparent. Semi-transparent films are obtained for duty cycles in-between $60-70\%$ of P . Duty cycle and incident angle both act on the optical properties of the films.

Then, for $dc \geq 90\%$ of P , the incident angle is the main parameter, which leads to porous and rough thin films.

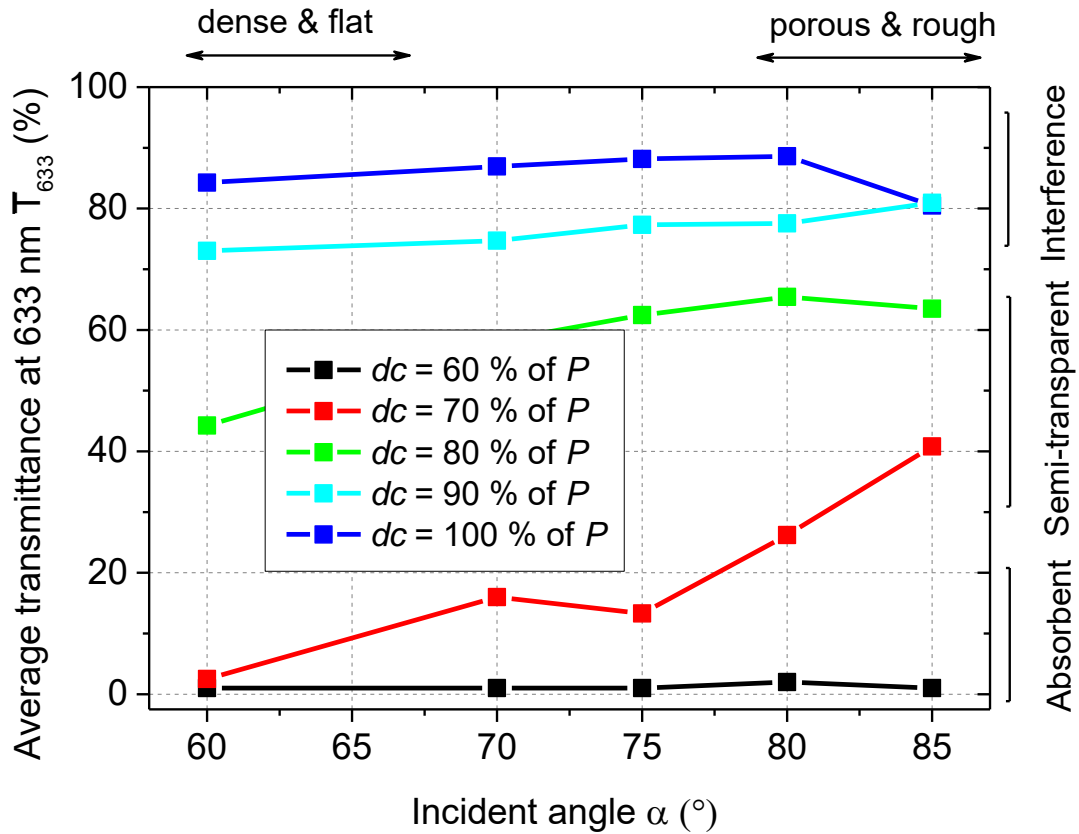


Figure 4.16 Average optical transmittance at 633 nm vs. incident angle α and for different duty cycles.

From optical transmittance spectra of transparent films deposited on glass substrate, the films porosity can be estimated. To this aim, we calculated the porosity π of the films according the Bruggeman effective medium approximation model [108].

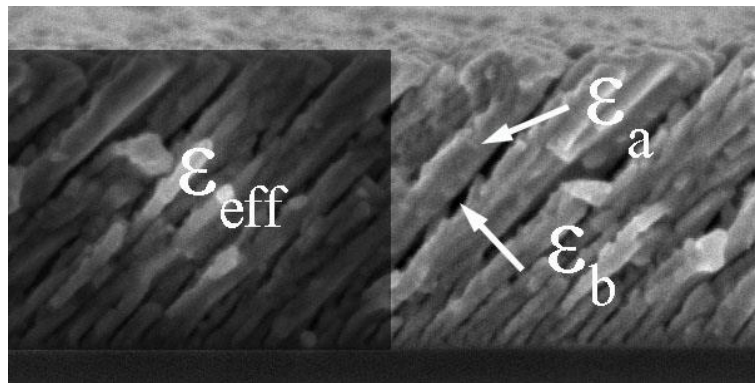


Figure 4.17 Illustration of Bruggeman effective medium approximation model in W-O thin films prepared with an incident angle $\alpha = 80^\circ$ and a duty cycle $dc = 80\%$ of P .

It uses to following equation:

$$\chi_a \left(\frac{\varepsilon_a - \varepsilon_{eff}}{\varepsilon_a + 2 \times \varepsilon_{eff}} \right) + \chi_b \left(\frac{\varepsilon_b - \varepsilon_{eff}}{\varepsilon_b + 2 \times \varepsilon_{eff}} \right) = 0 \quad (4.1)$$

where ε_a and ε_b represent the dielectric permittivity of a and b components, and ε_{eff} is the effective permittivity of the film. χ_a and χ_b are the volume fraction of a and b components, respectively ($\chi_a + \chi_b = 1$), as shown in Figure 4.17. In our films, a is related to WO₃ material and b represents the porosity.

The effective permittivity of the film is connected to the refractive index with:

$$\varepsilon = n^2 \quad (4.2)$$

The films porosity WO₃ also takes into account the refractive index of bulk tungsten trioxide compound ($n_b = 2.5$ at 633 nm [75]), and the refractive index n_{eff} of the film determined by the Swanepoel's method [109]:

$$n_{eff} = \sqrt{N + \sqrt{N^2 - n_{glass}^2}} \quad (4.3)$$

Where

$$N = 2n_{glass} \frac{T_M - T_m}{T_M T_m} + \frac{n_{glass}^2 + 1}{2} \quad (4.4)$$

n_{glass} is the refractive index of optical glass, which is assumed to be 1.51 at 633 nm. T_M and T_m are the optical transmittance from the envelope curves obtained from the peaks and valleys at 633 nm, respectively.

From equations 4.1 to 4.4, refractive index and porosity of the films were calculated. Figure 4.18 shows the evolution of refractive index n and porosity π as a function of the incident angle α and for duty cycles $dc = 80, 90$ and 100 % of P . It is worth noting that refractive index is significantly reduced when incident angle changes from 60 to 85° and for any duty cycle. The films porosity exhibits a reverse evolution vs. incident angle. The most important variation of n and/or π is obtained for films prepared with $dc = 80$ % of P while the lowest porosity reaches 10 % for $\alpha = 60^\circ$ and the highest is 50 % for $\alpha = 85^\circ$. The same

trend is obtained for all duty cycles, which means that the incident angle is the key parameter leading to a more voided microstructure.

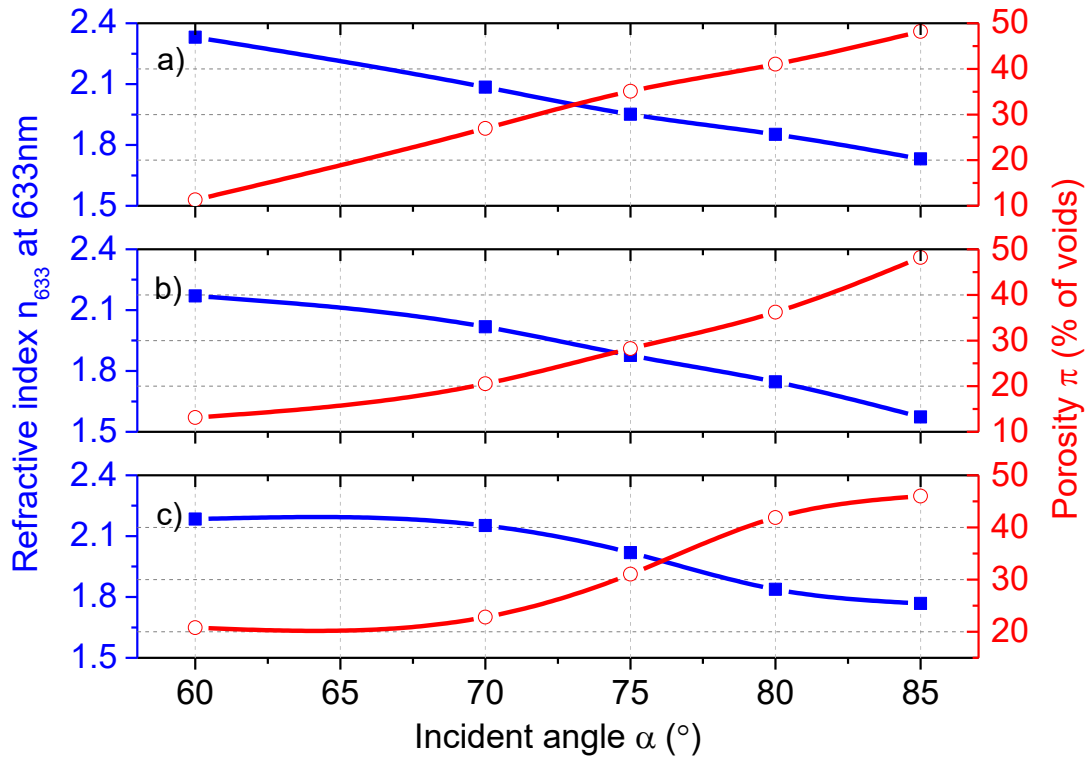


Figure 4.18 Refractive index n at 633 nm and porosity π vs. incident angle α for different duty cycles, a) $dc = 80\%$, b) $dc = 90\%$, and c) $dc = 100\%$ of P .

Optical transmittance was also measured for W-O films with a zigzag microstructure. These films were prepared with an incident angle α changing from 60 to 85 $^\circ$, duty cycle dc from 60 to 80 % of P , and zigzag numbers from 1 to 16 (Figure 4.19).

As expected, by increasing the incident angle α , amplitude of the fringes becomes less important due to the increasing porosity for the highest angles (specially for $\alpha = 80$ and 85°). It becomes even more significant when the zigzag number reduces. By decreasing the zigzag number, films tend to behave like inclined columnar microstructure.

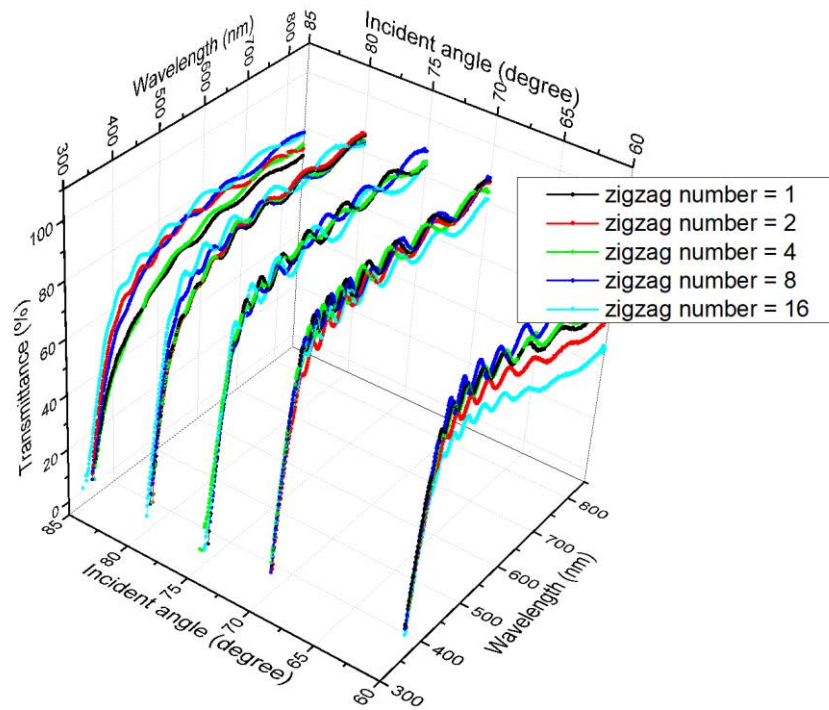


Figure 4.19 Optical transmittance spectra in the visible region of W-O films with a zigzag microstructure vs. incident angle and different zigzag numbers. All films were 500 nm thick and prepared with a duty cycle $dc = 80\%$ of P .

In addition, with a duty cycle $dc = 60\%$ of P , films become more absorbent because composition is the predominant factor influencing the optical transmittance (rather than the incident angle). For duty cycle higher than 70% of P , no clear effect of the zigzag number on the optical transmittance of the films is evidenced, except that films tend to behave as an inclined columnar microstructure when the zigzag number reduces down to 1.

Talking about the influence of zigzag number, the latter does not significantly affect the optical transmittance. Plotting the average transmittance at 633 nm as a function of the incident angle α and for duty cycles $dc = 70$ and 80% of P (Figure 4.20), one can compare with the value from inclined microstructure (Figure 4.16).

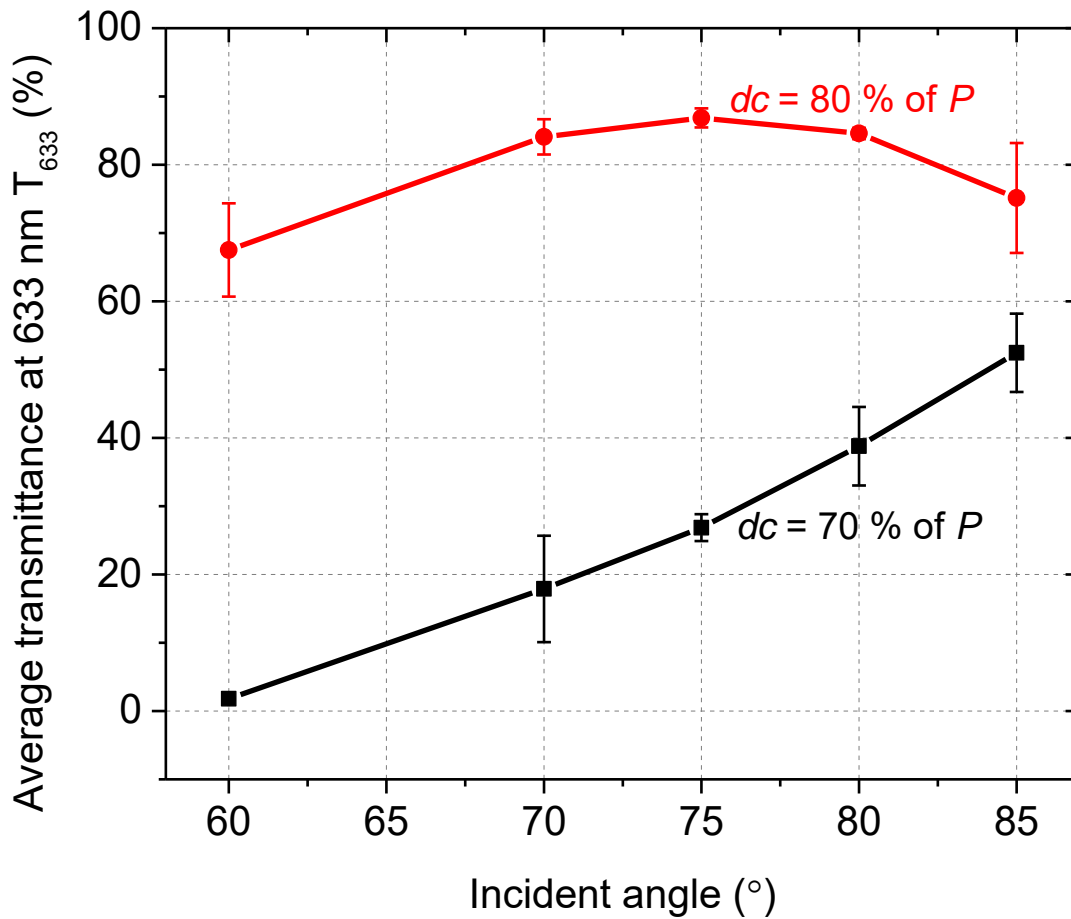


Figure 4.20 Average optical transmittance at 633 nm vs. incident angle α of W-O films with 4 zigzags and prepared with duty cycles $dc = 70$ and 80 % of P .

For both duty cycles, T_{633} vs. incident angle exhibit the same evolution. It shows again that the zigzag number does not influence the optical properties but rather the incident angle α , especially for $dc = 70$ % of P .

4.2.3 Electrical properties

In order to be measurable with our resistivity system, inclined columnar thin films were prepared varying duty cycle from 20 % to 70 % of P . Incident angle was systematically changed from 0 to 85°. Electrical resistivity of the films measured at room temperature is plotted vs. incident angle and for different duty cycles (Figure 4.21). All films systematically become more resistive as the incident angle increases. For the lowest duty cycle ($dc = 20$ % of P), $\rho_{RT} = 2 \times 10^{-5} \Omega \text{ m}$ for $\alpha = 0^\circ$ and it increases to one order of magnitude for $\alpha = 85^\circ$. Such resistivity increasing is more relevant for duty cycles $dc = 30$ to 70 % of P . For such deposition conditions, resistivity slightly increases as the incident angle varies from 0 to 60°. Afterwards, an abrupt jump is observed as the incident angle α becomes grazing (i.e. α tends to 85°). As

an example, resistivity starts at $2 \times 10^{-5} \Omega \text{ m}$ for $\alpha = 0^\circ$ and reaches near $2 \times 10^{-2} \Omega \text{ m}$ at $\alpha = 85^\circ$ for $dc = 60\%$ of P (i.e. 3 orders of magnitude). This sudden increase of resistivity from $\alpha \geq 60^\circ$ has ever been reported for GLAD metallic films [110]. It is mainly attributed to the formation of voids in the inclined columnar microstructure. Films become more and more porous as α tends to 85° , which reduces the mean free path of electrons and thus favors a high electrical resistivity. One can also assume the effect of composition (oxygen pollution) especially at high incident angle. One side of the substrate far from the W target receives a lower W flux and thus more oxygen atoms. In our case, the resistivity of samples was systematically tested in the same area to exclude the impact of the distance (i.e. between the target and the substrate). For duty cycles higher than 60% of P , the effect of oxygen becomes significant and for $dc = 80\%$ of P , the films resistivity is over $10^{-1} \Omega \text{ m}$ and becomes too high to be measured with our system as the incident angle increases.

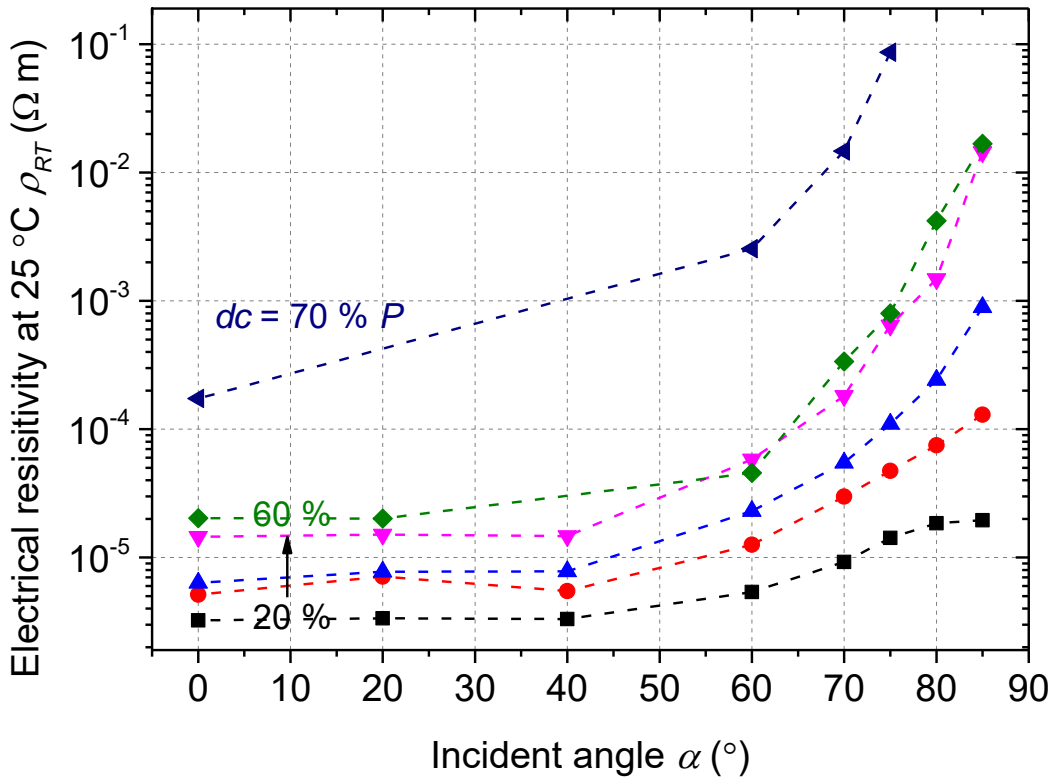


Figure 4.21 Electrical resistivity at room temperature vs. incident angle of inclined columnar W-O films for different duty cycles.

Electrical resistivity of the films vs. temperature was also measured from room temperature to 300°C . Figure 4.22 supports again that the electrical resistivity strongly depends on the duty cycle and incident

angle. Films exhibit a metallic-like behavior, turns to semiconductor and finally insulator while duty cycle increases. When the duty cycle is higher than 80 % of P , the samples are too much resistive to be measured. It is important to mention that the incident angle also affects the hysteresis loop during the temperature cycle. Surprisingly and for duty cycles $dc \geq 30$ % of P , resistivity can be reduced vs. temperature cycle for films prepared at low incident angle ($\alpha \leq 60^\circ$), whereas the loop shows a reverse evolution at higher incident angles ($\alpha \geq 80^\circ$), i.e. an increase of resistivity after a temperature cycle. A thermal oxidation of the films mainly gives rise to such increase of resistivity. About the surprising resistivity reduction after the temperature cycle, one may suggest that some Magnéli phases exhibiting a metallic-like behavior are partially produced for our sputtering conditions [111].

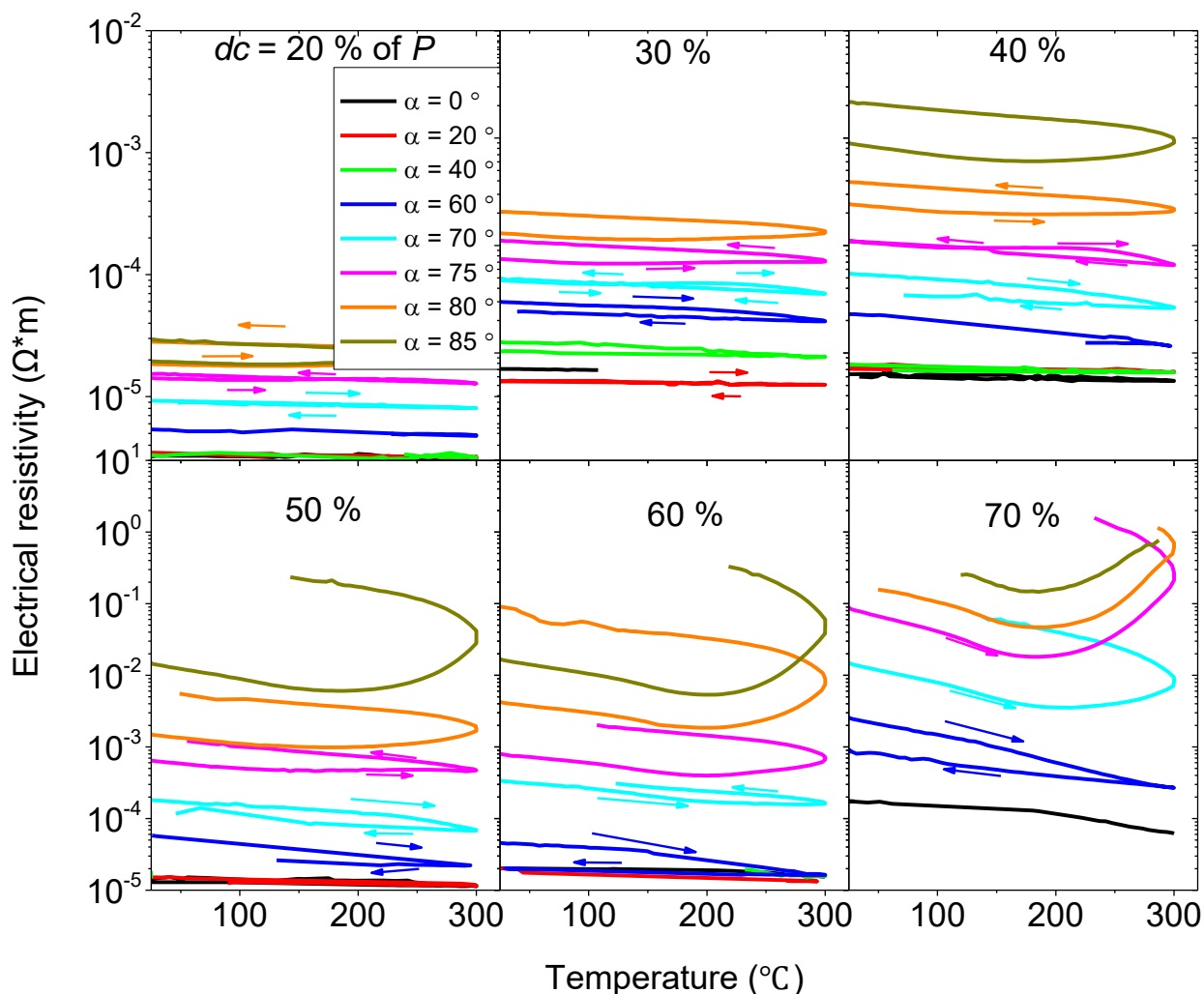


Figure 4.22 Electrical resistivity vs. temperature of inclined columnar W-O thin films deposited on glass substrate for duty cycles lower than 80 % of P and with different incident angles.

Several sub-stoichiometric WO_x compounds (where x changes from 2.6 to 2.9) have been reported by many authors [12,22,33]. Among these Magnéli phases, the charge carrier concentration becomes maximum ($n_e = 1.87 \times 10^{22} \text{ cm}^{-3}$) when the $W_{18}O_{49}$ compound is formed (i.e. $WO_{2.722}$). Such a compound exhibits a metallic-like behavior [112]. Increasing further the oxygen concentration leads to a reduction of the charge carrier concentration ($n_e = 2.90 \times 10^{21} \text{ cm}^{-3}$ for $W_{25}O_{73}$; i.e. $WO_{2.92}$) and finally the semiconducting nature is obtained reaching the WO_3 stoichiometry.

For zigzag structured thin films, there are three main parameters, which need to be controlled: duty cycle, incident angle and the zigzag number. The electrical resistivity was measured at room temperature, with duty cycles varying from 20 to 70 % of P , incident angles changing from 60 to 85°, and zigzag numbers from 1 to 16 (Figure 4.23).

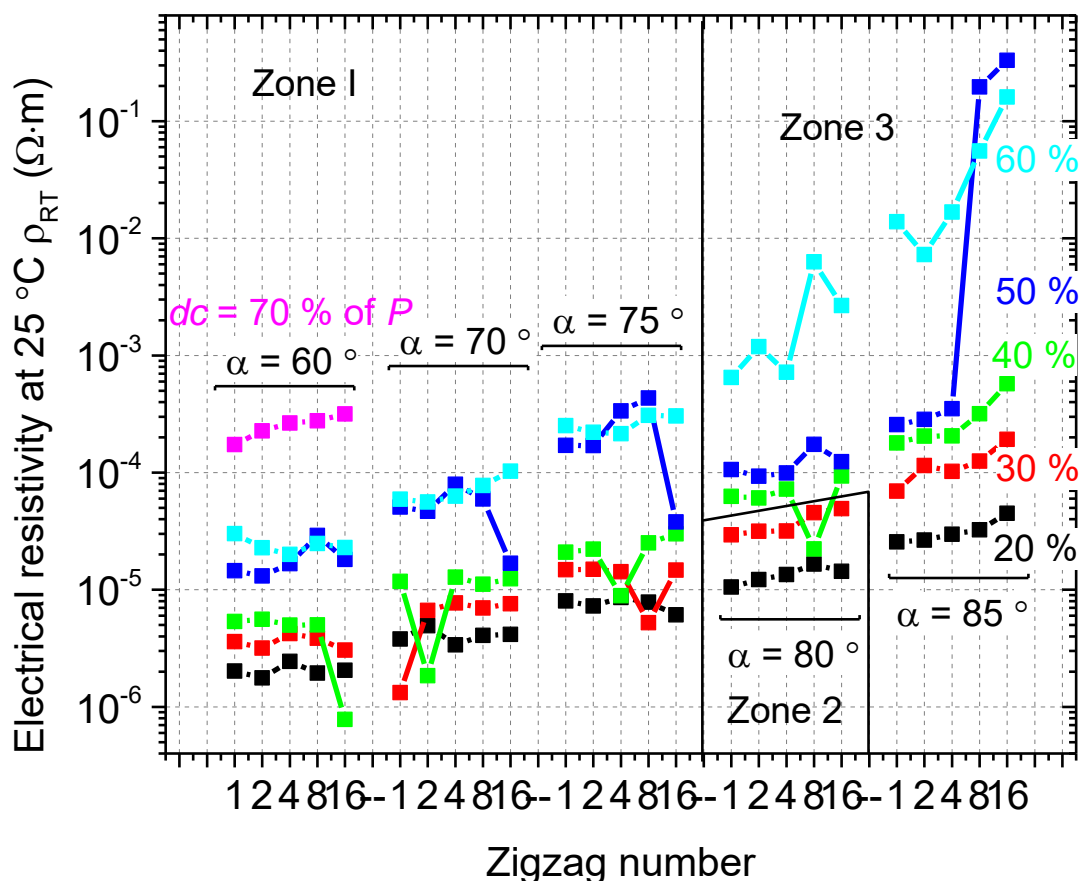


Figure 4.23 Electrical resistivity vs. zigzag number for different duty cycles and incident angles. Zone 1 concerns all films for incident angle lower than 75°, zone 2 for duty cycle $\leq 30\%$ of P and with an incident angle $\alpha = 80^\circ$, zone 3 for duty cycle $\geq 40\%$ of P and with an incident angle $\alpha = 80^\circ$ and all films with an incident angle $\alpha = 85^\circ$.

As previously noticed for inclined thin films, resistivity of zigzags shows the same behavior. Films prepared with low duty cycles and low incident angles exhibit the lowest resistivities ($\sim 10^{-6}$ to 10^{-5} Ωm). For any duty cycle, increasing the zigzag number and/or incident angle, systematically leads to more resistive films. For incident angles lower than 75° , duty cycle mainly influences the films resistivity, especially for dc higher than 40 % of P . For grazing incident angles (i.e. $\alpha \geq 80^\circ$), the zigzag number clearly influences the films resistivity for the highest duty cycles. Increasing the zigzag number to values higher than 8 gives rise to columns, which are normal to the surface. The zigzag architecture still remains as shown from SEM cross-section observation in Figure 4.12f. As a result, this wide range of electrical resistivities obtained for $\alpha = 85^\circ$ and $dc = 60$ % of P , and by increasing the zigzag number, is mainly due to a reduction of the column length (a few 10 nm for 16 zigzags) and thus a small electron mean free path.

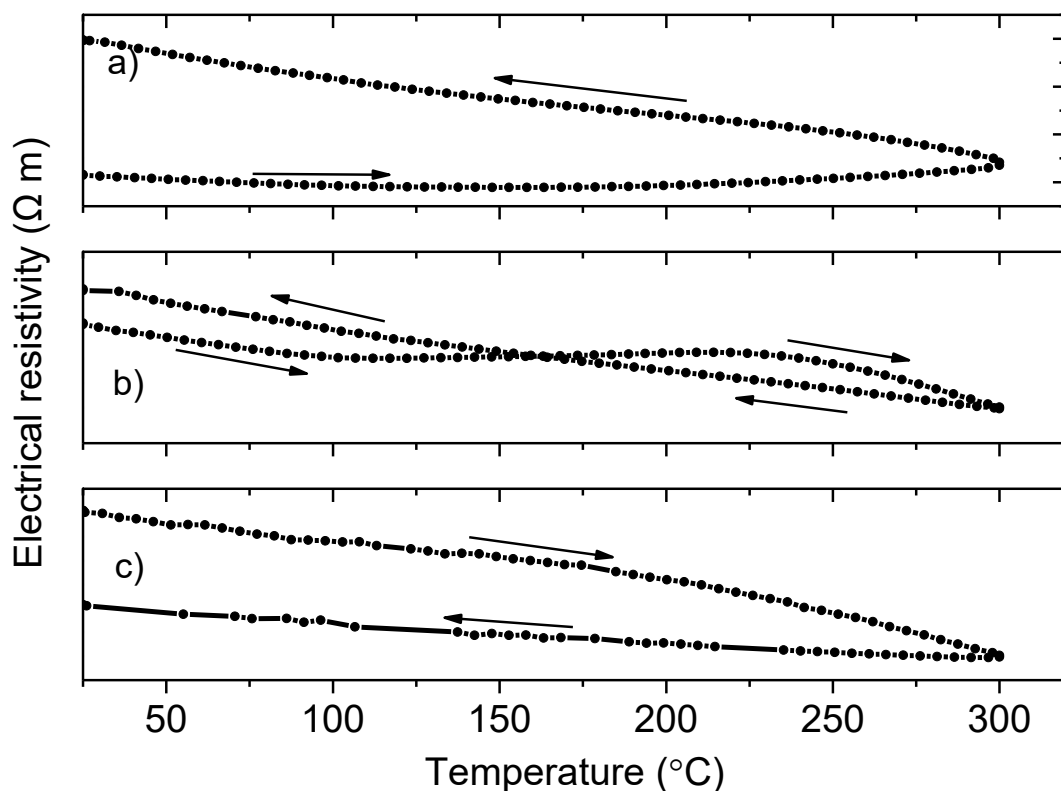


Figure 4.24 Three types of electrical resistivity evolution vs. temperature cycle of W-O thin films for a) an incident angle $\alpha = 85^\circ$ with any duty cycles and an incident angle $\alpha = 80^\circ$ with duty cycles higher than 40 % of P , b) incident angle $\alpha = 80^\circ$ with duty cycles lower than 30% of P , c) incident angles α lower than 75° with any duty cycle.

When the resistivity vs. temperature is investigated, there are three different types of evolution for films exhibiting a zigzag microstructure (Figure 4.24). The resistivity monotonically increases after one thermal cycle. This evolution occurs for zigzag films prepared with the highest incident angle of 85° and for duty cycles higher than 40 % of P (Figure 4.24a or Figure 4.23, Zone 1).

This resistivity increase is mainly due to the thermal oxidation of the zigzag structure. Zigzag films deposited with duty cycles lower than 30 % of P and high incident angles $\alpha \geq 80^\circ$ show again a surprising resistivity vs. temperature evolution (cross-like behavior as shown in Figure 4.24b or Figure 4.23, Zone 2). For zigzag films prepared with incident angles lower than 75° (and any duty cycle or zigzag number), resistivity reduces after a temperature cycle as shown in Figure 4.24c or Figure 4.23, Zone 3. (as previously reported for inclined columns in Figure 4.22). Again, this resistivity decreasing may be assigned to the partial formation of the $W_{18}O_{49}$ Magnéli phase exhibiting metallic-like properties [111,112].

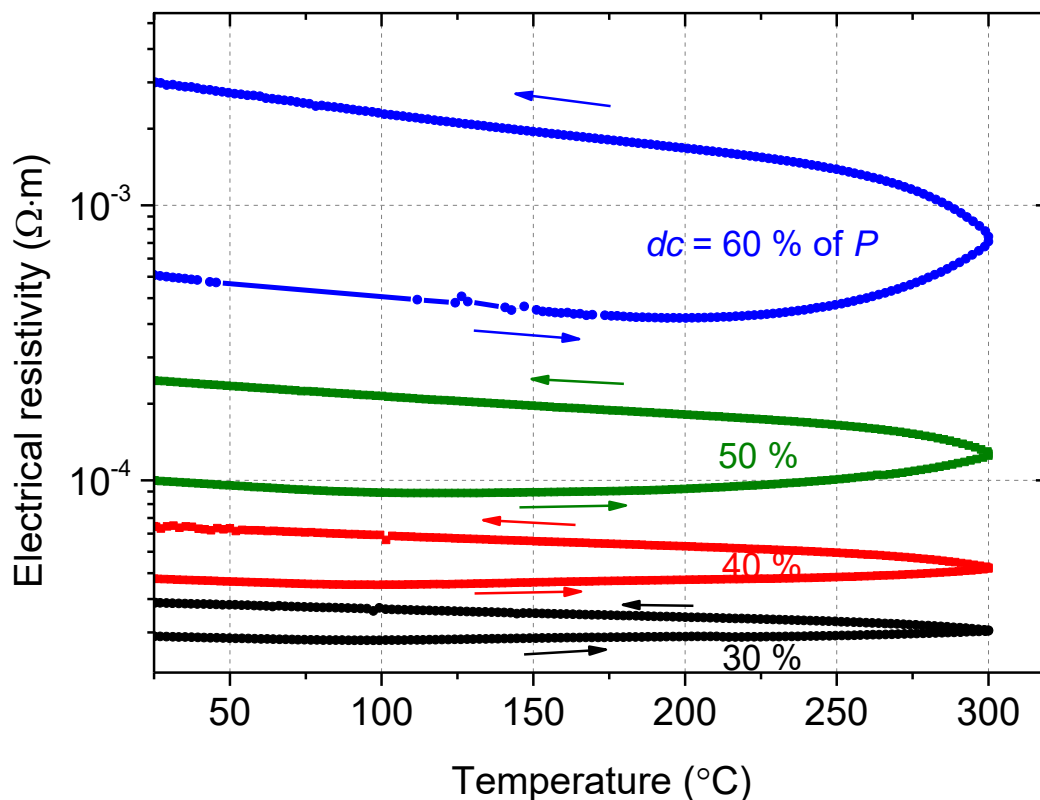


Figure 4.25 Electrical resistivity vs. temperature cycle for spiral microstructures of W-O films with different duty cycles, an incident angle $\alpha = 80^\circ$ and number of pitches = 4.

For W-O films prepared with a spiral microstructure, the resistivity vs. temperature was measured for a few samples, i.e. those prepared with an incident angle $\alpha = 80^\circ$, 4 pitches and duty cycle changing from 30 to 60 % of P (Figure 4.25). For duty cycles higher than 40 % of P , films exhibit an increasing resistivity with temperature cycle. Spiral films deposited with duty cycles lower than 30 % of P similarly show the resistivity reducing previously discussed for some inclined columnar and zigzag films (not shown here). The other films show a hysteresis loop evolution of resistivity vs. temperature typical of a thermal oxidation process, i.e. an increase of resistivity after the temperature cycle.

4.3. Conclusion

W-O thin films were deposited by DC reactive magnetron sputtering from a W target in argon + oxygen atmosphere. The Reactive Gas Pulsing Process (RGPP) was firstly involved to accurately change the chemical composition in the films from pure tungsten to over-stoichiometric WO_3 compound. These tunable W-O films were produced using a rectangular pulsing signal with a constant period $P = 16$ s and by means of a systematic change of the duty cycle dc from 0 to 100 % of P . These different and adjustable compositions have a clear influence on optical and electrical behaviors of the films since a gradual transition from metallic-to-semiconducting and finally insulating-like behaviors is evidenced. Various columnar architectures were produced by means of the GLancing Angle Deposition (GLAD) technique. Such a technique allowed the growth of different architectures: normal columns, inclined columns, zigzags and spirals. A wide range of electrical conductivities, from metallic to semiconducting-like behaviors, were reached playing with the duty cycle of RGPP and the two-key parameters of the GLAD technique, which are the incident angle (α) and the rotating speed of the substrate holder (ϕ). As a result, a large panel of compositions and architectures can be produced in W-O thin films combining GLAD + RGPP processes. In order to test these nanostructured films as an active layer for gas sensing, a suitable range (experience range further discussed in chapter 5) of the films' resistivity is required (Figure 4.26).

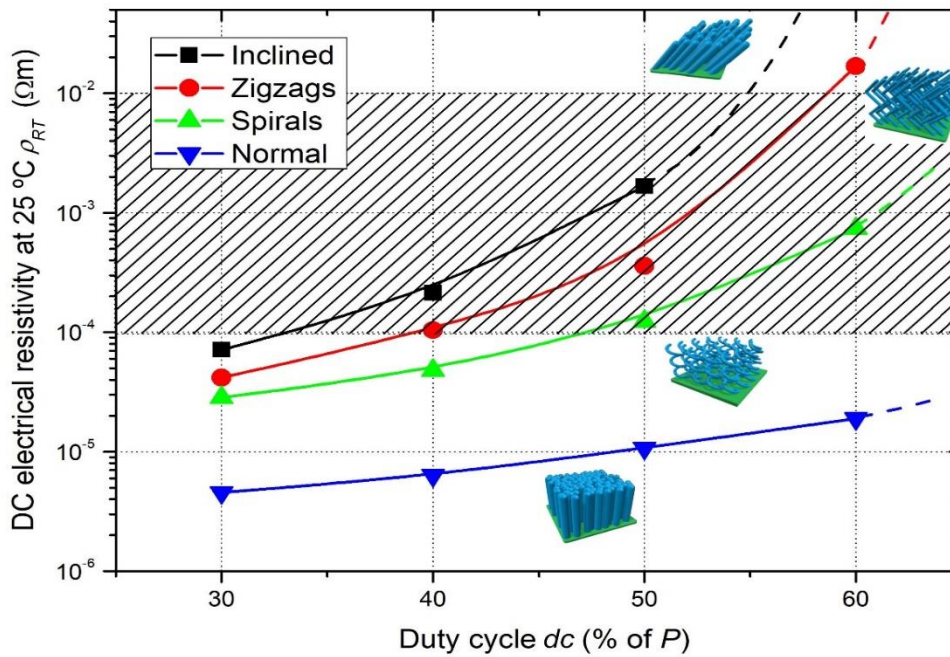


Figure 4.26 Electrical resistivity measured at room temperature as a function of the duty cycle for W-O films exhibiting inclined, zigzag, spiral and normal columnar architectures, $///$ = resistivity range for gas sensing.

Films prepared with normal incidence ($\alpha = 0^\circ$) exhibit the lowest resistivity due to a typical dense structure. Increasing the duty cycle gives rise to W-O films with a growing amount of oxygen, as previously reported and discussed in this chapter. For inclined columns, zigzag and spiral microstructures, resistivity systematically increases with duty cycle mainly due to an increasing oxygen concentration in the films. Such resistivity variation is more relevant for inclined columns, than zigzag and finally spiral microstructures. This is mainly ascribed to the porosity in the GLAD films. Such a porosity is more important in inclined columns than in zigzags and finally in spirals. One can expect the best sensing performances according to the same order (to see chapter 5).

5. Chapter 4: WO_x films by GLAD co-sputtering

Inclined columnar structures are produced implementing the GLAD co-sputtering technique by means of two opposite and inclined targets. Structure, morphology and electrical resistivity of the films are investigated. The strategy is first to use two W targets. By changing the second target current intensity and duty cycle dc of RGPP, one can expect an original control of the reactive co-sputtering process. In a second approach, oxygen is pulsed with a ring close to the second W target. Then two opposite W and WO₃ targets are co-sputtered in a reactive atmosphere using RGPP. The tungsten target current intensity I_W and WO₃ self-bias potential U_{WO_3} are separately modified, in order to tune the final properties of the films.

5.1. From two W targets

The two targets process was first implemented using two DC co-sputtered W targets. Due to different distances between each target and the substrate, two different fluxes can be expected, especially with RGPP. A ring was added near one target to further improve oxygen concentration of the flux from this target. This approach aims at producing a two components columnar microstructure in co-deposited thin films.

5.1.1 Structure and morphology by classical O₂ injection

Inclined columnar thin films prepared with duty cycle $dc = 40, 60, 80\%$ of P were first observed by SEM. The current intensity of the second tungsten target I_W was changed from 20 to 100 mA, whereas that of the first target was kept constant at 100 mA. It must be noted that the second tungsten target was sputtered without ring. An inclined columnar structure is clearly observed from the cross-section views (Figure 5.1).

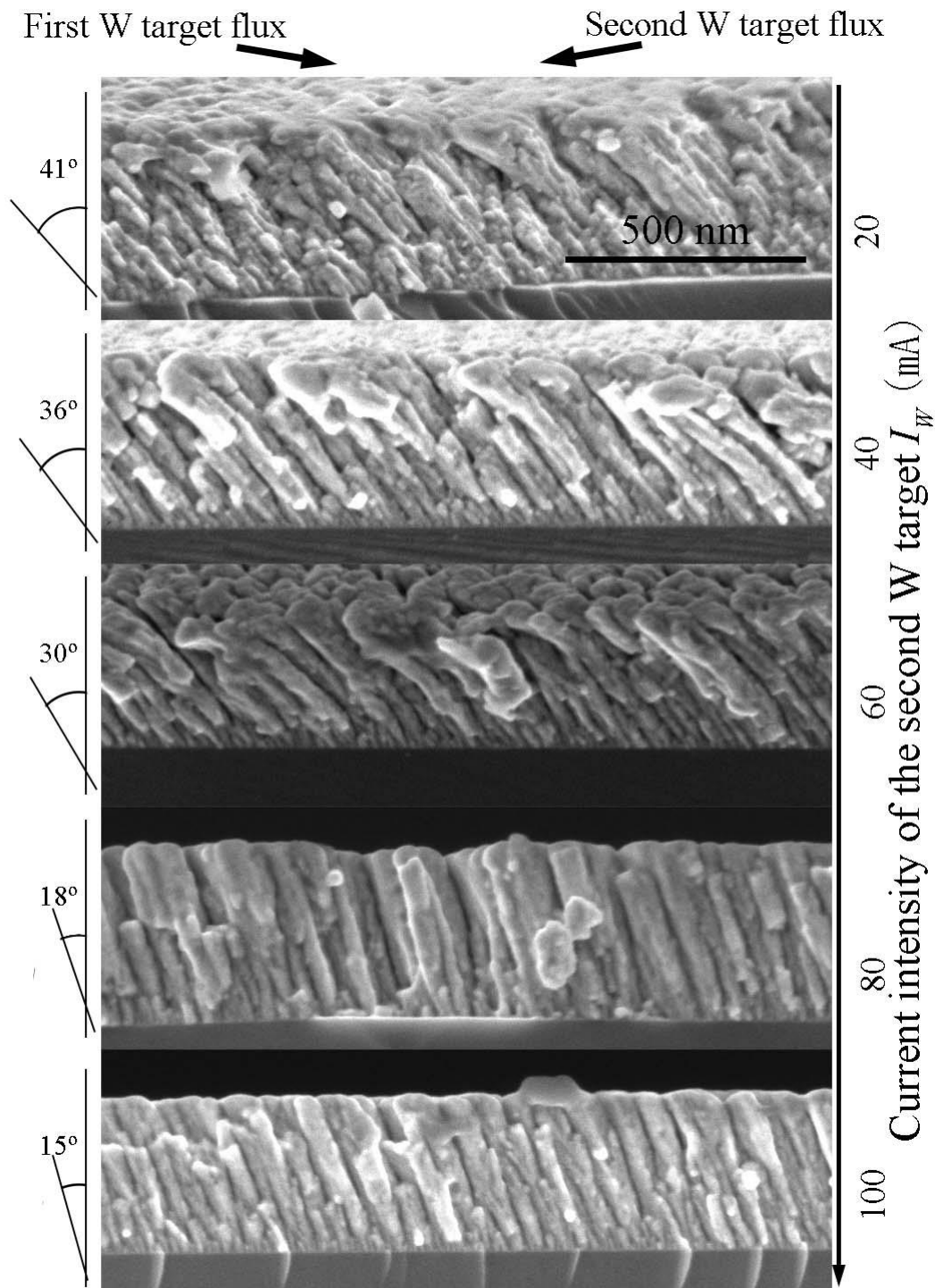


Figure 5.1 cross-section SEM views of W-O films co-sputtered by GLAD with duty cycle $dc = 60\%$ of P, the current intensity of the second tungsten target I_W changed from 20 to 100 mA, keeping that of the first tungsten target at 100 mA.

As expected, the column angle β decreases from 41 to 15° as the second I_W rises as shown in Figure 5.1. The column angle is not completely perpendicular to the substrate surface, while the two targets current are the same and equal to 100 mA. This can be explained by the distances between the targets and the substrate center, which are not the same (65 mm and 95 mm from Figure 3.2). As a result, the column

angle is 15° due to the highest W atoms flux coming from the W target the closest to the substrate (i.e. at 65 mm). It is worth to note that the column angle is always higher for W-O films co-sputtered with the highest duty cycle (80 % of P in Figure 5.2). For $dc = 40$ and 60 % of P , the co-sputtering process alternates between metal and oxidized sputtering modes. Thus, columnar growth is disturbed for such sputtering conditions, whereas the process becomes mainly in oxidized mode for $dc = 80$ % of P .

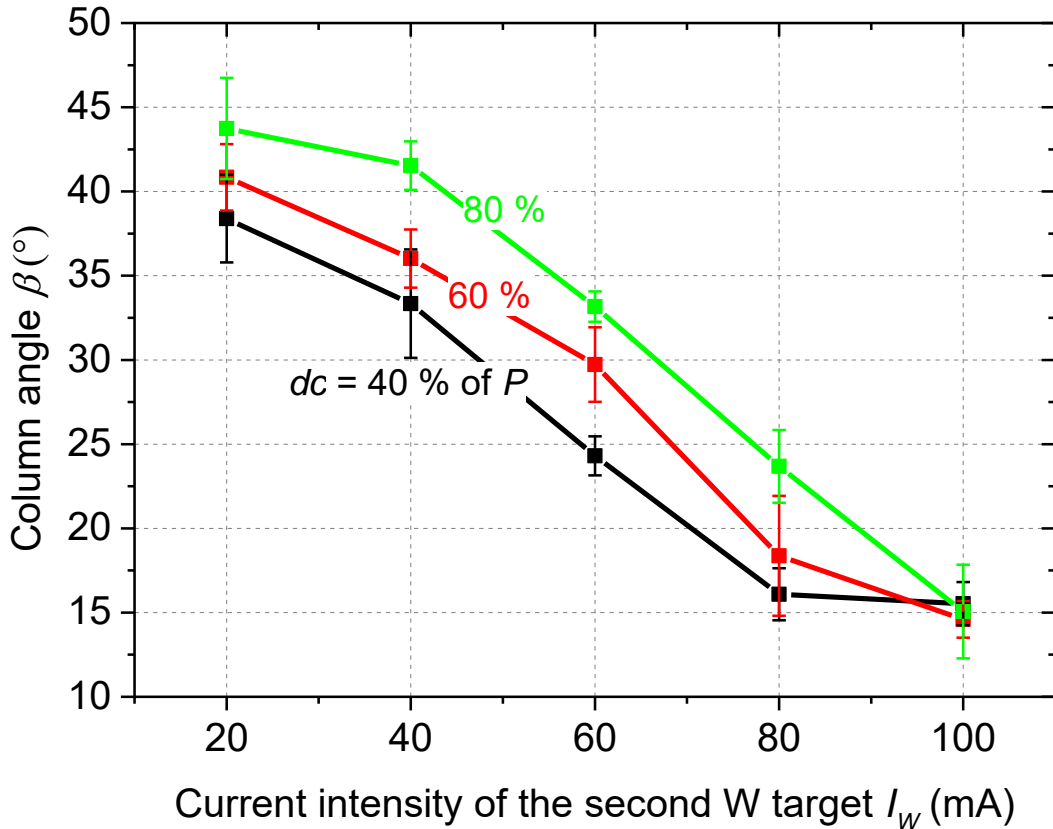


Figure 5.2 Column angle vs. current intensity of the second W target for 3 different duty cycles.

The optical transmittance in the visible region of W-O films deposited on glass is also influenced by 3 different duty cycles dc and the second tungsten target current I_W (Figure 5.3). Films are completely absorbent (or strongly) for the lowest duty cycles and for any second tungsten target current I_W .

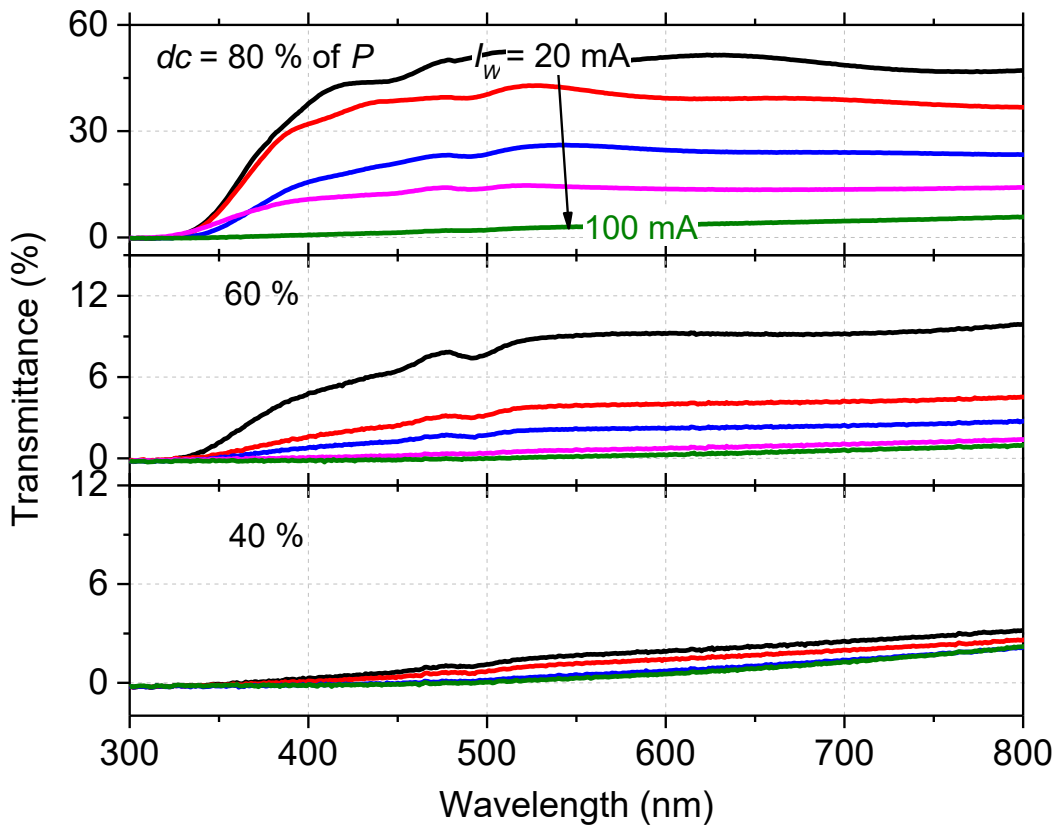


Figure 5.3 Optical transmittance spectra in the visible region of W-O films with different duty cycles and current intensities on the second tungsten target.

Films becomes transparent and typical interference fringes are produced in the visible region spectrum for duty cycles higher than 80 % of P and second tungsten target current $I_W = 20$ mA, as shown in Figure 5.3. While the second tungsten target current I_W is increased, the transmittance decreases for any duty cycle due to a larger amount of W in thin films. They tend to exhibit a metallic-like behavior.

5.1.2 O₂ injection close to one W target

In order to poison a W target surface but keeping the other W target in the metallic sputtering mode, the oxygen injection was located close to the second target (95 mm from the substrate center) by means of a ring (diameter of ring = 60 mm) surrounding the 2-inch W target. Such a ring consists of a pipe (diameter of pipe = 4 mm) with 16 holes (diameter = 1 mm) distributed equidistantly on the ring perimeter. From real-time measurements of each target potential, the reactive co-sputtering process was investigated without and with the ring. Figure 5.4 shows the targets potential vs. time when oxygen is

pulsed for a duty cycle $dc = 60\%$ of P , without and with the ring. The first target current intensity is $I_{W1} = 100$ mA, and the second target current intensity is $I_{W2} = 60$ mA.

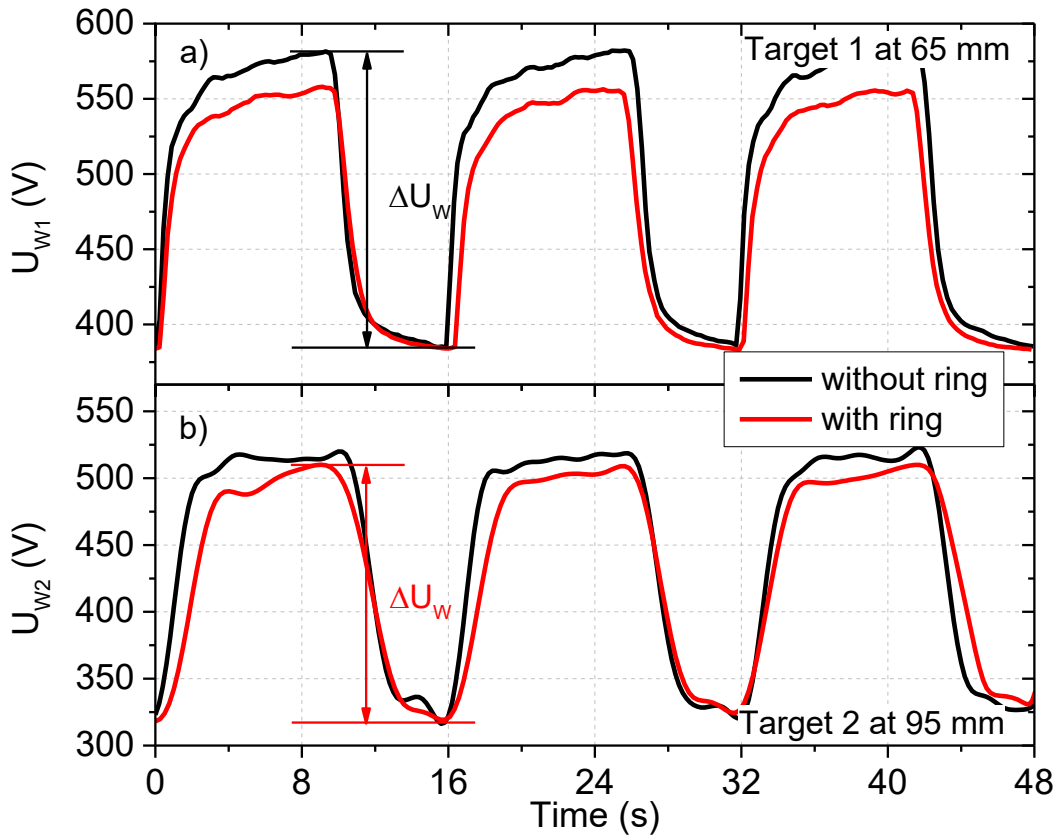


Figure 5.4 W targets potential of the first (U_{W1}) and second target (U_{W2}) vs. time when oxygen is supplied with and without a ring close to the target 2. Duty cycle $dc = 60\%$ of P , $I_{W1} = 100$ mA, and $I_{W2} = 60$ mA.

U_{W1} and U_{W2} both follow a periodic variation vs. time, which directly correlates with the oxygen pulsing signal (T_{ON} and T_{OFF} times of 9.6 and 6.4 s, respectively). With and without ring, both targets become poisoned after a few seconds of T_{ON} time (upper U_W values) and are restored to the metallic mode at the end of the T_{OFF} time. ΔU_W of the second target is nearly the same with or without ring, which means that the oxygen pollution is nearly equivalent. On the other hand, ΔU_W of the first target reaches more than 10 V lower value at the end of the T_{OFF} time (Figure 5.4 a). This would suggest a less poisoned state with the ring. However, the high target potential (higher than 550 V) rather corresponds to an oxidize sputtering mode. As a result, the use of such a ring does not allow poisoning of one W target while keeping the other one in the metallic state. In addition, the voltage differences without ring and for both

targets are always higher than with a ring (Figure 5.5), which indicates that the ring does not change the poisoning state during T_{ON} and T_{OFF} times.

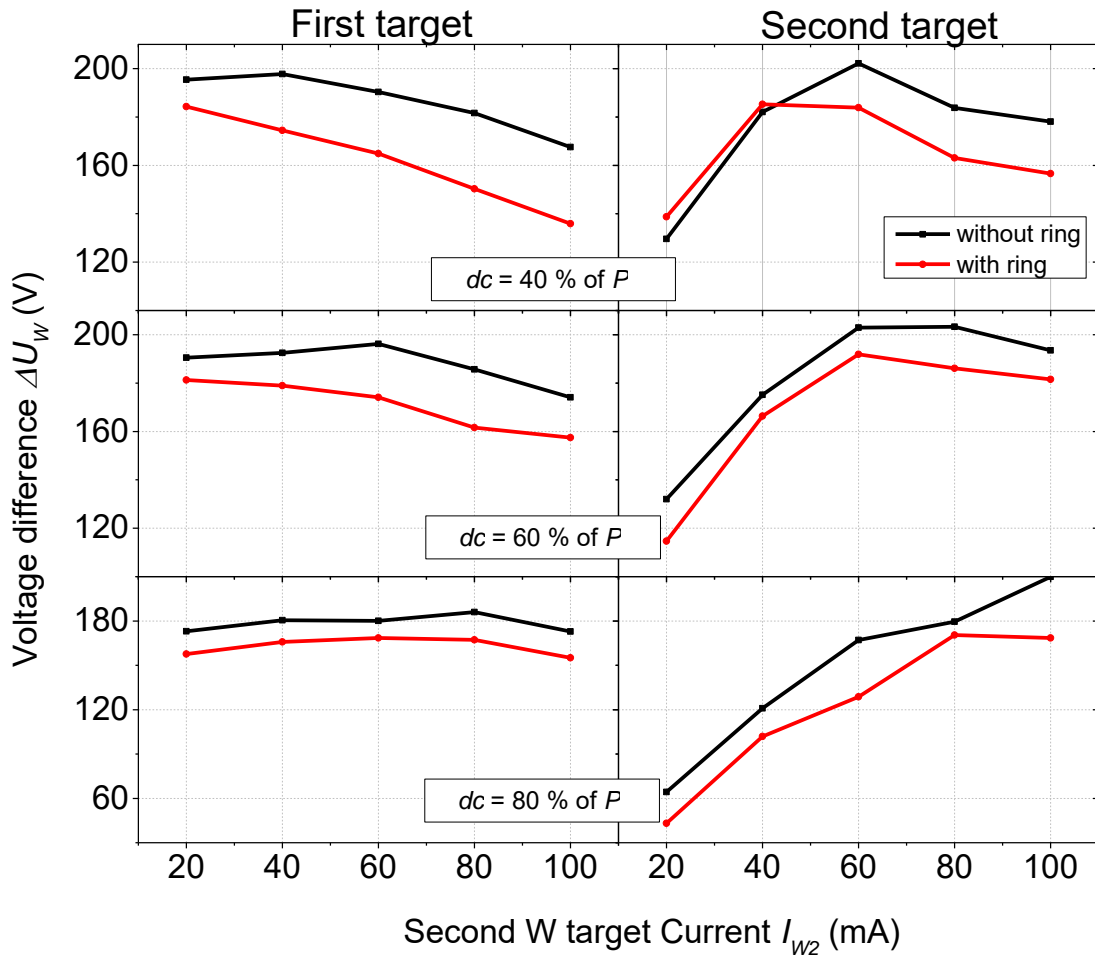


Figure 5.5 Voltage difference ΔU_w for the first W target and second W target vs. second W target current I_{w2} and for different duty cycles with or without ring for the oxygen supply, $I_{w1} = 100$ mA.

Thus, the ring does not influence the poisoning of both targets and cannot change one target sputtering mode while the other one is sputtered in another mode.

5.2. From W target and WO_3 target

Based-on results from § 5.1, the two W targets co-sputtering process did not allow getting a metallic state for one target and an oxidized one for the other one. As a result, a RF WO_3 target was sputtered instead of a DC W target.

5.2.1 Varying the DC sputtering of W target

Co-sputtering GLAD process was developed using two kinds of targets during deposition. Since many parameters may influence the film properties, univariate analysis was considered. We only changed one parameter at a time. Current intensity of DC sputtering of W target was firstly changed.

a) Structure and morphology

W-O films were prepared by reactive co-sputtering of tungsten and tungsten trioxide targets. Both targets were glanced at 80° to the substrate normal. Deposition rate and column angle were determined by using SEM cross-section views (Figure 5.6).

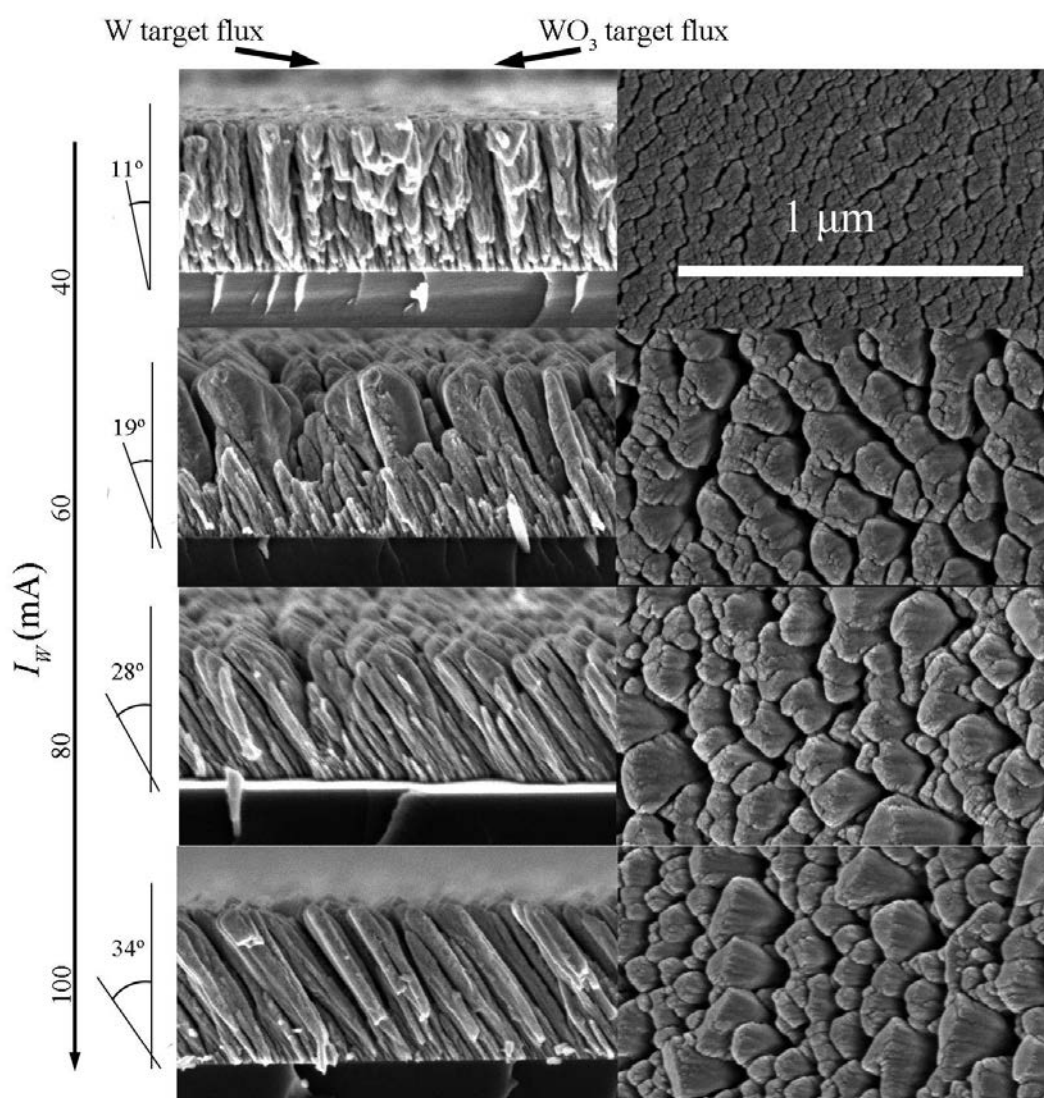


Figure 5.6 SEM views (cross-section and top) of W-O films co-sputtered by GLAD with self-bias potential of WO₃ target $U_{WO_3} = 300$ V and different current intensities on W target without RGPP.

The self-bias potential of WO_3 target was kept constant at $U_{\text{WO}_3} = 300$ V whereas the current intensity of W target I_W was changed from 40 to 100 mA (20 mA per step). As expected, deposition rate rapidly increases vs. I_W from 230 to 400 nm h^{-1} (Figure 5.7). For $I_W = 40$ mA (minimum I_W required to ignite the plasma on W target) and $U_{\text{WO}_3} = 300$ V, the column angle $\beta = 11^\circ$, which is nearly perpendicular to the substrate surface. From SEM top views, columns become bigger and more inclined as I_W increases. The column angle increases from 11 to 34° as I_W rises from 40 to 100 mA. Column angle β also becomes higher while the W target current intensity increases, because the deposition rate (due to the second W target) increases linearly vs. I_W . The resulting total deposition rate due to both targets increases as well, and the column angle is mainly influenced by the W target (β increases from 11 to 34°). A dense film with a low column angle ($\beta = 11^\circ$) is clearly produced for the lowest $I_W = 40$ mA, whereas larger columns are observed from $I_W = 60$ mA with an increasing column angle. This microstructural evolution supports again that W target flux prevails over that of WO_3 .

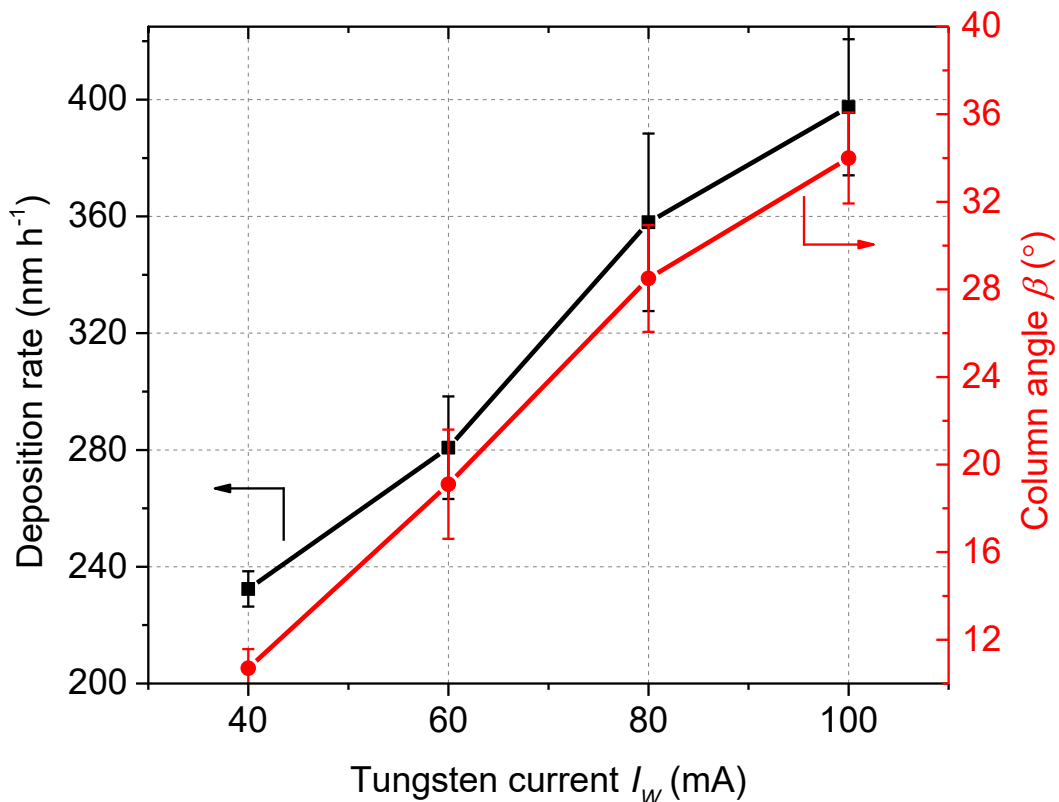


Figure 5.7 Deposition rate and column angle vs. tungsten target current.

X-ray diffraction patterns of co-sputtered films with $U_{WO_3} = 300$ V and various I_W are shown in Figure 5.8. Peaks corresponding to the β -W phase (pdf # 65-6453) are clearly recorded for all W target currents. Films prepared with $I_W = 40$ mA are poorly crystallized whereas the films' crystallinity is enhanced as I_W rises. An increase of I_W leads to a high intensity of diffracted signals corresponding to (200) plans at $2\theta = 41.58^\circ$.

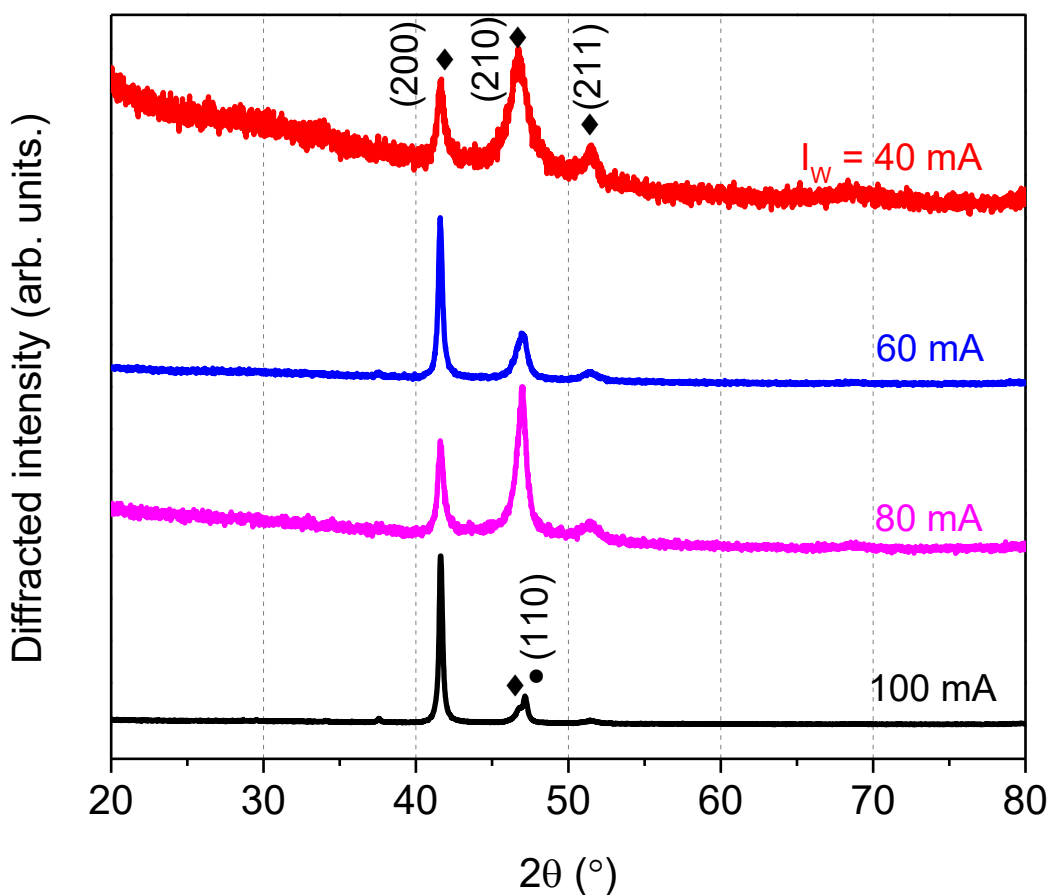


Figure 5.8 X-ray diffraction patterns of W-O thin films deposited on glass with various current intensities on W target and a constant self-bias potential $U_{WO_3} = 300$ V on the WO_3 target. \bullet = W (pdf # 04-0806); \blacklozenge = β -W (pdf # 65-6453).

In addition, peak at $2\theta = 51.53^\circ$ vanishes and it tends to give rise to a preferential orientation along (200) plans. These results show that a significant amount of oxygen still remains in the films in spite of a high W target current.

b) Electrical properties

An annealing treatment in air was applied to W-O thin films prepared by GLAD co-sputtering. They were all heated for 12 hours in air at 300°C . The goal of such annealing was to investigate and understand

the evolution of the films electrical properties, especially for a further application as gas sensors. Electrical resistivity was measured vs. time during such a treatment (Figure 5.9). For the lowest I_W target current intensity ($I_W = 40$ mA), resistivity remains quite stable as a function of the annealing time ($\rho \sim 5 - 6 \times 10^{-5} \Omega \text{ m}$ after 12 hours). This relative stability can be connected to the dense microstructure previously observed from SEM pictures (Figure 5.6). For $I_W = 60, 80$ and 100 mA, the same ρ vs. time evolution is recorded. An increasing I_W favors the metallic-like behavior of the films (ρ drops from 6.5×10^{-5} to $3.2 \times 10^{-5} \Omega \text{ m}$ before annealing) mainly due to an increase of their tungsten content.

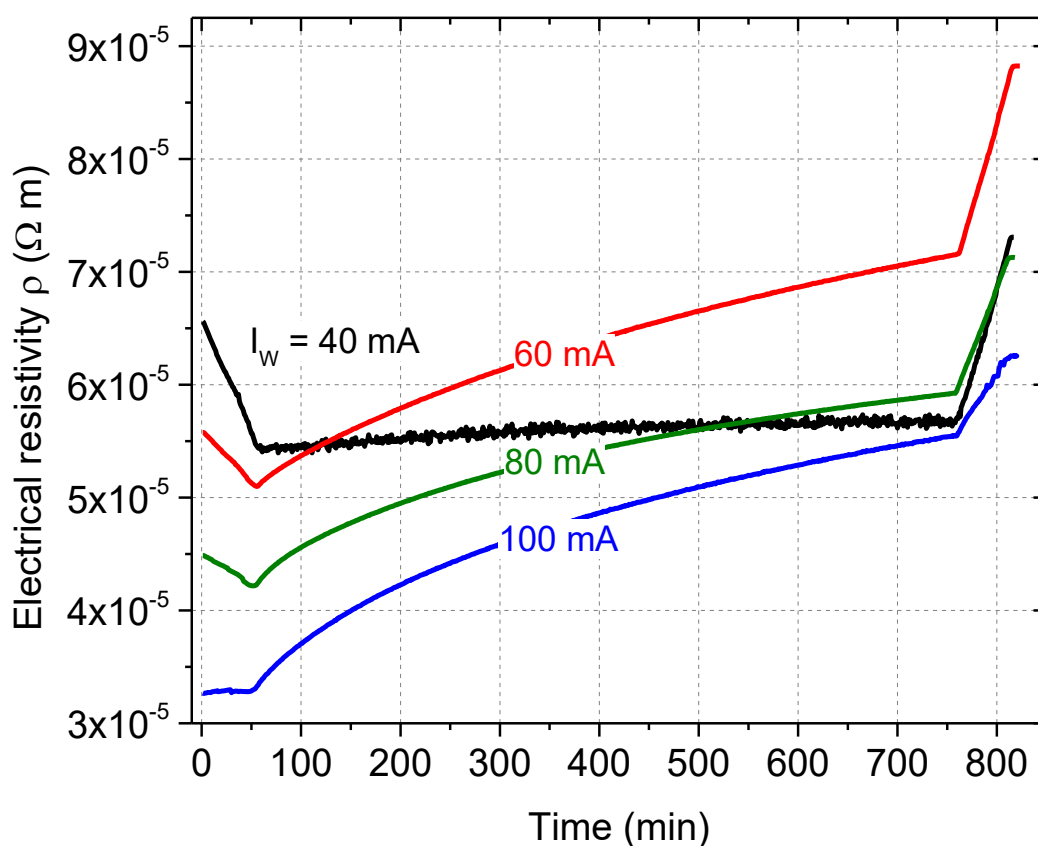


Figure 5.9 Electrical resistivity vs. time of W-O films prepared on glass substrates and annealed in air at 300 °C for 12 hours with various tungsten target current intensities and a constant WO_3 self-bias potential $U_{WO_3} = 300$ V.

Films become more porous and tungsten-rich as I_W increases. Despite the more voided microstructure, the film oxidation during annealing becomes less and less significant when I_W increases from 60 to 100 mA, since the amount of W rises in these co-sputtered inclined columnar films.

5.2.2 Varying the RF sputtering of WO₃ target

A constant current intensity of the W target is implemented whereas the self-bias potential of tungsten trioxide target is systematically changed from $U_{WO_3} = 100$ V (minimum potential to ignite the RF plasma) up to 300 V. Tuning U_{WO_3} in this range allows a stable co-sputtering process with composition changing from W to WO₃-rich films.

a) Structure and morphology

SEM cross-section and top views of films prepared with $I_W = 100$ mA and various U_{WO_3} are shown in Figure 5.10. An inclined columnar microstructure is clearly observed for any WO₃ self-bias potential. Columns are systematically tilted with an angle $\beta = 35 - 37^\circ$ oriented following the W particle flux. This means that sputtering flux of the W target prevails over that of WO₃ target.

It is also interesting to note that two kinds of columnar microstructures can be distinguished from the SEM top views whatever the WO₃ self-bias potential. The first one consists of narrow columns (width of a few tens nanometers) and more or less circular. The second one exhibits columns with an elliptical shape and a strong anisotropic microstructure, i.e. a big columnar width (a few hundreds of nanometers) in the direction normal to the W particle flux. This type of anisotropic microstructure is typical of tungsten thin films prepared by GLAD [57]. As a result, it supports that for these deposition conditions ($I_W = 100$ mA and $U_{WO_3} = 100$ to 300 V), particle flux coming from the W target mainly influences the final microstructure of W-O films produced by GLAD co-sputtering from W and WO₃ targets.

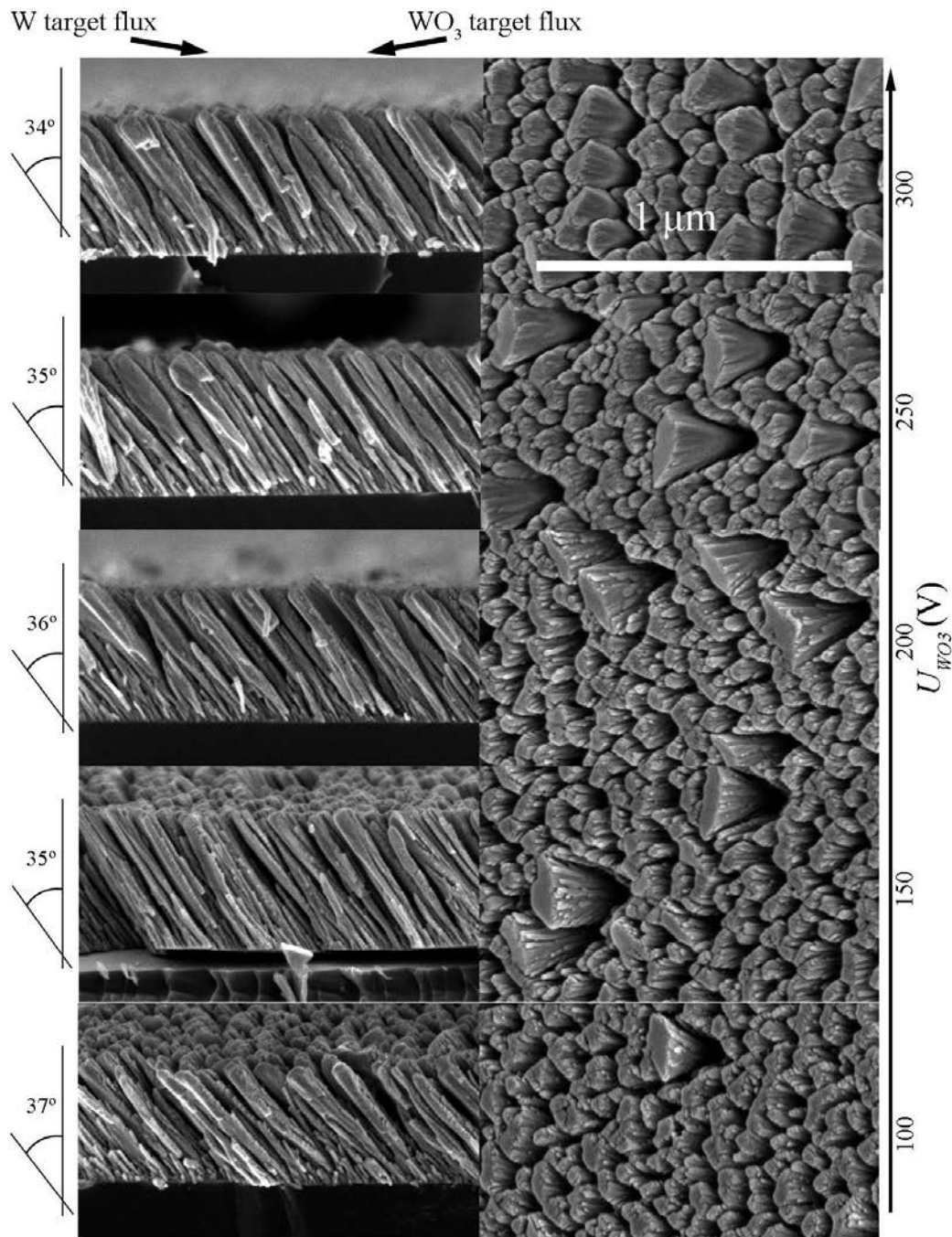


Figure 5.10 SEM views (cross-section and top) of W-O films co-sputtered by GLAD with a constant W target intensity $I_w = 100$ mA and various WO_3 target self-bias potentials.

The evolution of deposition rate and column angle as a function of the WO_3 target self-bias potential corroborates the predominance of the particle flux coming from the W target (Figure 5.11). Deposition rate slightly increases from 364 to 397 nm h^{-1} as U_{WO_3} rises from 100 to 300 V. In addition, the column angle is a little influenced by U_{WO_3} since it is reduced from 37 to 34 °. Similarly, an increase of U_{WO_3} favors the WO_3 target flux, which leads to a low rising of the total deposition rate.

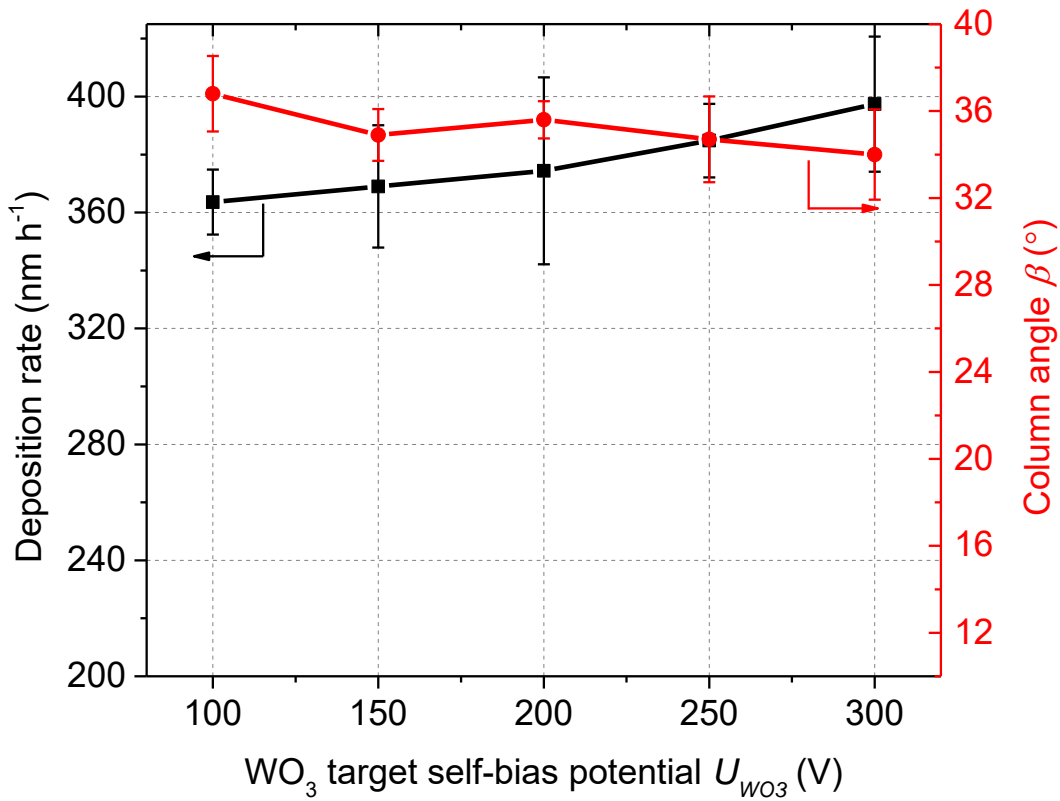


Figure 5.11 Deposition rate and column angle vs. WO_3 target self-bias potential. W target was DC sputtered with $I_w = 100$ mA. Deposition rate and column angle axes have the same scale as in Figure 5.7.

The crystallographic structure of these films prepared with various U_{WO_3} is significantly influenced as shown from X-ray diffraction patterns reported in Figure 5.12. For the lowest self-bias potential ($U_{WO_3} = 100$ V), peaks are mainly assigned to the pure W phase (pdf # 04-0806) with a (110) preferential orientation. Increasing U_{WO_3} gives rise to intense diffracted signals at $2\theta = 41.58^\circ$ and 47.20° corresponding to the (200) and (211) planes of the β -W phase (pdf # 65-6453), respectively. The (200) peak becomes more and more intense as U_{WO_3} increases, which correlates with an oxygen-enrichment of the films (β -phase formation is favored). Taking in to account the diffracted intensity of (200) phase of the β -W phase (pdf # 65-6453), the full width at half maximum (FWHM) does not show a clear evolution as a function of the WO_3 self-bias potential (inset in Figure 5.12). As a result, the crystal size is not significantly influenced by the WO_3 flux.

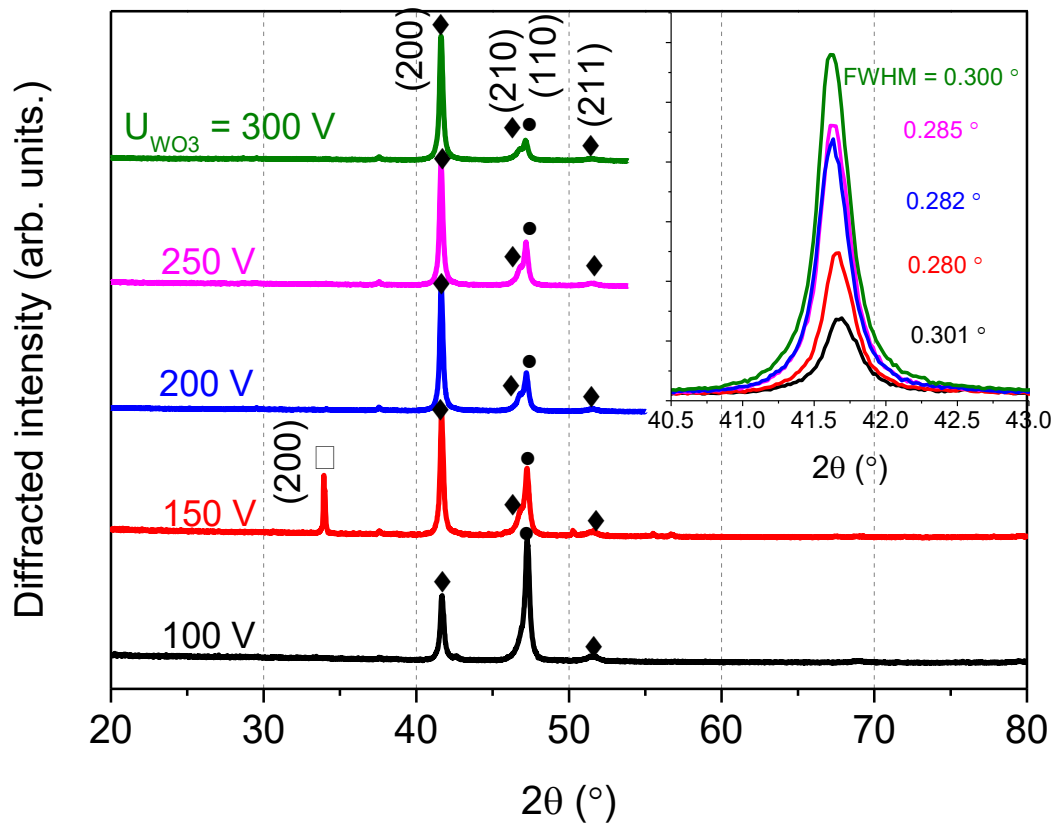


Figure 5.12 X-ray diffraction patterns of W-O thin films deposited on glass with various WO_3 target self-bias potentials and a constant W target current intensity. $I_W = 100$ mA; \bullet = W (pdf # 04-0806); \blacklozenge = β -W (pdf # 65-6453); \square = WO_{3-x} (pdf # 53-0434). Inset is a zoom of (200) peak at $2\theta = 41.58^\circ$. Full width at half-maximum (FWHM) is indicated.

It is also worth to notice that a shoulder appears close to the peak related to the (110) planes of the W-phase. Such a shoulder is linked to the occurrence of the β -W phase, i.e. (210) planes at $2\theta = 47.11^\circ$. For the films prepared with $U_{WO_3} = 150$ V and $I_W = 100$ mA, a diffracted signal is recorded at $2\theta = 33.96^\circ$ and is assigned to the WO_{3-x} phase (pdf # 53-0434). The occurrence of this WO_{3-x} phase still remains an open question.

b) Electrical properties

The same annealing treatment was applied to the films as before, i.e. annealing in air at 300°C for 12 hours. Figure 5.13 shows the evolution of electrical resistivity vs. time during this annealing. As U_{WO_3} increases, the samples become more resistive since more oxygen is introduced in the films. For all films, resistivity slightly increases after 12 hours annealing and remains in the order of $10^{-5} \Omega\text{ m}$.

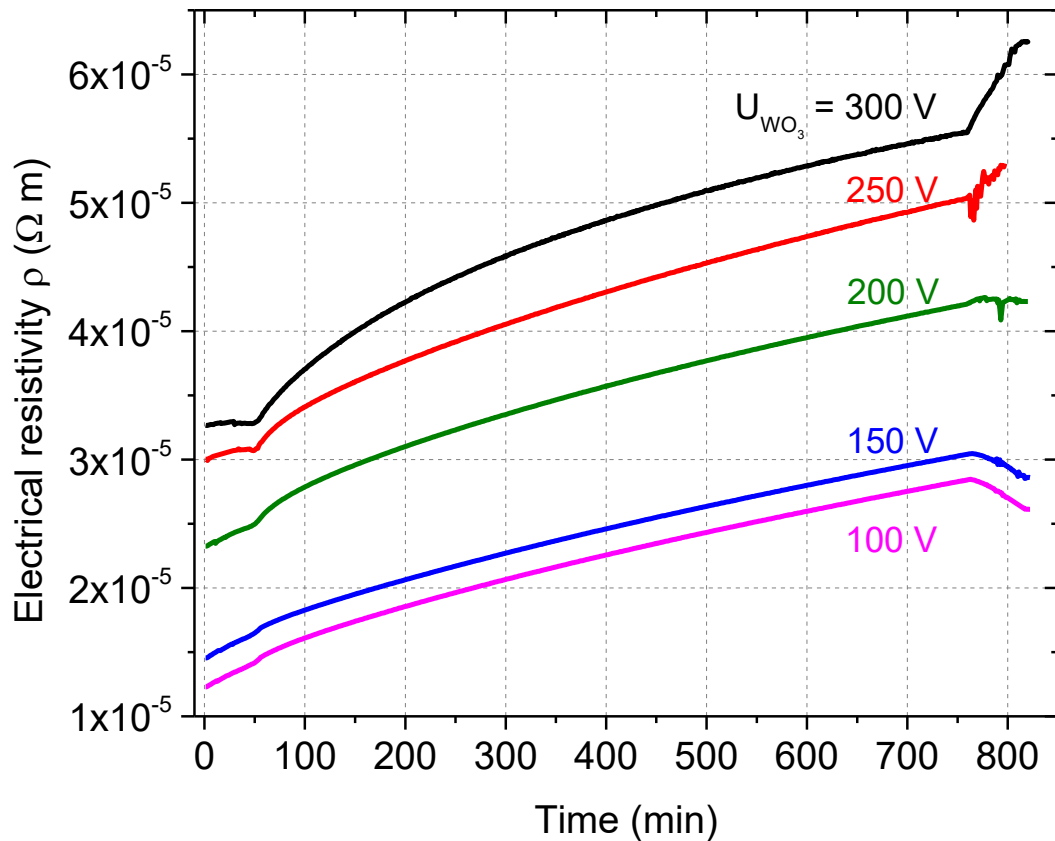


Figure 5.13 Electrical resistivity vs. time of W-O films prepared on glass substrates with various WO_3 target self-bias potentials and a constant W target current intensity $I_W = 100$ mA. Annealing was performed in air at 300 °C for 12 hours.

However, films deposited with $U_{WO_3} = 100$ and 150 V keep their metallic-like characteristic after the annealing treatment, whereas those obtained with $U_{WO_3} = 250$ and 300 V rather exhibit a semi-conducting-like behavior after 12 hours in air at 300 °C (from resistivity vs. time during the cooling stage, i.e. from 760 to 820 min). For the highest U_{WO_3} , films become oxygen-rich, which agrees with the β -W phase occurrence noticed from XRD results. We have to note that these films are too much conductive to be used as an active layer for gas sensing.

5.3. Conclusion

W-O thin films were reactively deposited by GLAD co-sputtering using two targets with a tilt angle of 80° to the substrate normal. At first, two W targets were DC sputtered. Despite a pulsing introduction of oxygen by RGPP using a ring for oxygen introduction close to one target, it was not possible to get the co-sputtering process maintaining one target in a metallic mode, whereas the other one was in reactive

mode in order to achieve tunable and original columnar architectures. Thus, WO₃ material was RF sputtered as the second target. By changing W target current intensity and WO₃ self-bias potential, inclined columnar microstructures were prepared with tunable columnar angles. Dense or porous architectures were produced with adjustable microstructures leading to nearly the same range of electrical resistivities (i.e. $\sim 10^{-5} \Omega \text{ m}$). Such resistivities are not suitable for gas sensing tests. An annealing post-deposition stage is thus necessary in order to reach the required range.

6. Chapter 5: Gas sensing performances

In the previous chapter, we presented how to develop an original way to get adjustable chemical compositions of WO_x thin films by means of the Reactive Gas Pulsing Process, namely RGPP. It was shown that we can gradually and precisely produce an accurate and progressive transition of WO_x film properties - from metal to semiconductor and finally to insulator – by using suitable deposition parameters of the RGPP technique. Such tunable WO_x films are now applied for the detection of dodecane vapor and the sensing performances are optimized in terms of response and recovery times, by simply taking into account the duty cycle parameter.

In order to produce nanostructured films, two combined strategies were implemented to play with microstructure and composition of sputter-deposited W-Os. The GLAD technique was developed so as to produce various architectures (inclined columns, zigzags, spirals) and similarly the Reactive Gas Pulsing Process, namely RGPP, was used for adjusting the oxygen concentration in the films and so, their electrical properties. The gas sensing performances of these W-O nanostructured films are now tested when separately exposed to dodecane vapor and ozone gas. We try to establish and discuss relationships between deposition parameters, architecture of W-O thin films and gas sensing performances.

We finally study GLAD co-sputtered W-O thin films as dodecane sensors. Inclined columnar structures are produced by tuning the co-sputtering conditions by means of two opposite and inclined W and WO_3 targets. Structure, morphology and electrical resistivity of the films are investigated, and an optimized series is prepared pulsing the oxygen gas during the growth to adjust the films composition and to tune the electrical properties. These W-O films are tested as dodecane sensors at operating temperatures ranging from 100 to 500 °C.

6.1. WO_x films with one W target

At first, the influence of the oxygen supply (duty cycle in RGPP) is considered on sensing performances of W-O thin films produced without GLAD. Afterwards, the nanostructuring by GLAD of W-O thin films are studied and applied as an active layer for gas sensor.

6.1.1 Role of oxygen

W-O films produced with duty cycles lower than 60 % of P did not produce any sensing behavior when exposed to dodecane vapor. It is mainly due to their metallic-like properties as previously shown in Figure 4.8. Oxygen content in the films is too low and duty cycles higher than 60 % of P are required to record some sensing responses as shown in Figure 6.1.

WO_x thin films sputter deposited with other duty cycles ($dc = 60, 80$ and 100 % of P) were tested by using the same sensing procedure, i.e. 10 to 300 ppm of dodecane injections for 90 s followed by 360 s of air exposure time. An annealing treatment in air (12 hours at 300 °C) was applied to W-O thin films before the sensing tests.

For $dc = 60$ % of P , WO_x are poorly sensitive to the dodecane injections since resistance changes are a few mΩ. In addition, the drift of the baseline as well as saturation at about 150 ppm are noticeable. These poor sensing performances agree with the metallic-like behavior previously noticed from optical (Figure 4.7) and electrical (Figure 4.8) characteristics of the films. On the other hand, WO_x films prepared with a continuous oxygen supply ($dc = 100$ % of P) exhibit an improved sensitivity to dodecane. The resistance change is negligible at 10 ppm but becomes significant at 50 and 100 ppm. However, the recovery time is longer than the sensor produced with $dc = 60$ % of P . The resistance increases when dodecane injection is stopped but never recovers its starting value. The baseline tends to be stabilized with time, but a saturation of the detection is once again close to 150 ppm.

The best sensing performances are finally achieved for films obtained with a duty cycle of 80 % of P . A very low drift of the baseline signal can be noticed after several dodecane injections. From resistance vs. time measurements, response and recovery times are improved compared to WO_x films fabricated with other duty cycles. Sensitivity of the sensor also seems to be enhanced and saturation is not reached

(higher than 300 ppm). It is interesting to note that these deposition conditions ($dc = 80\%$ of P) corresponds to the transition from sub- to over-stoichiometric WO_3 compounds (Figure 4.2).

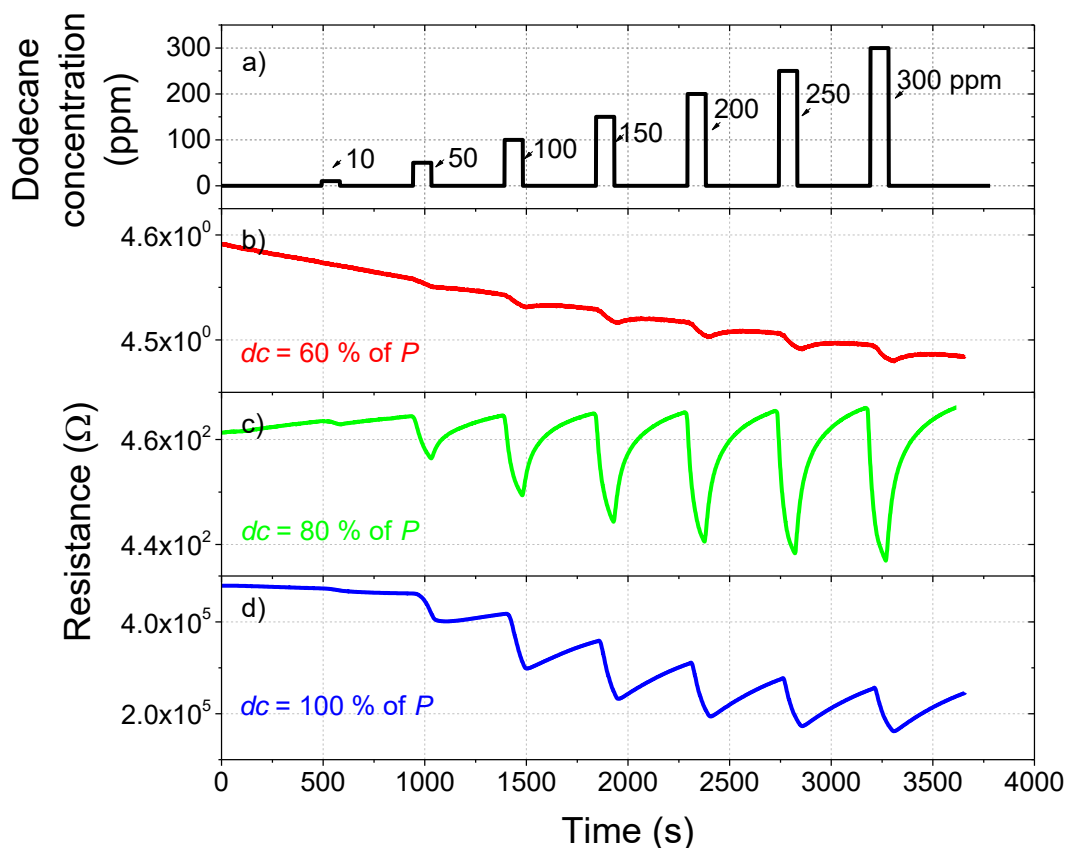


Figure 6.1 Resistance vs. time of WO_x sensors prepared with 3 different duty cycles ($dc = 60, 80$ and 100% of P). A growing dodecane concentration (10, 50 and up to 300 ppm, with a 50 ppm increment) was systematically used. Dodecane is injected for 90 s (injection time) and stopped for 360 s (air exposure time) with an operating temperature of 300 °C.

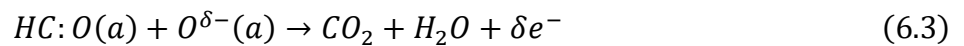
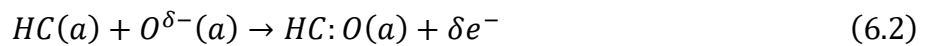
Oxygen vacancies as well as oxygen inserted in the films are both involved in the sensing mechanism. As a result, the adsorption-desorption phenomena on WO_x thin films surface remain an open question since for sub- and over-stoichiometric WO_3 thin films, dodecane is detected. However, one can suggest that for over-stoichiometric $WO_{3+\epsilon}$ compounds, some surface oxygen vacancies are created by the reaction of products from the decomposition of $C_{12}H_{26}$ with oxygen adsorbates and the resulting desorption of these reaction products (certainly CO_2 and H_2O). These surface oxygen vacancies created by the alkane decomposition can lead to the generation of W^{5+} centers. The additional electron associated with the resulting W^{5+} center favors the release of a free electron and gives rise to an increase of conductivity [113].

For sub-stoichiometric $WO_{3-\varepsilon}$ compounds, a mechanism involving interaction of charged surface oxygen species and the hydrocarbon molecules can be suggested taking into account Rout *et al.* investigations [114]. Assuming that hydrocarbon sensing by an oxygen-deficient WO_3 compound involves negative oxygen species O^- and O^{2-} , which are adsorbed on the film surface, these latter react with the hydrocarbon molecule to release an electron (CO_2 and H_2O gases are also produced) and finally decrease the resistivity.

The following reactions have been suggested by these authors [114]:



$O^{\delta-}(a)$ is a charged oxygen species adsorbed on the oxide surface. Hydrocarbons (HC) is first adsorbed on the oxide surface to give the $HC(a)$ species, which react with $O^{\delta-}(a)$ following:



These reactions release electrons leading to a decrease of the film's resistivity.

6.1.2 Exploiting the GLAD approach

It is well known that operating temperature of metal oxide material plays an important role on the sensing performances of resistive gas sensors because of the catalytic reactions involved during the detection process [115,116]. The influence of sensing material temperature has been studied measuring electrical responses of each selected chemical gas sensor under 300 ppm and 1 ppm of dodecane and ozone, respectively at different temperatures ranging from 50 to 500 °C. W-O thin films exhibiting dense, inclined, zigzag and spiral columnar microstructures, and sputter-deposited with various duty cycles were systematically tested as gas sensors. At first, it is worth noting that inclined and zigzag columnar structures gave rise to the best sensing performances towards dodecane and ozone environments. For these two kinds of structures, Figure 6.2a and b show the evolution of the gas sensor response *vs.* thin film temperature under dodecane and ozone, respectively and for duty cycles $dc = 30, 40$ and 50% of P . These measurements clearly show that the optimal temperature changes as a function of the architecture

and the nature of the chemical compound to detect. For a given temperature, the inclined structures systematically exhibit the best relative response. Zigzag structures tested with a temperature higher than 350°C did not produce a significant improvement of the sensing response. Such a temperature correlates with the crystallization of the films as previously reported from XRD analyses (Figure 4.14).

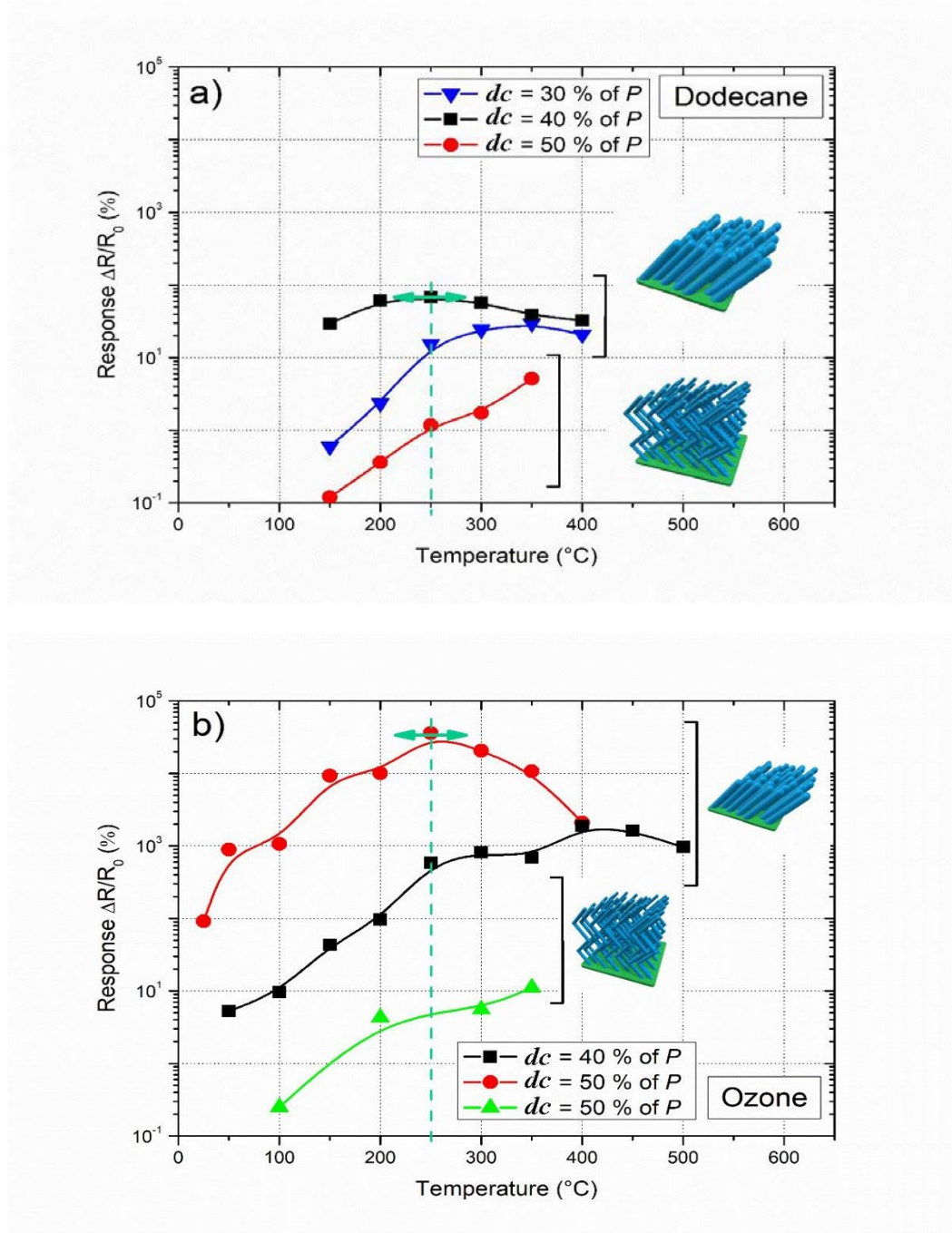


Figure 6.2 Responses of the W-O-based sensors to a) 300 ppm of dodecane and b) 1 ppm of ozone as a function of the temperature for inclined and zigzag architectures prepared with various duty cycles (only the optimized duty cycles and architectures are presented). The best sensing response is obtained at 250°C with dc = 40% of P and dc = 50% of P for dodecane and ozone, respectively (green dashed lines).

It is also interesting to note that heating zigzags and inclined structures at temperatures higher than 350°C led to a less defined architecture. Inclined columns and particularly zigzags become less distinct (film's densification), which is certainly connected to the lowest sensing performances at temperatures higher than 400°C. In addition, for both gaseous species tested with the inclined structures, the optimized sensing temperature ranges from 250 °C to 400 °C. As a result, the best responses are obtained for inclined structures at 250 °C with duty cycle $dc = 40\%$ of P and 50% of P for dodecane and ozone, respectively (green dashed lines in Figure 6.2a and b).

Figure 6.3 depicts the relationship established for each sensor prepared at their optimized duty cycle (dc in % of P) and tested at their optimized temperature (indicated in parentheses) between the pollutant response and the electrical resistance of the sensing film under synthetic air. The effect of duty cycle used to prepare dense films on their dodecane response is clearly shown. Such a duty cycle increases the electrical resistance of W-O coated platform and it has to be in the range 60-100% of P to get a significant response.

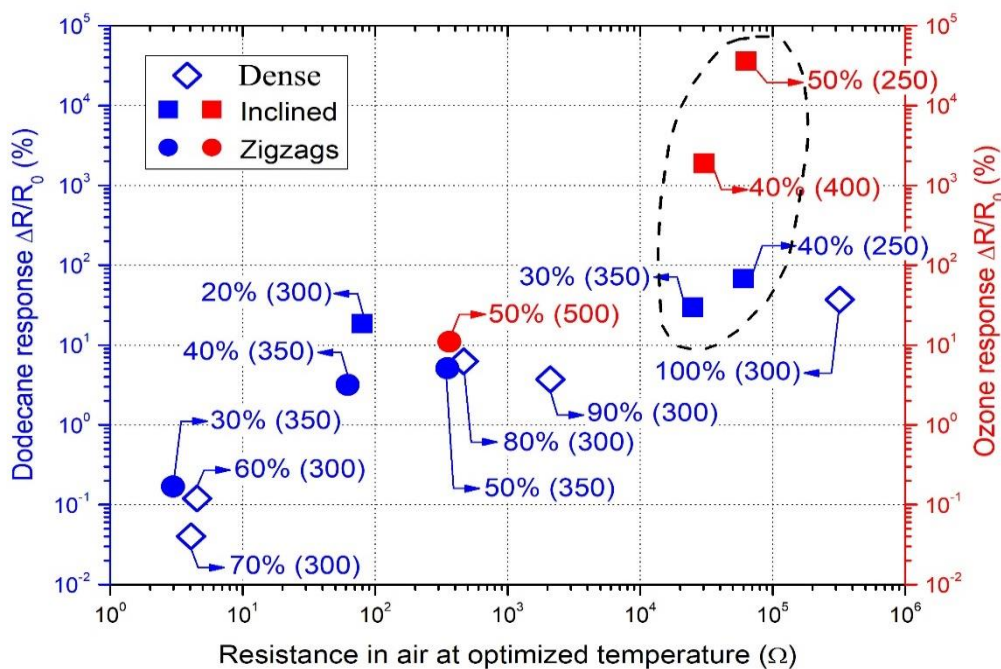


Figure 6.3 Dodecane and ozone responses vs. electrical resistance of W-O coated platform in air at the optimized temperature for films exhibiting normal, inclined and zigzag architectures. For each type of architecture, the duty cycle dc is indicated in % of the oxygen pulsing period P as well as the optimized temperature (in °C) in parentheses. The best response is systematically obtained for inclined columns as indicated by the dashed line.

The same trend is measured for inclined and zigzag structures tested with dodecane and ozone, i.e. a higher resistance and an improvement of the response as the duty cycle increases. This duty cycle effect is mainly connected to the oxygen vacancies in the films. Oxygen-deficient WO_3 compound is favored by reducing the duty cycle in the 60-80 % of P range [117]. Deviation from stoichiometry creates donor levels due to oxygen vacancies [101]. The increasing concentration of donor centers (as duty cycle reduces) leads to the formation of donor conduction band, which overlaps the conduction band and tends to exhibit metallic-like properties (i.e. free carrier concentration $> 10^{21} \text{ cm}^{-3}$). In addition, decreasing the oxygen concentration in sub-stoichiometric metallic oxide films enhances their reactivity and the film becomes more sensitive to an oxidized environment.

It is also interesting to note that the sensor responses improvement is in the following order: dense (normal sputtering), zigzags and inclined columns, which agrees with previous results reported in Figure 6.2. Clearly, sensors with a high resistance under synthetic air exhibit the best responses under dodecane or ozone. More specially, inclined columns prepared with duty cycles $dc = 40\%$ and 50% of P produce the highest response under dodecane and ozone, respectively in comparison with zigzags and normal structures. This is mainly assigned to the porous architecture (Figure 4.10 and Figure 4.12), which can be particularly emphasized in GLAD films with an inclined columnar structure [118]. In fact, inclined columns exhibit the most porous structure in comparison with the other ones [119], leading to a high quantity of chemisorbed gaseous species (reactive surface species) and a high permeability for the fast adsorption and gas diffusion. From these results, it can be concluded that the inclined columnar structures with duty cycles $dc = 40\%$ and 50% of P appear as the most efficient architectures for the detection of dodecane and ozone, respectively.

Repeatable test of W-O thin films gas sensor towards different concentrations of dodecane were also performed at an operating temperature of $250\text{ }^\circ\text{C}$ (Figure 6.4). Films exhibiting an inclined columnar microstructure and prepared with $dc = 40\%$ of P (i.e. the best dodecane response from results shown in Figure 6.3) were tested. Various concentrations (from 10 to 300 ppm) were applied 3 times for 90 s followed by 360 s of air exposure time. For the lowest concentrations (i.e. 10, 50 and 100 ppm), the

resistance systematically drifts. The response signal becomes more stable for dodecane concentrations higher than 150 ppm. It is also worth to remark that after 360 s of air exposure time, resistance never comes back to its original value, even for the lowest dodecane concentration. It leads to a significant drift of the baseline as clearly seen after 10 000 s of test. As a result, adsorption and desorption mechanisms of dodecane on tungsten oxide surfaces appear as complex process. Implementation of porous thin films produced by GLAD sputtering makes even more complicated understanding of sensing mechanisms and a whole area of work remains to be done in this respect.

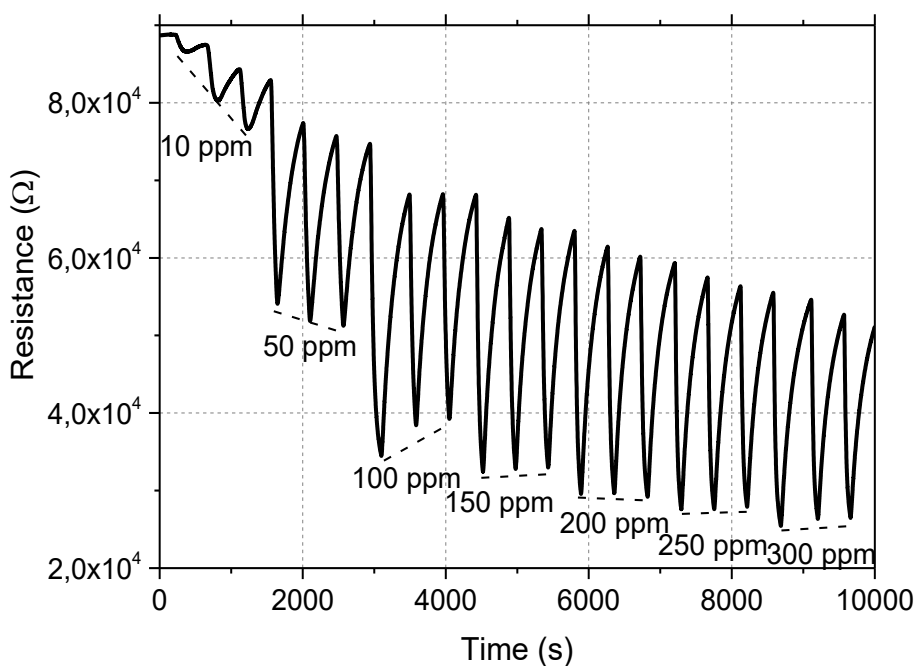


Figure 6.4 Resistance vs. time with different dodecane concentrations at 250°C of W-O thin films with an inclined columnar microstructure ($\alpha = 80^\circ$) prepared with duty cycle $dc = 40\%$ of P. Dodecane is injected for 90 s and stopped for 360 s. Each concentration is repeated 3 times.

For inclined columnar architectures, we systematically studied the influence of pollutant concentration on the gas sensor electrical responses at the optimized thin film temperature (250 °C). Figure 6.5a and b depict the real-time gas sensor response curves vs. time for various dodecane and ozone concentrations. Since WO_3 is an n-type semiconductor, the electrical resistance of the sensors decreases when exposed to dodecane (reducing compound) and increases when exposed to ozone (oxidizing compound).

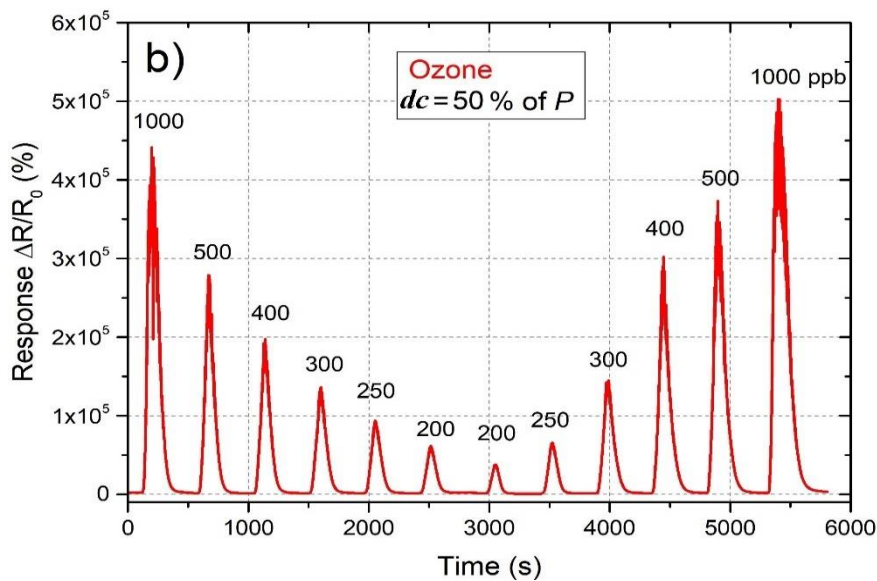
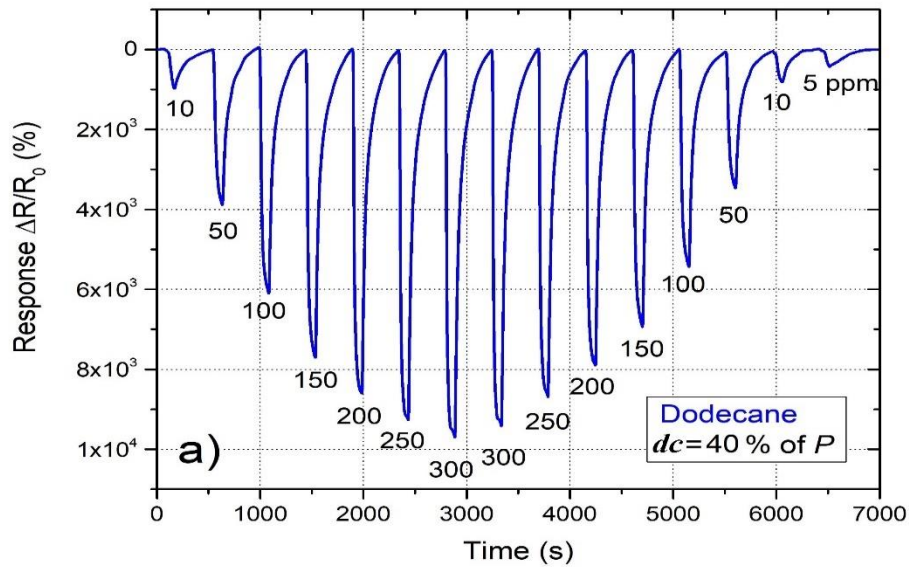


Figure 6.5 Normalized sensor responses (with a base line correction) at 250°C towards various gas concentrations of a) dodecane with duty cycle $dc = 40\%$ of P and b) ozone with duty cycle $dc = 50\%$ of P for W-O films exhibiting an inclined columnar architecture. Dodecane or ozone is injected for 90 s (injection) and stopped for 360 s (air exposure).

As expected, amplitudes of sensor electrical responses gradually decrease with decreasing dodecane or ozone concentration in synthetic air. It is also worth noticing that both sensors exhibited a poor repeatability over the time since the amplitude of the response for the same concentration is quite different. In addition, and especially for dodecane (Figure 6.5a), the response signal is still varying (back to the baseline is incomplete) when the next dodecane injection begins. At first, this phenomenon can

be explained by the operating temperature. Testing at 250 °C is too low to rapidly and completely desorb pollutant from the sensing surface. On the other hand, a relative short air exposure time (pollutant off = 360 s) is implemented between each pollutant exposition, which certainly leads to a non-total regeneration of activated sites. From Rout *et al.* [114] and Carotta *et al.* [120] investigations, one may suggest that the initial step of metal oxide sensor vs. alkane interactions consists of C-H bonds breaking and so, the formation of reactive alkyl radicals. Such radicals adsorb on the W-O surface with an oxidation of carbon (CO, CO₂) and generation of cracking sub-products, leading to poisoning of active sites.

For ozone, the sensor response becomes more stabilized at the end of the air exposure time (before the next ozone injection) since lower pollutant concentrations are involved (maximum of 1000 ppb or less). In addition, mechanisms of ozone sensor response would suggest a more efficient desorption phenomenon for ozone than dodecane for W-O active sites [121]. Similarly, a faster adsorption mechanism of ozone may also explain the highest response signals systematically measured when the pollutant is incrementally injected (from 3000 to 6000 s in Figure 6.5b) compared with those recorded as the ozone concentration is reduced (from 0 to 3000 s in Figure 6.5b). One may suggest the ozone adsorption mechanism on metal oxide surfaces by Ferrer and Somorjai [122] and continued by Labidi *et al.* [123]. The negatively charged ions adsorbed at the grain boundaries create a depletion layer in the n-type sample. This increases the bulk resistance and the grain boundary resistance by filling in the surface vacancies. The oxygen due to ozone adsorption also decreases the concentration of oxygen vacancies. Therefore, a decrease in the electron concentration is induced and thus an increase of the film's resistance.

Looking at the linear variation of the sensor responses during the first seconds of pollutant exposition (from Figure 6.5a and b), calculations of the slope value give information about the reactivity of each gas sensor under dodecane and ozone (as explained in Figure 3.7). The slopes of the W-O sensors were then measured and plotted as a function of the dodecane and ozone concentrations (Figure 6.6). The slope gradually increases as the pollutant concentration rises until a concentration close to 10 ppm and

300 ppb for dodecane and ozone, respectively. Above these concentrations, each gas sensor exhibits a smooth plateau, which is probably due to the rapid saturation of the W-O sensitive layer when increasing pollutant concentrations in the surrounding atmosphere of the gas sensor.

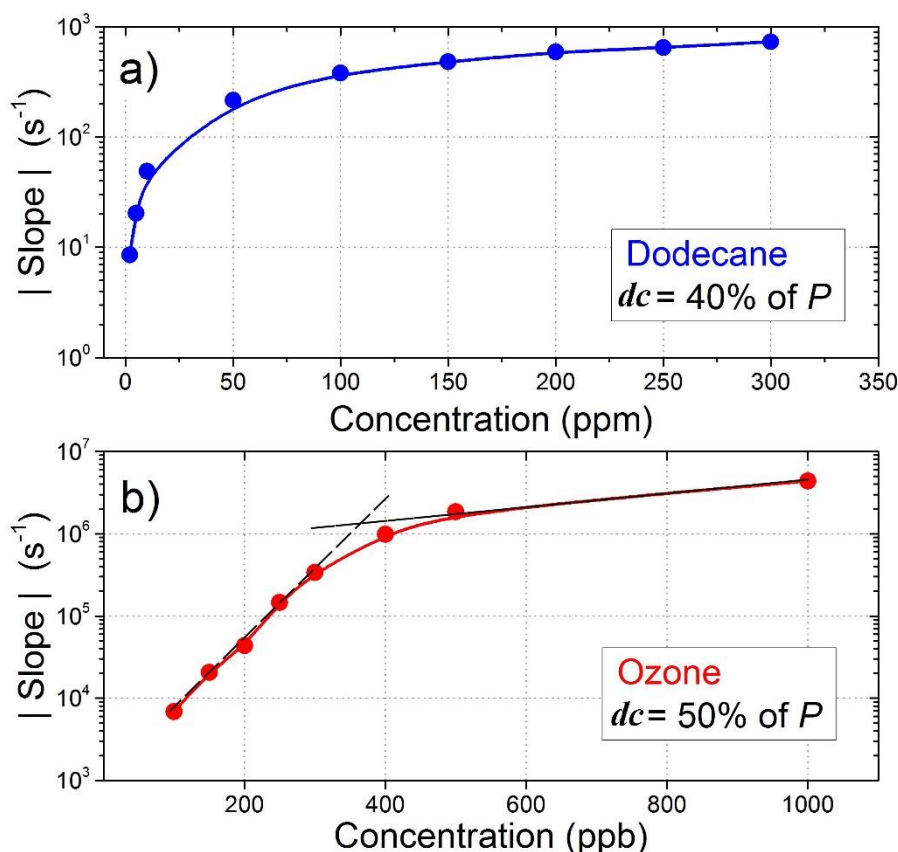


Figure 6.6 Absolute value of the slope as a function of the pollutant concentration calculated from the normalized sensor responses vs. time measurements (calculated as described in Figures 3.7 a and b) and data from Figure 6.5 when a) dodecane or b) ozone is injected. Duty cycle dc (% of pulsing period P) used for depositing W-O films is also indicated.

For dodecane, the $\log |\text{slope}|$ vs. concentration can be separated into 2 parts: below 20 ppm, and over 100 ppm. Below 20 ppm, the sensor sensitivity is the highest. A saturation state is reached for dodecane concentration higher than 100 ppm. Such a behavior has even been reported for the detection of hydrocarbon by metal oxide thin films [46,124]. This abrupt increase of sensitivity followed by a more or less defined saturation strongly depends on the number of carbon atoms in the targeted molecule [125]. Since the gas sensing mechanism is closely linked to the complex surface reactions of adsorbed dodecane and the sensing materials (among other parameters), no clear explanations can be proposed about this strong increase of slope for the lowest dodecane concentrations. Similarly, the ozone saturation becomes

significant close to 400 ppb. Interestingly, the slopes (in log scale) for concentrations from 100 to 300 ppb and from 400 to 1000 ppb could be well fitted into two linear curves with different slopes, respectively. The larger slope curve in the low concentration range (< 300 ppb) demonstrates a relatively high increase of the sensitivity (high-sensitive mode), whereas the sensitivity increases more slowly (low-sensitive mode) in the high concentration range (> 400 ppb). As the |slope| depends on resistance and thus conductivity of the film, which is the product of carrier concentration and carrier mobility, we may suggest that the switch from the high- to low-sensitive mode could be assigned to the reduced carrier mobility related to the scattering effects of adsorbed O₃ molecules [126]. Therefore, for low ozone concentrations (< 300 ppb), the reduction of carrier mobility could be negligible due to sparse O₃ molecular adsorption (high-resistive mode). When ozone concentration is high enough (low-resistive mode), carrier mobility decreases significantly due to abundant O₃ adsorption.

6.2. WO_x films with W and WO₃ co-sputtered targets

6.2.1 Annealing treatment before gas sensing

An annealing treatment in air was applied to W-O thin films prepared by GLAD co-sputtering. They were all heated for 12 hours in air at 300, 400, 450 and 500 °C. The sample were prepared with duty cycle $dc = 40\%$ of P , tungsten target current intensity $I_W = 100$ mA and WO₃ self-bias potential $U_{WO_3} = 100$ V. SEM observations of the cross-section and top view of the films show various morphologies as a function of the annealing temperature (Figure 6.7). Without annealing treatment, a typical columnar microstructure is clearly viewed (Figure 6.7a).

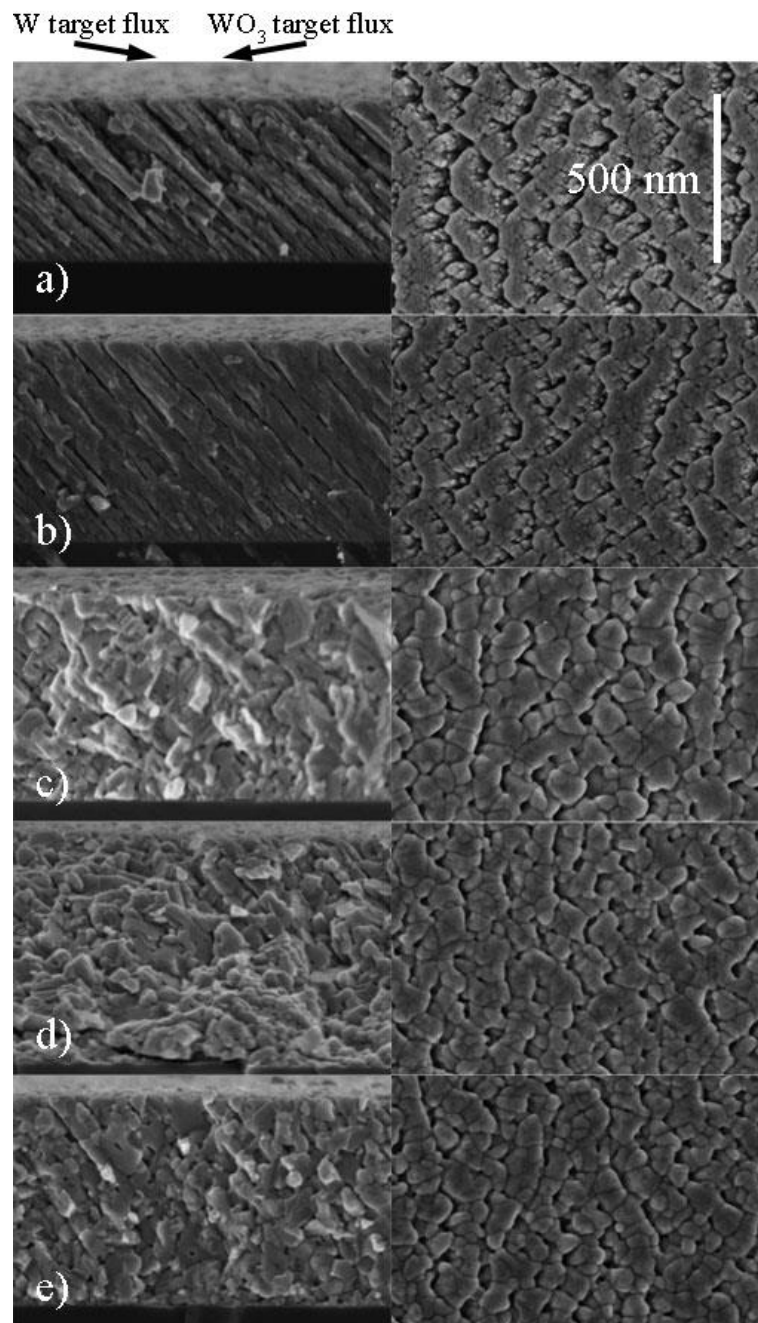


Figure 6.7 SEM views (cross-section and top) of W-O as-deposited films prepared with $I_w = 100$ mA, $U_{WO_3} = 100$ V, $dc = 40\%$ of P and after annealing in air for 12 hours at: a) room temperature, b) 300 °C, c) 400 °C, d) 450 °C and e) 500 °C.

From top and cross-section views, voids can be clearly seen between the columns. When the annealing temperature increases to 300 °C, columns become more aggregated and coalescent to form a more connected network grain growth (Figure 6.7b). Voids and spaces between columns remain but are less defined. From the cross-section view, columns begin to be destroyed while the annealing temperature is higher than 400 °C (Figure 6.7c). It becomes even worse while the annealing temperature reaches 450 °C (Figure 6.7d). At 500 °C, columns are still distinguishable but are rather formed by small crystalline

grains, and the column angle can be still observed. The column boundaries appear from the top view and voids are limited between the columns. It is worth noting that despite the annealing temperature higher than 450 °C, voids still exist. Columns are sintered and connected to each other. They form nano-necks, which may enhance the electron transport properties between the column boundaries.

X-ray diffraction patterns of co-sputtered W-O thin films show that the crystalline structure is also influenced by the annealing temperature (Figure 6.8). Two series of samples were co-sputter deposited. The first one corresponds to films prepared with duty cycle $dc = 40\%$ of P , tungsten target current intensity $I_W = 100$ mA and WO_3 self-bias potential $U_{WO_3} = 100$ V (Figure 6.8a). Such conditions produced inclined and narrow columns (Figure 5.10). The second one is related to films exhibiting a porous and anisotropic microstructure (i.e. large columns in the direction perpendicular to the W particle flux as shown in Figure 5.10). They were deposited with duty cycle $dc = 30\%$ of P , tungsten target current intensity $I_W = 100$ mA and WO_3 self-bias potential $U_{WO_3} = 300$ V. All films were annealed in the temperature range changing from 300 to 500 °C. Up to 300 °C, all samples exhibit a nearly amorphous structure. As the annealing temperature reaches 400 °C, clear diffracted signals are recorded for both series. Peaks are mainly assigned to WO_3 (pdf # 20-1324) and W_3O_8 (pdf # 65-1175) phase mixture. With a higher annealing temperature, a (001) strong preferential orientation of the WO_3 phase (pdf # 20-1324) is clearly recorded at $2\theta = 26.87^\circ$, as well as another peak at $2\theta = 27.37^\circ$ corresponding to the (001) planes of the W_3O_8 phase (pdf # 65-1175). In addition, weak but significant diffracted signals can also be noticed at $2\theta = 33.51$ and 37.80° , which are assigned to (320) and (330) planes of the sub-stoichiometric W_3O_8 phase (pdf # 65-1175), respectively. The peak is related to the SiO_2 phase coming from the glass substrate at high temperature annealing treatment.

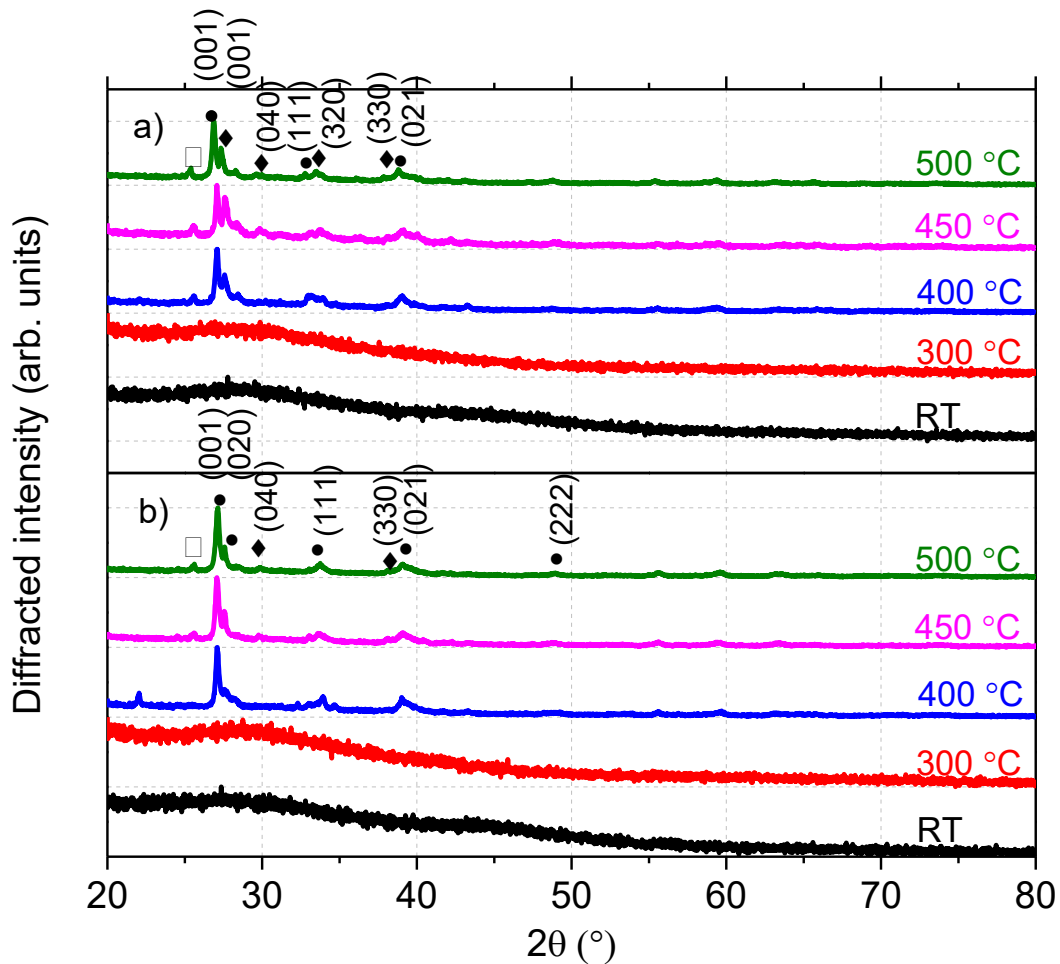


Figure 6.8 X-ray diffraction patterns of W-O co-sputtered thin films with different annealing temperatures. a) $I_W = 100$ mA, $U_{WO_3} = 100$ V and $dc = 40$ % of P, b) $I_W = 100$ mA, $U_{WO_3} = 300$ V and $dc = 30$ % of P; • = WO_3 (pdf # 20-1324); ◆ = W_3O_8 (pdf # 65-1175); ◻ = SiO_2 (pdf # 43-0745).

Three types of co-sputtered W-O thin films were annealed and followed by resistivity vs. measurements as reported in Figure 5.9 and Figure 5.13. These reactive sputtering conditions were performed for films exhibiting various and inclined columnar microstructures as shown in Figure 5.6 and for the two I_W extrema (i.e. the densest and the more voided). For the first series, the tungsten target current intensity was $I_W = 40$ mA and WO_3 self-bias potential was $U_{WO_3} = 300$ V. Using these deposition conditions, the column angle was nearly perpendicular to the substrate surface and a dense microstructure was observed (Figure 5.6). About the second series, the co-sputtering conditions were as follows: $I_W = 100$ mA and $U_{WO_3} = 100$ V (highest I_W and lowest U_{WO_3}), which produced inclined and narrow columns with a porous microstructure (Figure 5.10). For the third series, $I_W = 100$ mA and $U_{WO_3} = 300$ V (highest I_W and highest U_{WO_3}). The column angle was the highest ($\beta = 35^\circ$) and the SEM top view showed an anisotropic

microstructure (i.e. large columns in the direction perpendicular to the W particle flux as shown in Figure 5.10). However, the electrical resistivity of those 3 series are not suitable to be used as gas sensor ($\rho \sim 10^{-5} \Omega\text{m}$, which is less than one order of magnitude of the required range). The RGPP was used to inject oxygen flow rate during the co-sputtering process. The duty cycle was chosen in order to reach a resistivity range suitable for the gas sensing tests (i.e. $\rho \sim 10^{-4}$ to $10^{-2} \Omega\text{m}$). Afterward, all samples were annealed in air at 300 °C for 12 hours and the resistivity evolution vs. time was recorded as shown in Figure 6.9 (gas sensor aging process, as similarly applied for all sensors).

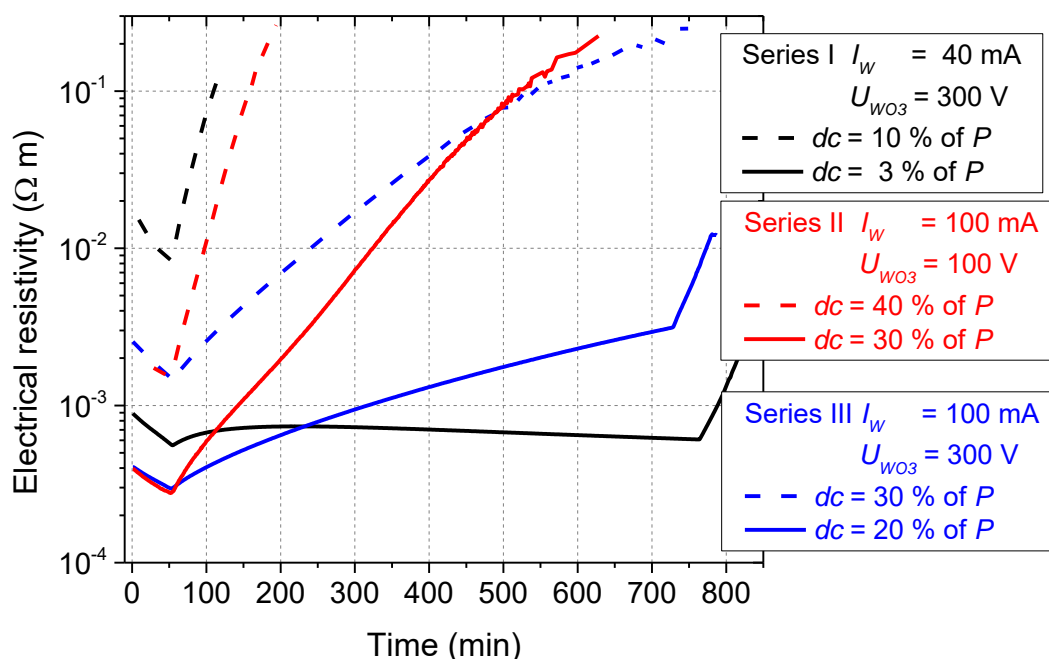


Figure 6.9 Electrical resistivity vs. time of some selected W-O films prepared on glass substrates and annealed in air at 300 °C for 12 hours.

As expected and for the same I_W and U_{WO_3} conditions, W-O films prepared with the highest duty cycle are the most resistive (dashed line in Figure 6.9). Such films are oxygen-rich compared to those deposited with the lowest duty cycle. As a result, they are very sensitive to the annealing time and become too much resistive to be measured with our system ($\rho > 10^{-1} \Omega\text{m}$). It is also worth to note that for the films prepared with $dc = 10\%$ of P , $I_W = 40\text{ mA}$ and $U_{WO_3} = 300\text{ V}$ (the most oxygen-rich sample), the resistivity is higher than $10^{-1} \Omega\text{m}$ only after 120 min, whereas those produced with $dc = 30\%$ of P , $I_W = 100\text{ mA}$ and $U_{WO_3} = 300\text{ V}$ (tungsten-rich) exhibit a resistivity $\rho = 2 \times 10^{-1} \Omega\text{m}$ after more than 700 min, despite its porous microstructure.

For a given series, decreasing the duty cycle reduces the resistivity drift *vs.* annealing time. It is particularly significant for films prepared with $dc = 20\%$ of P , $I_W = 100$ mA and $U_{WO_3} = 300$ V and even more marked when $dc = 3\%$ of P , $I_W = 40$ mA and $U_{WO_3} = 300$ V. For this latter, resistivity is nearly temperature invariant (slight reduction of resistivity after 720 min of annealing treatment). This quite stable resistivity evolution of the films co-sputtered with the highest U_{WO_3} and lowest I_W is directly linked to the densest microstructure. As previously discussed in § 4.2.3, this reduction of resistivity may be connected to the formation of metallic Magnéli phases in WO_x compounds. Last but not least, all these films are certainly incompletely oxidized after 12 hours in air at 300 °C, which probably contributes to the resistivity drift. However, and after this thermal treatment, the films resistivity remains in the suitable range for testing as gas sensors.

6.2.2 Sensing performances

After the process annealing in air for 12 hours at 300 °C, all WO_x thin films sputter-deposited according to the 3 series (i.e. different dc , I_W and U_{WO_3}) were tested as active layers for the dodecane detection. All the sensors were tested following the same procedure: a constant dodecane concentration (325 ppm) and measurements of the response *vs.* temperature every 50 °C from 100 to 500 °C (Figure 6.10). For temperatures lower than 350 °C, all sensors exhibit no response. The dodecane detection becomes significant for temperatures higher than 350 °C, except for films prepared with $I_W = 100$ mA, $U_{WO_3} = 300$ V and $dc = 30\%$ of P (biggest and widest columns from Figure 5.6) for which a response is clearly recorded from 200 °C.

For the other films, response becomes relevant when temperature reaches 450 °C and the best one is obtained for films prepared with $dc = 30\%$ of P . This operating temperature is higher than those recently reported by others [82,83,127] on the sensing properties of WO_3 nanorods produced by the GLAD method. However, it is important to remark that before testing our sensors, our annealing treatment is different, especially the involved temperature. Films were annealed in air for 12 hours at 300 °C, which is lower than the 400 to 500 °C typically reported [79] but this annealing treatment allows preserving the

columnar structure. As a result, crystallization, microstructure and oxygen vacancies in the films certainly change with the post-deposition thermal treatment. In addition, we focused on dodecane vapor detection for which a few investigations can be found in the literature [46,107] and detection mechanisms certainly differ from common gases such as NO₂, CO, O₃, among others. When the temperature is higher than 400 °C, the relevant kinetic parameters of adsorption or desorption phenomena between gas atoms and surface reaction sites increase, leading to a better response. The resistance in air (R₀) also decreases due to the high operating temperature, which consequently increases the response $\Delta R/R_0$.

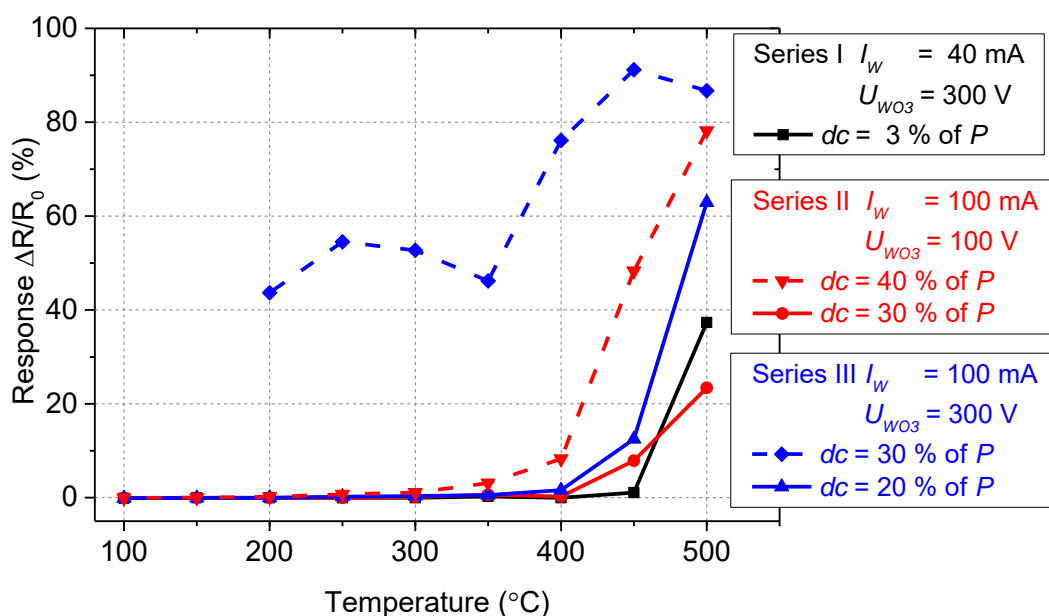


Figure 6.10 Sensor response vs. temperature for three series of W-O thin films GLAD co-sputtered, annealed 12 h in air at 300 °C and exposed to 325 ppm of dodecane for 90 s.

Dynamic responses of sensors at 500 °C when exposed to 325 ppm dodecane vapor for 90 s followed by 360 s air exposure time were measured for the same three groups of samples at 500 °C (Figure 6.11). Here again, the best performances are clearly obtained for films deposited with $dc = 30\%$ of P , tungsten target current intensity $I_W = 100$ mA and WO₃ self-bias potential $U_{WO_3} = 300$ V. Response is higher than 90 % and slightly drifts after a few cycles. The response time is also the best one for these films and saturation of $\Delta R/R_0$ clearly occurs at the end of all dodecane injections (i.e. after a few ten seconds of injection, $\Delta R/R_0$ is constant). Despite the incomplete dodecane desorption (steep and negative slope of

$\Delta R/R_0$ vs. time before the next dodecane injection), sensor remains sensitive to dodecane vapor. For the other films, response is in-between 20 – 80 %.

In addition, $\Delta R/R_0$ still drifts and increases after each dodecane injection, particularly for films sputtered with $dc = 30\%$ of P , $I_W = 100$ mA and $U_{WO_3} = 100$ V. It worth to notice that the influence of duty cycle on the sensors response is stronger than that of WO_3 self-bias potential. Films prepared with the lower duty cycles in series II (i.e. $dc = 30\%$ of P , $I_W = 100$ mA and $U_{WO_3} = 300$ V) exhibit the lowest sensing performances. With a slight increase of duty cycle (i.e. $dc = 40\%$ of P for these films), the sensing performance is among the highest with a response of about 80 %.

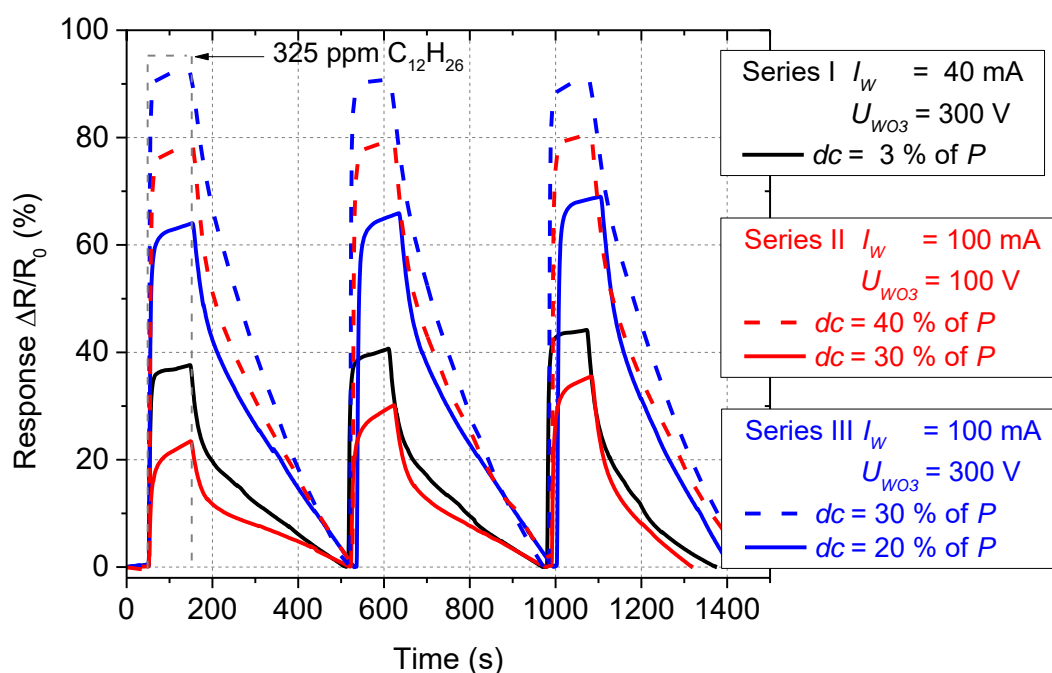


Figure 6.11 Sensor response vs. time of the 3 series of W-O thin films exposed to 325 ppm of dodecane for 90 s followed by 360 s of air exposure time at their own optimized temperature determined from Figure 6.10.

One can notice that the sensor prepared with $dc = 10\%$ of P , $I_W = 40$ mA and $U_{WO_3} = 300$ V, is too much resistivity to be tested, as shown in Figure 6.9. The most thermally stable sample (i.e. $dc = 3\%$ of P , $I_W = 40$ mA and $U_{WO_3} = 300$ V) does not exhibit the best performances, which can be explained by its quite dense microstructure as shown in Figure 5.6. We also have to highlight that the best dodecane sensing performances are connected to the high porous microstructure of W-O films sputter-deposited with $dc = 30\%$ of P (series III) combined with a relatively stable electrical resistivity after the annealing treatment (Figure 6.9).

6.3. Conclusion

W-O films prepared by RGPP with one W target and without GLAD, exhibited some sensing performances to dodecane vapor at 300 °C, mainly in terms of response and recovery time, for duty cycles in-between 60 – 100 % of P . The best performances were obtained for $dc = 80$ % of P , which is closely connected to the transition from sub- to overstoichiometric WO_3 compound.

For sensors obtained with films sputter-deposited using one W target and combining RGPP and GLAD processes, inclined columns, zigzag and spiral architectures were tested. Oxidizing and reducing chemical compounds were involved, namely dodecane and ozone. For both pollutants, the best sensing responses were obtained at 250 °C for W-O films prepared with an optimized duty cycle and showing tilted columns. These enhanced responses were mainly assigned to the high porous architecture, which is especially produced in GLAD films exhibiting an inclined columnar structure.

For GLAD co-sputtering thin films obtained from tilted W and WO_3 targets, some selected W-O films were used as sensitive layers for the detection of dodecane vapor. The best sensing responses were measured for films exhibiting the highest porous structure and quite stable electrical resistivity. Metal oxide thin films fabricated by the GLAD co-sputtering technique associated with the Reactive Gas Pulsing Process appears as a highly promising strategy and a large open field for gas sensing applications.

7. Conclusions and perspectives

The present work was based on the reactive sputter deposition of W-O thin films. Although W-O compounds have been abundantly investigated for these last decades, clear relationships between deposition conditions and fundamental material properties are often rather straight forward and partly well established in the literature. To tune the nature and the microstructure of WO_x films by means of new reactive sputtering processes still remains an exciting scientific motivation and the development of original strategies is always a pending task. To this aim, some attempts to modify W-O thin films properties have been performed following two approaches: the modification of the composition implementing the Reactive Gas Pulsing Process (RGPP) and the sculpturing of the films architecture at the micro- and/or nanoscale by means of the GLancing Angle Deposition (GLAD) technique.

At first, W-O thin films were successfully deposited by conventional reactive magnetron sputtering. W target was the starting material and oxygen gas was pulsed periodically by RGPP using a constant and short rectangular signal ($P = 16$ s), whereas the duty cycle dc was systematically changed from 0 to 100 % of P . Beyond the alternation of the process between the metallic and oxidized sputtering modes, a gradual evolution of the film properties was clearly achieved. The smooth transition from metal to semiconductor and finally insulator was possible by adjusting the duty cycle parameter by RGPP. The most interesting range was obtained for dc in-between 60-100 % of P corresponding to the transition from sub- to overstoichiometric WO_3 materials. Similarly, electrical and optical behaviors of thin films were largely tuned, and they produced the most interesting sensing performances for $dc = 80$ % of P when exposed to dodecane vapor as pollutant.

Combining GLAD and RGPP techniques, a large panel of compositions and architectures were produced in W-O thin films. Inclined columns with tilted angles up to 55° , zigzags with a periods number varying from 1 to 16, and spirals with a few pitches, were successfully grown. An accurate control of some geometrical characteristics such as column angle, zigzag number, etc. with an incremental change of duty cycle allowed a progressive evolution of optical properties: from absorbent, to semi-transparent and finally interferential compounds. A wide range of electrical resistivities (more than 5 orders of

magnitude) especially for films exhibiting an inclined columnar microstructure was also reached. This extended range of electrical properties was made possible mostly with the two key parameters: the incident angle α and the duty cycle dc . The first one gave rise to an enhanced thin films porosity (about 50 % of voids) and the second one led to play with the oxygen amount in the films. A suitable range of electrical resistivities was consequently defined in order to test these nanostructured W-O films as an active layer for gas sensors. Such a range strongly depends on the GLAD and RGPP key parameters, and the post-deposition annealing treatment as well.

The more complex GLAD co-sputtering process always associated with RGPP was finally developed. WO_3 target material was RF sputtered with a W target in DC mode. Both targets were inclined with a tilt angle of 80° compared to the substrate normal: the goal being to favor a growth competition between WO_3 and W fluxes in order to get tunable and original architectures. Playing with WO_3 self-bias potential and W target current intensity, columnar architectures were systematically prepared. The column angle could be modified from 11° to 37° as well as the columns width and thus, the resulting voided microstructure. A few films showing different morphologies were tested as gas sensors when exposed to dodecane. Some sensing performances were obtained for active layers exhibiting the most porous microstructure. Last but not least, the most interesting sensing responses were reached for W-O films sputter-deposited with one W target and associating GLAD and RGPP. Favoring the targeted range of films resistivity (between 10^{-4} to $10^{-2} \Omega m$) by means of a precise adjustment of the deposition parameters and the required annealing procedure, these nanostructured W-O films were applied as an active layer for reducing and oxidizing pollutants, namely dodecane and ozone. For both pollutants, the best sensing performances were obtained for films prepared with an optimized duty cycle ($dc = 40\%$ of P for dodecane and $dc = 50\%$ of P for ozone) and showing tilted columns. These improved responses were assigned to the high porous architecture, which is particularly produced in GLAD films with an inclined columnar microstructure. A drawback in the performance of these sensors was however brought to the fore by their relatively poor repeatability.

One of the first future works would be a focus on creating even more porous microstructures taking advantage of the GLAD co-sputtering process. By co-deposition of more or less miscible metals (e.g. W-Cu, Mo-Cu or even Sn-Cu), some original bicomponent columnar films could be achieved (e.g. Janus-like columns). Removing one material by chemical etching to further improve the surface-to-volume ratio of the films and with a post-thermal oxidation treatment to get the sensitive metal oxide compounds (e.g. WO_x , SnO_y , etc.), the sensing behaviors should surely be improved with deeper investigations focused on all sensing performances (sensitivity, response and recovery time and so on). Another attractive prospect would be the doping of binary metal oxide films (e.g. Me: WO_3 , Me: SnO_2 , etc.) or the possibility to get ternary oxides exhibiting inclined columns and thus, a porous microstructure. The choice of metals and their thermal stability to normal environment would obviously remain a challenging task to manage and understand, in correlation with their electronic transport properties. Finally, the open and porous microstructure associated with GLAD films make them very exciting candidates not only for sensing applications, but also for other micro and/or nano systems. This strong advantage makes them a strategic tool for integrating into a wide range of sensing and analytical devices.

8. References

- [1] S.H.G. Teo, A.Q. Liu, J. Singh, M.B. Yu, Hole-type two-dimensional photonic crystal fabricated in silicon on insulator wafers, *Sensors and Actuators A: Physical*. 133 (2007) 388–394. doi:10.1016/j.sna.2006.06.030.
- [2] M. Liu, X. Li, S.K. Karuturi, A.I.Y. Tok, H.J. Fan, Atomic layer deposition for nanofabrication and interface engineering, *Nanoscale*. 4 (2012) 1522. doi:10.1039/c2nr11875k.
- [3] A. Cacucci, S. Loffredo, V. Potin, L. Imhoff, N. Martin, Interdependence of structural and electrical properties in tantalum/tantalum oxide multilayers, *Surface and Coatings Technology*. 227 (2013) 38–41. doi:10.1016/j.surfcoat.2012.10.064.
- [4] Y. Teng, Y. Fu, L. Xu, B. Lin, Z. Wang, Z. Xu, L. Jin, W. Zhang, Three-dimensional ordered macroporous (3DOM) composite for electrochemical study on acetylcholinesterase inhibition induced by endogenous neurotoxin, *The Journal of Physical Chemistry B*. 116 (2012) 11180–11186. doi:10.1021/jp302792u.
- [5] M.O. Jensen, M.J. Brett, Square spiral 3D photonic bandgap crystals at telecommunications frequencies, *Optics Express*. 13 (2005) 3348. doi:10.1364/OPEX.13.003348.
- [6] K.J. Choi, H.W. Jang, One-dimensional oxide nanostructures as gas-sensing materials: Review and issues, *Sensors*. 10 (2010) 4083–4099. doi:10.3390/s100404083.
- [7] Y. Li, T. Kunitake, S. Fujikawa, Efficient fabrication and enhanced photocatalytic activities of 3D-ordered films of titania hollow spheres, *The Journal of Physical Chemistry B*. 110 (2006) 13000–13004. doi:10.1021/jp061979z.
- [8] X. Zhang, H. Su, X. Yang, Catalytic performance of a three-dimensionally ordered macroporous Co/ZrO₂ catalyst in Fischer–Tropsch synthesis, *Journal of Molecular Catalysis A: Chemical*. 360 (2012) 16–25. doi:10.1016/j.molcata.2012.03.024.
- [9] L. Yang, D. Ge, J. Zhao, Y. Ding, X. Kong, Y. Li, Improved electrochromic performance of ordered macroporous tungsten oxide films for IR electrochromic device, *Solar Energy Materials and Solar Cells*. 100 (2012) 251–257. doi:10.1016/j.solmat.2012.01.028.
- [10] M. Fenker, H. Kappl, C.S. Sandu, Precise control of multilayered structures of Nb-O-N thin films by the use of reactive gas pulsing process in DC magnetron sputtering, *Surface and Coatings Technology*. 202 (2008) 2358–2362. doi:10.1016/j.surfcoat.2007.08.007.
- [11] D. Depla, S. Mahieu, R. De Gryse, Depositing aluminium oxide: A Case study of reactive magnetron sputtering, in: *Reactive sputter deposition, 2008*: pp. 153–197. doi:10.1007/978-3-540-76664-3_5.
- [12] I. Safi, Recent aspects concerning DC reactive magnetron sputtering of thin films: A review, *Surface and Coatings Technology*. 127 (2000) 203–219. doi:10.1016/S0257-8972(00)00566-1.
- [13] J. Musil, P. Baroch, J. Vlček, K.H. Nam, J.G. Han, Reactive magnetron sputtering of thin films: Present status and trends, *Thin Solid Films*. 475 (2005) 208–218. doi:10.1016/j.tsf.2004.07.041.
- [14] J.F. Pierson, D. Wiederkehr, A. Billard, Reactive magnetron sputtering of copper, silver, and gold, *Thin Solid Films*. 478 (2005) 196–205. doi:10.1016/j.tsf.2004.10.043.
- [15] W.D. Sproul, Reactive sputter deposition of polycrystalline nitride and oxide superlattice coatings, *Surface and Coatings Technology*. 86–87 (1996) 170–176. doi:10.1016/S0257-8972(96)02977-5.
- [16] S.B. Kulkarni, A.T. Mane, S.T. Navale, P.S. Kulkarni, R.N. Mulik, V.B. Patil, Synthesis, structural, compositional, morphological and optoelectronic properties of tungsten oxide thin films, *Journal of Materials Science: Materials in Electronics*. 26 (2015) 1087–1096. doi:10.1007/s10854-014-2508-8.
- [17] C. Li, J.H. Hsieh, M.-T. Hung, B.Q. Huang, The deposition and microstructure of amorphous tungsten oxide films by sputtering, *Vacuum*. 118 (2015) 125–132. doi:10.1016/j.vacuum.2015.01.020.
- [18] G.A. Niklasson, C.G. Granqvist, Electrochromics for smart windows: Thin films of tungsten oxide and nickel oxide, and devices based on these, *J. Mater. Chem*. 17 (2007) 127–156. doi:10.1039/B612174H.

- [19] C.G. Granqvist, Electrochromic tungsten oxide films: Review of progress 1993-1998, *Solar Energy Materials and Solar Cells*. 60 (2000) 201–262. doi:10.1016/S0927-0248(99)00088-4.
- [20] Y.S. Kim, S.-C. Ha, K. Kim, H. Yang, S.-Y. Choi, Y.T. Kim, J.T. Park, C.H. Lee, J. Choi, J. Paek, K. Lee, Room-temperature semiconductor gas sensor based on nonstoichiometric tungsten oxide nanorod film, *Applied Physics Letters*. 86 (2005) 213105. doi:10.1063/1.1929872.
- [21] C.V. Ramana, S. Utsunomiya, R.C. Ewing, C.M. Julien, U. Becker, Structural stability and phase transitions in WO_3 thin films, *The Journal of Physical Chemistry B*. 110 (2006) 10430–10435. doi:10.1021/jp056664i.
- [22] M.B. Johansson, B. Zietz, G.A. Niklasson, L. Österlund, Optical properties of nanocrystalline WO_3 and WO_{3-x} thin films prepared by DC magnetron sputtering, *Journal of Applied Physics*. 115 (2014) 213510. doi:10.1063/1.4880162.
- [23] K.J. Patel, C.J. Panchal, V.A. Kheraj, M.S. Desai, Growth, structural, electrical and optical properties of the thermally evaporated tungsten trioxide (WO_3) thin films, *Materials Chemistry and Physics*. 114 (2009) 475–478. doi:10.1016/j.matchemphys.2008.09.071.
- [24] D. Depla, S. Heirwegh, S. Mahieu, J. Haemers, R. De Gryse, Understanding the discharge voltage behavior during reactive sputtering of oxides, *Journal of Applied Physics*. 101 (2007) 13301. doi:10.1063/1.2404583.
- [25] W.D. Sproul, P.J. Rudnik, C.A. Gogol, R.A. Mueller, Advances in partial-pressure control applied to reactive sputtering, *Surface and Coatings Technology*. 39–40 (1989) 499–506. doi:10.1016/S0257-8972(89)80011-8.
- [26] A.F. Hmiel, Partial pressure control of reactively sputtered titanium nitride, *Journal of Vacuum Science & Technology A: Vacuum, Surfaces, and Films*. 3 (1985) 592–595. doi:10.1116/1.572957.
- [27] S. Kadlec, J. Musil, H. Vyskocil, Hysteresis effect in reactive sputtering: A problem of system stability, *Journal of Physics D: Applied Physics*. 19 (1986) 187–190.
- [28] N. Martin, A.R. Bally, P. Hones, R. Sanjinés, F. Lévy, High rate and process control of reactive sputtering by gas pulsing: the Ti–O system, *Thin Solid Films*. 377–378 (2000) 550–556. doi:10.1016/S0040-6090(00)01440-1.
- [29] N. Martin, O. Banakh, A.M.E. Santo, S. Springer, R. Sanjinès, J. Takadoum, F. Lévy, Correlation between processing and properties of TiO_xN_y thin films sputter deposited by the reactive gas pulsing technique, *Applied Surface Science*. 185 (2001) 123–133. doi:10.1016/S0169-4332(01)00774-7.
- [30] O. Banakh, T. Heulin, P.E. Schmid, H. Le Dréo, I. Tkalcec, F. Lévy, P.-A. Steinmann, Influence of process parameters on the properties of the tantalum oxynitride thin films deposited by pulsing reactive gas sputtering, *Journal of Vacuum Science & Technology A: Vacuum, Surfaces, and Films*. 24 (2006) 328–333. doi:10.1116/1.2172946.
- [31] M. Grafouté, C. Petitjean, A. Diama, J.F. Pierson, J.M. Greneche, C. Rousselot, Structural investigations of iron oxynitride multilayered films obtained by reactive gas pulsing process, *Surface and Coatings Technology*. 272 (2015) 158–164. doi:10.1016/j.surfcoat.2015.04.010.
- [32] P. Carvalho, L. Cunha, E. Alves, N. Martin, E. Le Bourhis, F. Vaz, ZrO_xN_y decorative thin films prepared by the reactive gas pulsing process, *Journal of Physics D: Applied Physics*. 42 (2009) 195501. doi:10.1088/0022-3727/42/19/195501.
- [33] N.M.G. Parreira, T. Polcar, A. Cavaleiro, Characterization of W–O coatings deposited by magnetron sputtering with reactive gas pulsing, *Surface and Coatings Technology*. 201 (2007) 5481–5486. doi:10.1016/j.surfcoat.2006.07.017.
- [34] J.-M. Chappé, N. Martin, J. Lintymer, F. Sthl, G. Terwagne, J. Takadoum, Titanium oxynitride thin films sputter deposited by the reactive gas pulsing process, *Applied Surface Science*. 253 (2007) 5312–5316. doi:10.1016/j.apsusc.2006.12.004.
- [35] K. Robbie, M.J. Brett, A. Lakhtakia, Chiral sculptured thin films, *Nature*. 384 (1996) 616.
- [36] R.N. Tait, T. Smy, M.J. Brett, Modelling and characterization of columnar growth in evaporated films, *Thin Solid Films*. 226 (1993) 196–201. doi:10.1016/0040-6090(93)90378-3.

- [37] A. Boudiba, P. Roussel, C. Zhang, M.-G. Olivier, R. Snyders, M. Debliquy, Sensing mechanism of hydrogen sensors based on palladium-loaded tungsten oxide (Pd-WO₃), *Sensors and Actuators B: Chemical*. 187 (2013) 84–93. doi:10.1016/j.snb.2012.09.063.
- [38] M. Usta, S. Kahraman, F. Bayansal, H.A. Çetinkara, Effects of annealing on morphological, structural and electrical properties of thermally evaporated WO₃ thin films, *Superlattices and Microstructures*. 52 (2012) 326–335. doi:10.1016/j.spmi.2012.05.008.
- [39] R.F. Garcia-Sanchez, T. Ahmido, D. Casimir, S. Baliga, P. Misra, Thermal effects associated with the Raman spectroscopy of WO₃ gas-sensor materials, *The Journal of Physical Chemistry. A*. 117 (2013) 13825–31. doi:10.1021/jp408303p.
- [40] T. Stoycheva, F.E. Annanouch, I. Gràcia, E. Llobet, C. Blackman, X. Correig, S. Vallejos, Micromachined gas sensors based on tungsten oxide nanoneedles directly integrated via aerosol assisted CVD, *Sensors and Actuators B: Chemical*. 198 (2014) 210–218. doi:10.1016/j.snb.2014.03.040.
- [41] J. Guérin, M. Bendahan, K. Aguir, A dynamic response model for the WO₃-based ozone sensors, *Sensors and Actuators B: Chemical*. 128 (2008) 462–467. doi:10.1016/j.snb.2007.07.010.
- [42] W. Belkacem, A. Labidi, J. Guérin, N. Mliki, K. Aguir, Cobalt nanograins effect on the ozone detection by WO₃ sensors, *Sensors and Actuators B: Chemical*. 132 (2008) 196–201. doi:10.1016/j.snb.2008.01.023.
- [43] R. Boulmani, M. Bendahan, C. Lambert-Mauriat, M. Gillet, K. Aguir, Correlation between rf-sputtering parameters and WO₃ sensor response towards ozone, *Sensors and Actuators B: Chemical*. 125 (2007) 622–627. doi:10.1016/j.snb.2007.03.011.
- [44] A. Labidi, M. Gaidi, J. Guérin, A. Bejaoui, M. Maaref, K. Aguir, Alternating current investigation and modeling of the temperature and ozone effects on the grains and the grain boundary contributions to the WO₃ sensor responses, *Thin Solid Films*. 518 (2009) 355–361. doi:10.1016/j.tsf.2009.06.034.
- [45] X. You, F.N. Egolopoulos, H. Wang, Detailed and simplified kinetic models of n-dodecane oxidation: The role of fuel cracking in aliphatic hydrocarbon combustion, *Proceedings of the Combustion Institute*. 32 I (2009) 403–410. doi:10.1016/j.proci.2008.06.041.
- [46] M.A.P. Yazdi, N. Martin, E. Monsifrot, P. Briois, A. Billard, ZnO nano-tree active layer as heavy hydrocarbon sensor: From material synthesis to electrical and gas sensing properties, *Thin Solid Films*. 596 (2015) 128–134. doi:10.1016/j.tsf.2015.08.065.
- [47] H.A. Wriedt, The OW (oxygen-tungsten) system, *Journal of Phase Equilibria*. 10 (1989) 368–384.
- [48] Y. Zhao, S. Zhang, G. Zhang, X. Deng, C. Xie, Highly sensitive porous metal oxide films for early detection of electrical fire: Surface modification and high throughput screening, *Sensors and Actuators B: Chemical*. 191 (2014) 431–437. doi:10.1016/j.snb.2013.09.111.
- [49] A.T. Mane, S.B. Kulkarni, S.T. Navale, A.A. Ghanwat, N.M. Shinde, J. Kim, V.B. Patil, NO₂ sensing properties of nanostructured tungsten oxide thin films, *Ceramics International*. 40 (2014) 16495–16502. doi:10.1016/j.ceramint.2014.08.001.
- [50] E. Çiftyürek, K. Sabolsky, E.M. Sabolsky, Molybdenum and tungsten oxide based gas sensors for high temperature detection of environmentally hazardous sulfur species, *Sensors and Actuators, B: Chemical*. 237 (2016) 262–274. doi:10.1016/j.snb.2016.06.071.
- [51] M. Zhao, M.H. Wong, J.X. Huang, C.W. Ong, Ultrathin percolated WO₃ cluster film and its resistive response to H₂, *Journal of Alloys and Compounds*. 612 (2014) 163–169. doi:10.1016/j.jallcom.2014.05.108.
- [52] F. Tian, L. Zhao, X.-Y. Xue, Y. Shen, X. Jia, S. Chen, Z. Wang, DFT study of CO sensing mechanism on hexagonal WO₃ (001) surface: The role of oxygen vacancy, *Applied Surface Science*. 311 (2014) 362–368. doi:10.1016/j.apsusc.2014.05.069.
- [53] T.A. Ho, T.-S. Jun, Y.S. Kim, Material and NH₃-sensing properties of polypyrrole-coated tungsten oxide nanofibers, *Sensors and Actuators B: Chemical*. 185 (2013) 523–529.

doi:10.1016/j.snb.2013.05.039.

- [54] S. Shukla, S. Chaudhary, A. Umar, G.R. Chaudhary, S.K. Mehta, Tungsten oxide (WO_3) nanoparticles as scaffold for the fabrication of hydrazine chemical sensor, *Sensors and Actuators B: Chemical*. 196 (2014) 231–237. doi:10.1016/j.snb.2014.02.016.
- [55] X. Chi, C. Liu, L. Liu, Y. Li, Z. Wang, X. Bo, L. Liu, C. Su, Tungsten trioxide nanotubes with high sensitive and selective properties to acetone, *Sensors and Actuators B: Chemical*. 194 (2014) 33–37. doi:10.1016/j.snb.2013.12.078.
- [56] M. Zhao, J. Huang, C.-W. Ong, Preparation and structure dependence of H_2 sensing properties of palladium-coated tungsten oxide films, *Sensors and Actuators B: Chemical*. 177 (2013) 1062–1070. doi:10.1016/j.snb.2012.12.011.
- [57] H.G. Moon, S.D. Han, M.-G. Kang, W. Jung, B. Kwon, C. Kim, T. Lee, S. Lee, S. Baek, J. Kim, H. Park, C. Kang, Glancing angle deposited WO_3 nanostructures for enhanced sensitivity and selectivity to NO_2 in gas mixture, *Sensors and Actuators B: Chemical*. 229 (2016) 92–99. doi:10.1016/j.snb.2016.01.084.
- [58] N.D. Hoa, N. Van Duy, N. Van Hieu, Crystalline mesoporous tungsten oxide nanoplate monoliths synthesized by directed soft template method for highly sensitive NO_2 gas sensor applications, *Materials Research Bulletin*. 48 (2013) 440–448. doi:10.1016/j.materresbull.2012.10.047.
- [59] J. Yu, H. Wen, M. Shafiei, M.R. Field, Z.F. Liu, W. Wlodarski, N. Motta, Y.X. Li, K. Kalantar-zadeh, P.T. Lai, A hydrogen/methane sensor based on niobium tungsten oxide nanorods synthesised by hydrothermal method, *Sensors and Actuators B: Chemical*. 184 (2013) 118–129. doi:10.1016/j.snb.2013.03.135.
- [60] N.M. Vuong, D. Kim, H. Kim, Surface gas sensing kinetics of a WO_3 nanowire sensor: Part 1 - oxidizing gases, *Sensors and Actuators B: Chemical*. 220 (2015) 932–941. doi:10.1016/j.snb.2015.06.031.
- [61] Y. Qin, W. Xie, Y. Liu, Z. Ye, Thermal-oxidative growth of aligned $\text{W}_{18}\text{O}_{49}$ nanowire arrays for high performance gas sensor, *Sensors and Actuators B: Chemical*. 223 (2016) 487–495. doi:10.1016/j.snb.2015.09.113.
- [62] A. Maity, A. Ghosh, S.B. Majumder, Understanding the anomalous conduction behavior in “n” type tungsten oxide thin film during hydrogen gas sensing: Kinetic analyses of conductance transients, *Sensors and Actuators, B: Chemical*. 220 (2015) 949–957. doi:10.1016/j.snb.2015.06.038.
- [63] Y. Qin, C. Liu, M. Liu, Y. Liu, Nanowire (nanorod) arrays-constructed tungsten oxide hierarchical structure and its unique NO_2 -sensing performances, *Journal of Alloys and Compounds*. 615 (2014) 616–623. doi:10.1016/j.jallcom.2014.07.080.
- [64] W. Zeng, Y. Li, B. Miao, K. Pan, Hydrothermal synthesis and gas sensing properties of $\text{WO}_3\text{H}_2\text{O}$ with different morphologies, *Physica E: Low-Dimensional Systems and Nanostructures*. 56 (2014) 183–188. doi:10.1016/j.physe.2013.09.005.
- [65] D. Susanti, A.S. Perdana, H. Purwaningsih, L. Noerochim, G.E. Kusuma, Preparation of CO gas sensor from WO_3 nanomaterial synthesized via sol-gel method followed by hydrothermal process, in: *5th Nanoscience and Nanotechnology Symposium, 2014*: pp. 14–19. doi:10.1063/1.4866722.
- [66] H. Zhang, Z. Liu, J. Yang, W. Guo, L. Zhu, W. Zheng, Temperature and acidity effects on WO_3 nanostructures and gas-sensing properties of WO_3 nanoplates, *Materials Research Bulletin*. 57 (2014) 260–267. doi:10.1016/j.materresbull.2014.06.013.
- [67] Y. Liu, S. Xie, C. Liu, J. Li, X. Lu, Y. Tong, Facile synthesis of tungsten oxide nanostructures for efficient photoelectrochemical water oxidation, *Journal of Power Sources*. 269 (2014) 98–103. doi:10.1016/j.jpowsour.2014.07.012.
- [68] G. Zhang, C. Xie, A novel method in the gas identification by using WO_3 gas sensor based on the temperature-programmed technique, *Sensors and Actuators B: Chemical*. 206 (2015) 220–229. doi:10.1016/j.snb.2014.09.063.

- [69] G. Zhang, C. Xie, S. Zhang, J. Zhao, T. Lei, D. Zeng, Temperature-programmed technique accompanied with high-throughput methodology for rapidly searching the optimal operating temperature of MOX gas sensors., *ACS Combinatorial Science*. 16 (2014) 459–65. doi:10.1021/co500054r.
- [70] X. Bai, H. Ji, P. Gao, Y. Zhang, X. Sun, Morphology, phase structure and acetone sensitive properties of copper-doped tungsten oxide sensors, *Sensors and Actuators B: Chemical*. 193 (2014) 100–106. doi:10.1016/j.snb.2013.11.059.
- [71] A. Kumar, S. Keshri, D. Kabiraj, Influence of annealing temperature on nanostructured thin films of tungsten trioxide, *Materials Science in Semiconductor Processing*. 17 (2014) 43–52. doi:10.1016/j.mssp.2013.07.018.
- [72] N.M.G. Parreira, N.J.M. Carvalho, A. Cavaleiro, Synthesis, structural and mechanical characterization of sputtered tungsten oxide coatings, *Thin Solid Films*. 510 (2006) 191–196. doi:10.1016/j.tsf.2005.12.299.
- [73] N.M.G. Parreira, T. Polcar, A. Cavaleiro, Thermal stability of reactive sputtered tungsten oxide coatings, *Surface and Coatings Technology*. 201 (2007) 7076–7082. doi:10.1016/j.surfcoat.2007.01.019.
- [74] T. Polcar, T. Kubart, E. Malainho, M. Vasilevskiy, N.M.G. Parreira, A. Cavaleiro, Nanoscale colour control: W-O graded coatings deposited by magnetron sputtering, *Nanotechnology*. 19 (2008) 395202. doi:10.1088/0957-4484/19/39/395202.
- [75] C. Charles, N. Martin, M. Devel, J. Ollitrault, A. Billard, Correlation between structural and optical properties of WO₃ thin films sputter deposited by glancing angle deposition, *Thin Solid Films*. 534 (2013) 275–281. doi:10.1016/j.tsf.2013.03.004.
- [76] C. Charles, N. Martin, M. Devel, Optical properties of nanostructured WO₃ thin films by GLancing Angle Deposition: Comparison between experiment and simulation, *Surface and Coatings Technology*. 276 (2015) 136–140. doi:10.1016/j.surfcoat.2015.06.051.
- [77] A. Farjadpour, D. Roundy, A. Rodriguez, M. Ibanescu, P. Bermel, J.D. Joannopoulos, S.G. Johnson, G.W. Burr, Improving accuracy by subpixel smoothing in the finite-difference time domain, *Optics Letters*. 31 (2006) 2972. doi:10.1364/OL.31.002972.
- [78] D. Deniz, D.J. Frankel, R.J. Lad, Nanostructured tungsten and tungsten trioxide films prepared by glancing angle deposition, *Thin Solid Films*. 518 (2010) 4095–4099. doi:10.1016/j.tsf.2009.10.153.
- [79] M. Horprathum, K. Limwichean, A. Wisitsoraat, P. Eiamchai, K. Aiempanakit, P. Limnonthakul, N. Nuntawong, V. Pattantsetakul, A. Tuantranont, P. Chindaudom, NO₂-sensing properties of WO₃ nanorods prepared by glancing angle DC magnetron sputtering, *Sensors and Actuators B: Chemical*. 176 (2013) 685–691. doi:10.1016/j.snb.2012.09.077.
- [80] H.G. Moon, Y.-S. Shim, D.H. Kim, H.Y. Jeong, M. Jeong, J.Y. Jung, S.M. Han, J.K. Kim, J.-S. Kim, H.-H. Park, J.-H. Lee, H.L. Tuller, S.-J. Yoon, H.W. Jang, Self-activated ultrahigh chemosensitivity of oxide thin film nanostructures for transparent sensors., *Scientific Reports*. 2 (2012) 588. doi:10.1038/srep00588.
- [81] A. Wisitsoorat, M.Z. Ahmad, M.H. Yaacob, M. Horpratum, D. Phakaratkul, T. Lomas, A. Tuantranont, W. Wlodarski, Optical H₂ sensing properties of vertically aligned Pd/WO₃ nanorods thin films deposited via glancing angle rf magnetron sputtering, *Sensors and Actuators B: Chemical*. 182 (2013) 795–801. doi:10.1016/j.snb.2013.03.091.
- [82] M.Z. Ahmad, A. Wisitsoraat, A.S. Zoolfakar, R.A. Kadir, W. Wlodarski, Investigation of RF sputtered tungsten trioxide nanorod thin film gas sensors prepared with a glancing angle deposition method toward reductive and oxidative analytes, *Sensors and Actuators B: Chemical*. 183 (2013) 364–371. doi:10.1016/j.snb.2013.04.027.
- [83] C. Wongchoosuk, A. Wisitsoraat, D. Phokharatkul, M. Horprathum, A. Tuantranont, T. Kerdcharoen, Carbon doped tungsten oxide nanorods NO₂ sensor prepared by glancing angle RF sputtering, *Sensors and Actuators B: Chemical*. 181 (2013) 388–394. doi:10.1016/j.snb.2013.01.066.

- [84] L.J. van der Pauw, A method of measuring specific resistivity and Hall effect of discs of arbitrary shape, *Philips Research Reports*. 13 (1958) 1–9.
- [85] Hall Effect Measurements, (2010). <https://www.nist.gov/pml/engineering-physics-division/popular-links/hall-effect>.
- [86] A. Gaddari, F. Berger, M. Amjoud, J.B. Sanchez, M. Lahcini, B. Rhouta, D. Mezzane, C. Mavon, E. Beche, V. Flaude, A novel way for the synthesis of tin dioxide sol-gel derived thin films: Application to O₃ detection at ambient temperature, *Sensors and Actuators, B: Chemical*. 176 (2013) 811–817. doi:10.1016/j.snb.2012.10.049.
- [87] J.A. Thornton, Influence of apparatus geometry and deposition conditions on the structure and topography of thick sputtered coatings, *Journal of Vacuum Science and Technology*. 11 (1974) 666–670. doi:10.1116/1.1312732.
- [88] A. Anders, A structure zone diagram including plasma-based deposition and ion etching, *Thin Solid Films*. 518 (2010) 4087–4090. doi:10.1016/j.tsf.2009.10.145.
- [89] T.P. Drüsedau, T. Bock, T.-M. John, F. Klabunde, W. Eckstein, Energy transfer into the growing film during sputter deposition: An investigation by calorimetric measurements and Monte Carlo simulations, *Journal of Vacuum Science & Technology A: Vacuum, Surfaces, and Films*. 17 (1999) 2896–2905. doi:10.1116/1.581957.
- [90] S. Schiller, U. Heisig, C. Korndörfer, G. Beister, J. Reschke, K. Steinfeld, J. Strümpfel, Reactive d.c. high-rate sputtering as production technology, *Surface and Coatings Technology*. 33 (1987) 405–423. doi:10.1016/0257-8972(87)90206-4.
- [91] A. Billard, C. Frantz, Attempted modelling of thickness and chemical heterogeneity in coatings prepared by d.c. reactive magnetron sputtering, *Surface and Coatings Technology*. 59 (1993) 41–47. doi:10.1016/0257-8972(93)90052-P.
- [92] N. Martin, R. Sanjinès, J. Takadom, F. Lévy, Enhanced sputtering of titanium oxide, nitride and oxynitride thin films by the reactive gas pulsing technique, *Surface and Coatings Technology*. 142–144 (2001) 615–620. doi:10.1016/S0257-8972(01)01149-5.
- [93] T. Kubart, T. Polcar, O. Kappertz, N. Parreira, T. Nyberg, S. Berg, A. Cavaleiro, Modelling of magnetron sputtering of tungsten oxide with reactive gas pulsing, *Plasma Processes and Polymers*. 4 (2007) S522–S526. doi:10.1002/ppap.200731301.
- [94] S. Berg, T. Nyberg, Fundamental understanding and modeling of reactive sputtering processes, *Thin Solid Films*. 476 (2005) 215–230. doi:10.1016/j.tsf.2004.10.051.
- [95] M. Stolze, B. Camin, F. Galbert, U. Reinholz, L.K. Thomas, Nature of substoichiometry in reactively DC-sputtered tungsten oxide thin films and its effect on the maximum obtainable colouration by gases, *Thin Solid Films*. 409 (2002) 254–264. doi:10.1016/S0040-6090(02)00058-5.
- [96] D.R. Lide, *CRC Handbook of Chemistry and Physics*. Section 14, Geophysics, Astronomy, and Acoustics; Abundance of Elements in the Earth's Crust and in the Sea, (2005).
- [97] G. Reiss, J. Vancea, H. Hoffmann, Grain-boundary resistance in polycrystalline metals, *Physical Review Letters*. 56 (1986) 2100–2103. doi:10.1103/PhysRevLett.56.2100.
- [98] A. Cacucci, I. Tsiaoussis, V. Potin, L. Imhoff, N. Martin, T. Nyberg, The interdependence of structural and electrical properties in TiO₂/TiO/Ti periodic multilayers, *Acta Materialia*. 61 (2013) 4215–4225. doi:10.1016/j.actamat.2013.03.047.
- [99] I. Goldfarb, F. Miao, J.J. Yang, W. Yi, J.P. Strachan, M.X. Zhang, M.D. Pickett, G. Medeiros-Ribeiro, R.S. Williams, Electronic structure and transport measurements of amorphous transition-metal oxides: Observation of Fermi glass behavior, *Applied Physics A: Materials Science and Processing*. 107 (2012) 1–11. doi:10.1007/s00339-012-6856-z.
- [100] J.M. Berak, M.J. Sienko, Effect of oxygen-deficiency on electrical transport properties of tungsten trioxide crystals, *Journal of Solid State Chemistry*. 2 (1970) 109–133. doi:10.1016/0022-4596(70)90040-X.
- [101] J. Molenda, A. Kubik, Electrical properties of nonstoichiometric WO_{3-y} at temperatures 77 to 300 K, *Physica Status Solidi (B)*. 191 (1995) 471–478. doi:10.1002/pssb.2221910220.

- [102] E. Machlin, *Materials Science in microelectronics I: The relationships between thin film processing and structure*, Elsevier, 2010.
- [103] V. Patil, P. Joshi, M. Chougule, S. Sen, Synthesis and characterization of Co₃O₄ thin film, *Soft Nanoscience Letters*. 2 (2012) 1–7. doi:10.4236/snl.2012.21001.
- [104] Y.U. Peter, M. Cardona, *Fundamentals of semiconductors: physics and materials properties*, Springer Science & Business Media, 2010.
- [105] S. Sadeghi-Khosravieh, K. Robbie, Morphology and crystal texture in tilted columnar micro-structured titanium thin film coatings, *Thin Solid Films*. 627 (2017) 69–76. doi:10.1016/j.tsf.2017.02.038.
- [106] Y. Li, N. Koshizaki, W. Cai, Periodic one-dimensional nanostructured arrays based on colloidal templates, applications, and devices, *Coordination Chemistry Reviews*. 255 (2011) 357–373. doi:10.1016/j.ccr.2010.09.015.
- [107] X. Xu, M. Arab Pour Yazdi, J.-Y. Rauch, R. Salut, A. Billard, V. Potin, N. Martin, Tungsten Oxide Thin Films Sputter Deposited by the Reactive Gas Pulsing Process for the Dodecane Detection, *Materials Today: Proceedings*. 2 (2015) 4656–4663. doi:10.1016/j.matpr.2015.09.019.
- [108] S. Kasap, P. Capper, *Handbook of Electronic and Photonic Materials*, Springer, 2006.
- [109] R. Swanepoel, Determination of the thickness and optical constants of amorphous silicon, *Journal of Physics E: Scientific Instruments*. 16 (1983) 1214–1222. doi:10.1088/0022-3735/16/12/023.
- [110] A. Besnard, N. Martin, L. Carpentier, B. Gallas, A theoretical model for the electrical properties of chromium thin films sputter deposited at oblique incidence, *Journal of Physics D: Applied Physics*. 44 (2011) 215301. doi:10.1088/0022-3727/44/21/215301.
- [111] K. Viswanathan, K. Brandt, E. Salje, Crystal structure and charge carrier concentration of W₁₈O₄₉, *Journal of Solid State Chemistry*. 36 (1981) 45–51. doi:10.1016/0022-4596(81)90190-0.
- [112] D.B. Migas, V.L. Shaposhnikov, V.E. Borisenko, Tungsten oxides. II. The metallic nature of Magnéli phases, *Journal of Applied Physics*. 108 (2010) 93714. doi:10.1063/1.3505689.
- [113] B. Frühberger, M. Grunze, D.J. Dwyer, Surface chemistry of H₂S-sensitive tungsten oxide films, *Sensors and Actuators B: Chemical*. 31 (1996) 167–174. doi:10.1016/0925-4005(96)80062-1.
- [114] C.S. Rout, A. Govindaraj, C.N.R. Rao, High-sensitivity hydrocarbon sensors based on tungsten oxide nanowires, *Journal of Materials Chemistry*. 16 (2006) 3936–3941.
- [115] J.F. McAleer, P.T. Moseley, J.O.W. Norris, D.E. Williams, P. Taylor, B.C. Tofield, Tin oxide based gas sensors, *Materials Chemistry and Physics*. 17 (1987) 577–583.
- [116] D. Kohl, Surface processes in the detection of reducing gases with SnO₂-based devices, *Sensors and Actuators*. 18 (1989) 71–113.
- [117] X. Xu, M.A.P. Yazdi, R. Salut, J.-M. Cote, A. Billard, N. Martin, Structure, composition and electronic transport properties of tungsten oxide thin film sputter-deposited by the reactive gas pulsing process, *Materials Chemistry and Physics*. 205 (2018) 391–400. doi:10.1016/j.matchemphys.2017.11.048.
- [118] K.M. Krause, M.T. Taschuk, K.D. Harris, D.A. Rider, N.G. Wakefield, J.C. Sit, J.M. Buriak, M. Thommes, M.J. Brett, Surface area characterization of obliquely deposited metal oxide nanostructured thin films, *Langmuir*. 26 (2009) 4368–4376.
- [119] C. Charles, N. Martin, M. Devel, Optical properties of WO₃ thin films modeled by finite-difference time-domain and fabricated by glancing angle deposition, *Journal of Nanoscience and Nanotechnology*. 12 (2012) 9125–9130.
- [120] M.C. Carotta, V. Guidi, G. Martinelli, M. Nagliati, D. Puzzovio, D. Vecchi, Sensing of volatile alkanes by metal-oxide semiconductors, *Sensors and Actuators B: Chemical*. 130 (2008) 497–501.
- [121] J. Guérin, K. Aguir, M. Bendahan, C. Lambert-Mauriat, Thermal modelling of a WO₃ ozone

- sensor response, *Sensors and Actuators B: Chemical*. 104 (2005) 289–293.
- [122] S. Ferrer, G.S. Somorjai, Ultraviolet photoelectron spectroscopy study of the adsorption of oxygen on reduced SrTiO₃ surfaces, *Journal of Applied Physics*. 52 (1981) 4792–4794. doi:10.1063/1.329319.
- [123] A. Labidi, C. Jacolin, M. Bendahan, A. Abdelghani, J. Guerin, K. Aguir, M. Maaref, Impedance spectroscopy on WO₃ gas sensor, *Sensors and Actuators B: Chemical*. 106 (2005) 713–718. doi:10.1016/j.snb.2004.09.022.
- [124] K. Kanda, T. Maekawa, Development of a WO₃ thick-film-based sensor for the detection of VOC, *Sensors and Actuators, B: Chemical*. 108 (2005) 97–101. doi:10.1016/j.snb.2005.01.038.
- [125] V.V. Malyshev, A.A. Vasiliev, A.V. Eryshkin, E.A. Koltypin, Y.I. Shubin, A.I. Buturlin, V.A. Zaikin, G.B. Chakhunashvili, Gas sensitivity of SnO₂ and ZnO thin-film resistive sensors to hydrocarbons, carbon monoxide and hydrogen, *Sensors and Actuators B: Chemical*. 10 (1992) 11–14. doi:10.1016/0925-4005(92)80004-H.
- [126] S. Cui, H. Pu, S.A. Wells, Z. Wen, S. Mao, J. Chang, M.C. Hersam, J. Chen, Ultrahigh sensitivity and layer-dependent sensing performance of phosphorene-based gas sensors, *Nature Communications*. 6 (2015) 1–9. doi:10.1038/ncomms9632.
- [127] M. Horprathum, T. Srichaiyaperk, B. Samransuksamer, A. Wisitsoraat, P. Eiamchai, S. Limwichean, C. Chananonawathorn, K. Aiempnanakit, N. Nuntawong, V. Patthanasettakul, C. Oros, S. Porntheeraphat, P. Songsiriritthigul, H. Nakajima, A. Tuantranont, P. Chindaudom, Ultrasensitive hydrogen sensor based on Pt-decorated WO₃ nanorods prepared by glancing-angle dc magnetron sputtering, *ACS Applied Materials & Interfaces*. 6 (2014) 22051–22060. doi:10.1021/am505127g.

9. Appendices

9.1. Curriculum Vitae

Introduction:

Name: XU Xiaolong **Birthday:** 07/21/1988 **Major:** Materials science
Mobile Call: +33 6 68 07 71 08 **E-mail:** roy.xiaolong.xu@outlook.com
Address: 18, rue de la Cassotte, 25000 BESANCON, France
Ph.D. supervisor: Nicolas MARTIN, Alain BILLARD, Mohammad ARAB POUR YAZDI

Education Experience:

2014.09~present Université Bourgogne Franche-Comté (UBFC), Institute FEMTO-ST Department of Micro Nano Sciences & Systems Ph.D. student
2011.09~2014.07 Beijing Jiaotong University Department of Chemical Engineering Master
2006.09~2010.07 Tianjin University Department of Material Science and Engineering Bachelor
2008.09~2010.07 Tianjin University Department of Business Administration Bachelor

Research Experience:

2014.09-present Project of “**Nanostructured metal oxide thin films for gas sensors**”
2013.01-2014.12 Research Assistant: Project of “**Research of preparation of composite nano material and its optical response for purification of sewage**”
2012.09-2014.09 Research Assistant: Project of “**Preparation of carbon inverse opal photonic crystal**”
2009.08-2010.07 Project of “**Low-temperature sintering of ZnO varistor ceramics and its performance optimization**”
2008.09-2009.11 With the team work, finished the project “**Preparation and properties of respiratory disease - electronic nose with nanometer sensitive material**”

Capabilities and Skills:

Computer Abilities:

Skilled in use of Microsoft Office, Visual Basic (certification), Origin, Jade, Photoshop, Mendeley, Digital Micrograph.

Basic use of AutoCAD, CorelDraw, Solid work, ANSYS (Finite Element Analysis).

Operate instruments:

Independent operation of sputtering process, UV-visible spectrophotometer, infrared spectrometer, SEM, XRD, gas sensor detect system, 4-point resistivity.

Analysis experience of EDS, DSC, TGA, XPS.

Language Skills: IELTS 6.0 (English), TCF B1 (French)

Publications and Communication:

9 Publications referenced by SCI and EI
3 Communications (international and national)
2 Patents in China

9.2. List of publications and communications

List of publications

- [1]. **Xiaolong Xu**, Mohammad Arab Pour Yazdi, Jean-Baptiste Sanchez, Alain Billard, Franck Berger, Nicolas Martin. Exploiting the dodecane and ozone sensing capabilities of nanostructured W-O films. *Sensors & Actuators B. Chemical*. in press, 2018.
- [2]. **Xiaolong Xu**, Mohammad Arab Pour Yazdi, Jean-Baptiste Sanchez, Alain Billard, Franck Berger, Nicolas Martin. Reactive co-sputtering of W-O thin films by GLancing Angle Deposition for gas sensors. *Materials Today: Proceedings*. in press, 2018
- [3]. **Xiaolong Xu**, Mohammad Arab Pour Yazdi, Roland Salut, Jean-Marc Cote, Alain Billard, Nicolas Martin. Structure, composition and electronic transport properties of W-O thin film sputter-deposited by the Reactive Gas Pulsing Process. *Materials Chemistry and Physics*. 2018, 205: 391-400.
- [4]. **Xiaolong Xu**, Mohammad Arab Pour Yazdi, Jean-Yves Rauch, Roland Salut, Alain Billard, Valérie Potin, Nicolas Martin. W-O Thin Films Sputter Deposited by the Reactive Gas Pulsing Process for the Dodecane Detection. *Materials Today: Proceedings*. 2015, 2(9): 4656-4663/4656-4663.
- [5]. Hui Zhang, **Xiaolong Xu**. Transition Metal Oxides Inverse Opals and Their Applications in Photo(electro)chemical Processes. *Progress in Chemistry*. 2013, 25(11): 1858-1866. SCIE
- [6]. **Xiaolong Xu**, Hui Zhang, Shengnan Liu, et al. Preparation of Three-Dimensional Ordered Macroporous Zirconia and Characteristics of Its Pore Walls. *Journal of the Chinese Ceramic Society*, 2013, 41(5): 705-709.
- [7]. **Xiaolong Xu**, Hui Zhang, Shengnan Liu, et al. Study on Surface Characteristics of TiO₂ Three-Dimensional Ordered Macroporous Materials. *Journal of Synthetic Crystals*, 2013, 42(3): 461-465.
- [8]. Hui Zhang, **Xiaolong Xu**, Fan Li, et al. Influencing Factors of Macroporous Ordering in TiO₂ and ZrO₂ Inverse Opals. *Key Engineering Materials*, 2013, 554, 209-212.
- [9]. Hui Zhang, Chen, **Xiaolong Xu**, et al. Syntheses of Mesoporous ZnO and SnO₂ Microspheres by Spray Reaction Process. *Key Engineering Materials*, 2012, 519, 74-78. EI

List of communications

- [1]. **Xiaolong Xu**, Mohammad Arab Pour Yazdi, Jean-Baptiste Sanchez, Alain Billard, Franck Berger, Nicolas Martin. Reactive co-sputtering of W-O thin films by GLancing Angle Deposition for gas sensors. Besançon, France: 3rd International Workshop on Functionalized Surfaces for Sensor Applications, May 30-31, 2017.
- [2]. **Xiaolong Xu**, Mohammad Arab Pour Yazdi, Jean-Yves Rauch, Roland Salut, Alain Billard, Valérie Potin, Nicolas Martin. WO_x Film Sputter Deposition by GLAD and Gas Pulsing. Nancy France: 7th international conference on innovations in thin film processing and characterization, November 16-20, 2015, Michel Cantarel student grant.
- [3]. **Xiaolong Xu**, Hui Zhang, Shengnan Liu, et al. One Step Preparation of Al₂O₃ and ZrO₂ Three-Dimensional Ordered Macroporous Materials. Nanjing China: 17th National Academic Conference of High-tech Ceramics, September 19-21, 2012, Oral.

List of patents

- [1]. Hui Zhang, **Xiaolong Xu**, Ming Fu. Preparation of Controllable Line Defect Colloidal Photonic Crystal. CN, A, 201010037987.5. 2012.07.25. CN Patent
- [2]. Hui Zhang, **Xiaolong Xu**. Method of Particulate Fluidization Assembly of Multiple Colloidal Photonic Crystal. CN, A, 201110428500.1. 2012.07.11. CN Patent

Summary

This thesis is focused on the reactive sputter deposition of W-O thin films. In order to play with their composition, the Reactive Gas Pulsing Process (RGPP) is implemented and allows tunable oxygen and tungsten concentrations. Similarly, the GLancing Angle Deposition (GLAD) technique is developed to produce various architectures, namely inclined columns, zigzags and spirals, and increases the surface-to-volume ratio of the films. The GLAD co-sputtering approach is also investigated by means of two inclined and separated W and WO₃ targets. Relationships between microstructure, composition, electronic and optical properties of W-O films are systematically studied. They are finally applied as active layers for resistive sensors in order to improve detection of dodecane vapor and ozone gas. The high porous microstructure of inclined columns produced by GLAD combined to the suitable composition adjusted by RGPP leads to define a range of W-O films attractive for sensing performances.

Keywords

W-Os, thin films, RGPP, GLAD, co-sputtering, gas sensor, dodecane, ozone.

Résumé

Cette thèse est dédiée à l'élaboration de couches minces d'oxydes de tungstène par pulvérisation cathodique réactive. Afin de jouer sur la composition des films, le procédé de pulsation du gaz réactif (RGPP) est mis en œuvre pour changer les concentrations en oxygène et en tungstène. En parallèle, la technique de dépôt sous incidence oblique (GLAD) est développée pour produire différentes architectures, à savoir des colonnes inclinées, des zigzags ou encore des spirales, et augmenter le rapport surface-volume dans les films. La co-pulvérisation GLAD est également étudiée en utilisant deux cibles inclinées et séparées de W et WO₃. Les relations entre la microstructure, la composition, les propriétés électroniques et optiques des films d'oxydes de tungstène sont systématiquement étudiées. Ils sont finalement appliqués comme couches actives pour des capteurs résistifs afin d'améliorer la détection de vapeur de dodécane et d'ozone gazeux. La microstructure poreuse élevée des colonnes inclinées produite par GLAD combinée à une composition ajustée par RGPP conduit à définir une gamme de films d'oxydes de tungstène attractifs pour améliorer les performances capteurs.

Mots-clés

Oxydes de tungstène, films minces, RGPP, GLAD, co-pulvérisation, capteurs de gaz, dodécane, ozone.



SPIM

■ École doctorale SPIM - Université de Technologie Belfort-Montbéliard
F - 90010 Belfort Cedex ■ tél. +33 (0)3 84 58 31 39
■ ed-spim@univ-fcomte.fr ■ www.ed-spim.univ-fcomte.fr

